POLITECNICO
MILANO 1863

SCUOLA DI INGEGNERIA INDUSTRIALE
E DELL'INFORMAZIONE

# Assessment of Stiff Trench and Metawedge as Mitigation Measures for Railway Induced Ground Vibration

Tesi di Laurea Magistrale in
Mechanical Engineering - Ingegneria Meccanica

Author: **Alessandro Bracci**
**Student ID:** 939910

**TU Delft Advisor:** Prof. Karel N. van Dalen
**Co-Advisors:**
Prof. Andrei V. Metrikine (TU Delft)
Ir. Andrei B. Fărăgău (TU Delft)
Dr. João M. de Oliveira Barbosa (TU Delft)
Ir. Eliam Vlijm (Cohere Consultants)

**PoliMi Advisor:** Prof. Roberto Corradi

**Academic Year:** 2020-21

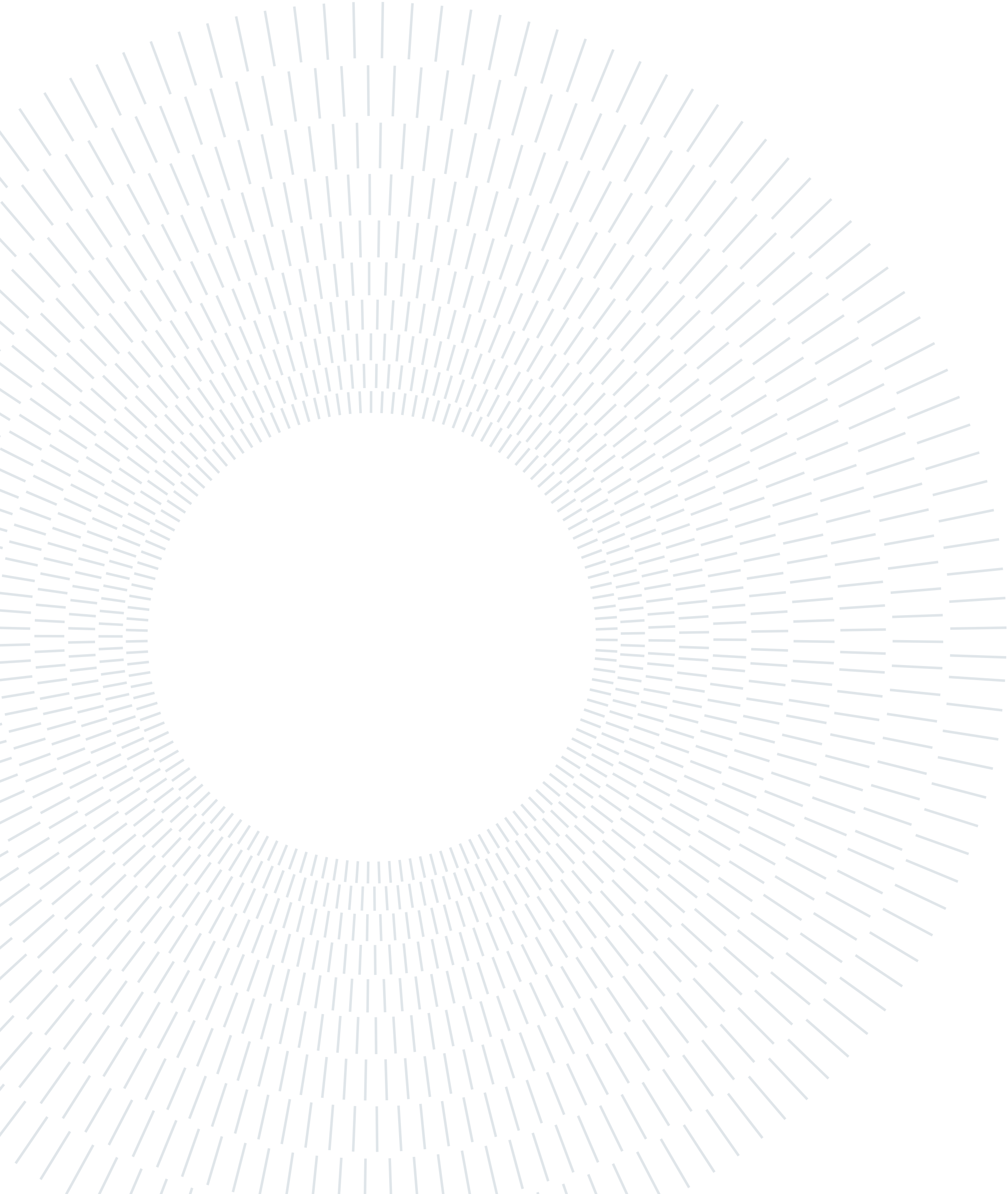

*"If I have seen further it is by standing on the shoulders of Giants."*

Isaac Newton

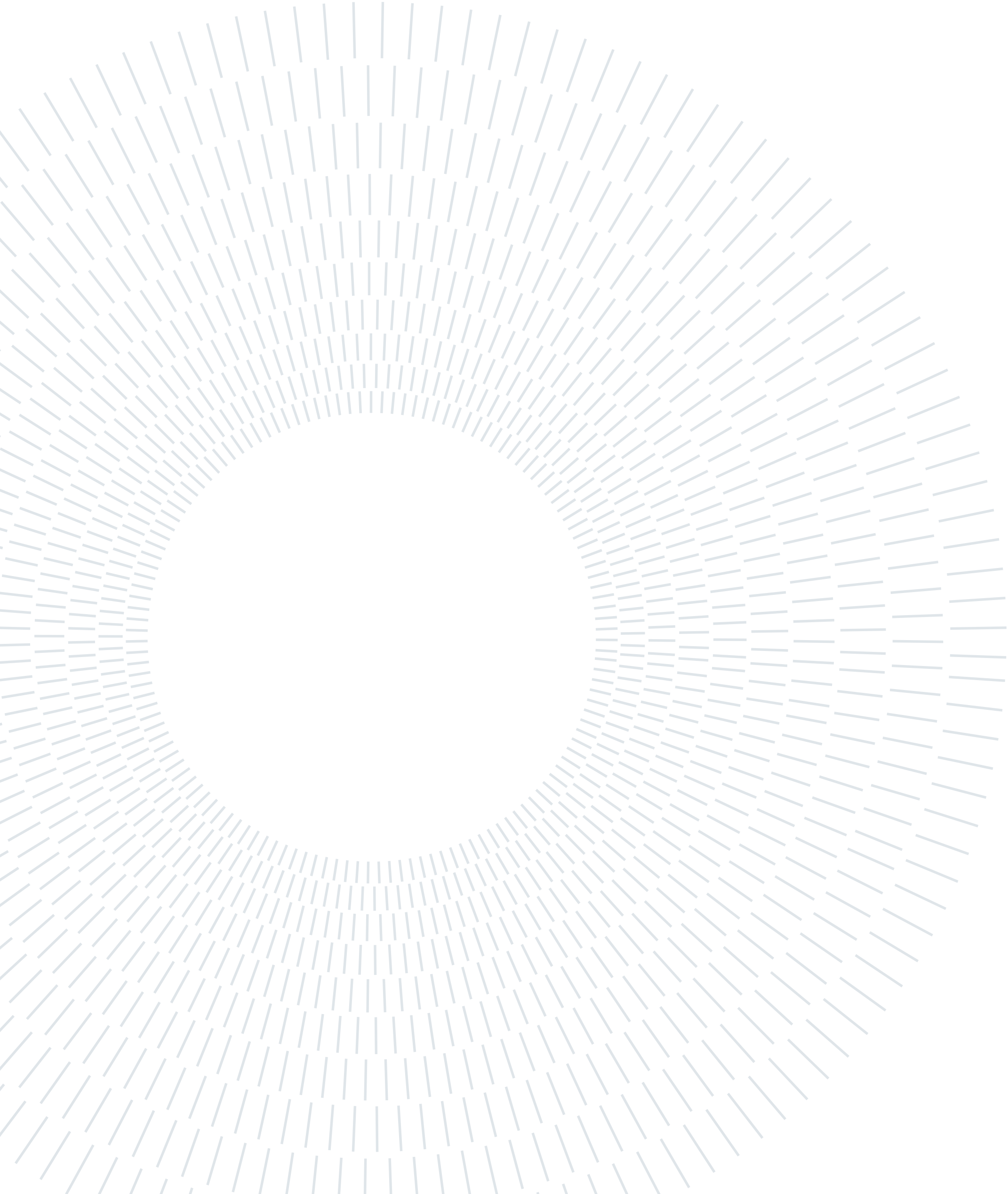

# Abstract

Railway induced vibration may lead to annoyance to lineside residents. Mitigation measures can be installed on the transmission path to reduce the ground motion generated by the train passage.

This work studies the efficiency of a stiff in-filled trench for the attenuation of railway induced ground vibration. The key mitigation mechanisms of this solution are investigated to understand its physical behaviour and to improve its vibration attenuation performance with practically applicable design guidelines. The trench effect is firstly determined by in-situ measurements, which highlight a beneficial vibration reduction. The performance is further examined by means of a 2.5D approach. The numerical tool reveals that the stiffness difference between the trench material and the surrounding soil is the most important aspect to enhance the positive wave impeding effect. Indeed, an increase of the Young's modulus difference between the two media leads to a better vibration mitigation. This shows how the wave propagation is hindered through the activation of the trench free bending modes. The simulations with the 2.5D model include both homogeneous and layered half-space models for the soil. The wave attenuation related to the stiffness difference between the stiff trench and the ground is verified with both cases. Comparing the performance assessment carried out through the field measurements and numerical data, a better match is experienced for the vertical vibration component, while contradictory trends are visible for the horizontal direction.

The proposal of an innovative mitigation system for railway induced vibration is presented as the second objective. Both 2D and 2.5D models are adopted in this study. The metawedge countermeasure is suggested to divert the incoming waves deep into the soil by exploiting its non-conventional dispersion properties. The proposed solution is able to convert the surface waves into body ones, redirecting the approaching energy content far from the surface. This mechanism is attained for the frequency range mainly excited by the train passage, resulting in a successful vibration reduction at the surface level.

**Keywords:** In-filled Trench, Metawedge, Railroads, Ground Vibration, Soil Dynamics, 2.5D Approach

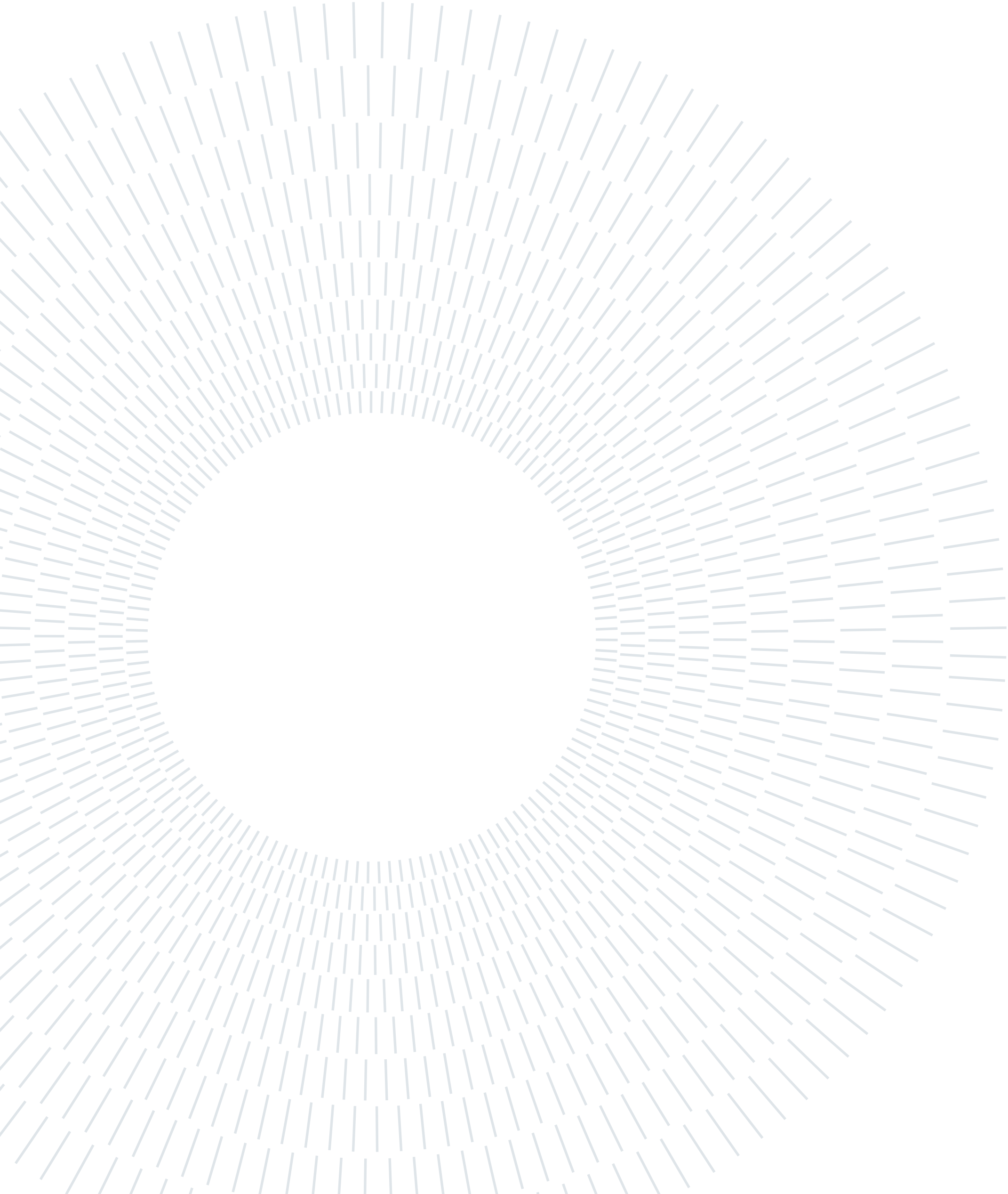

# Sommario

La vibrazione derivante dal traffico ferroviario può comportare un fastidio per i residenti delle zone limitrofe. Per ridurre la vibrazione del suolo generata dal passaggio del treno è possibile installare delle misure di mitigazione lungo il percorso di propagazione.

L'obiettivo dell'elaborato consiste nello studiare l'efficienza di una trincea rigida piena per la riduzione della vibrazione indotta dalla ferrovia. Al fine di comprenderne appieno il comportamento fisico e per migliorarne le prestazioni proponendo delle linee guida di design è di fondamentale importanza esaminare i principali meccanismi di mitigazione. In primo luogo, l'effetto della trincea viene analizzato mediante delle misurazioni sperimentali che mostrano una positiva riduzione delle vibrazioni. La prestazione viene ulteriormente esaminata con un modello 2.5D. Questo rivela come la differenza di rigidità tra il materiale della trincea e il terreno circostante rappresenti l'aspetto più importante per migliorare l'efficacia del sistema. Aumentando la differenza del modulo di Young tra i due materiali si ottiene una migliore attenuazione. Ciò mostra come la propagazione dell'onda sia ostacolata della rigidezza flessionale della trincea. Le simulazioni con il modello 2.5D includono per il suolo sia un semispazio omogeneo che a strati. L'attenuazione dell'onda basata sulla differenza di rigidezza tra la trincea rigida e il terreno viene verificata in entrambi i casi. Confrontando i dati sperimentali e numerici per valutare la prestazione della trincea, un migliore risultato viene ottenuto per la componente verticale della vibrazione, mentre tendenze contradditorie appaiono per la direzione orizzontale.

Il secondo obiettivo consiste nella proposta di un innovativo sistema di mitigazione per l'applicazione ferroviaria. In questa parte, entrambi i modelli 2D e 2.5D vengono utilizzati. Il sistema chiamato metawedge viene suggerito per deviare le onde in arrivo nel terreno grazie alle sue proprietà di dispersione non convenzionali. La soluzione proposta è in grado di convertire le onde superficiali in onde di volume, reindirizzando il contenuto energetico lontano dalla superficie. Questo meccanismo si ottiene per le frequenze maggiormente eccitate dal veicolo, dando così vita a una buona riduzione delle vibrazioni sulla superficie.

**Parole chiave:** Trincea Piena, Metawedge, Ferrovia, Vibrazione del Terreno, Dinamica del Suolo, Approccio 2.5D

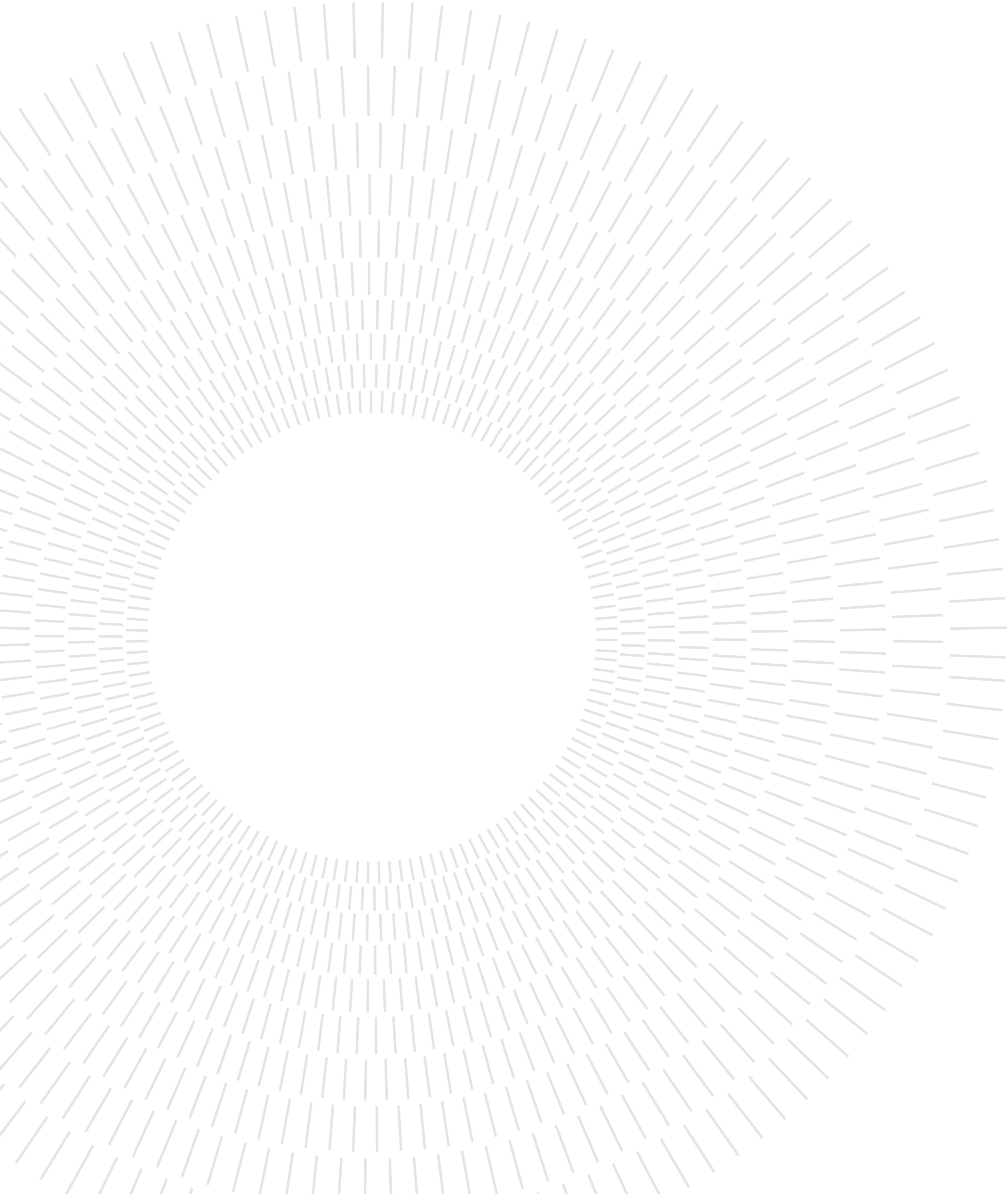

# Contents

# Introduction

## Background

Railway transport is environmentally friendly and offers many advantages for sustainable development [1]. However, the ground vibration induced by the train passage is a widely reported issue among the nearby residents [2]. Indeed, the vibration transmitted through the ground can represent a source of disturbance and annoyance. The vibration is generated by the running vehicle at the interface between the wheel and the rail. Heavy axle-load freight traffic, travelling at relatively low speed, causes high amplitude motion at the track [3]. This type of source excites waves in the soil that propagate along the ground surface (Rayleigh waves). The perturbation experienced at the receiver position depends not only on the coupling effect between the vehicle and the track but also on the soil properties. This vibration phenomenon is especially associated with soft soil conditions, where significant levels of vibration may be propagated up to distances of the order of 100 m from the railway line [3]. In the Netherlands, this aspect can be particularly problematic due to the typical ground structure, which is generally stratified with soft upper layers [4]. In these cases, a considerable energy content can be detected at a very low frequency (below 10 Hz). These low frequency waves can be perceived by the human body, leading to increased heart rates and reduced sleep quality [5, 6].

To limit these side effects of the railway traffic, mitigation measures can be adopted at the source, on the transmission path or at the receiver. When the vibration attenuation is required for already existing tracks and buildings, applying a countermeasure on the transmission path represents the most attractive option. Concerning this solution, different possibilities are available: open or soft trenches [7], stiff trenches [8], subgrade stiffening [9, 10], wave impeding block [11], sheet pile walls [12, 13] and heavy mass next to the track [14, 15]. Fig. 1 offers a schematic representation of the listed technologies. They aim at hindering the wave propagation through the soil. The expected effectiveness must be carefully considered when choosing the most appropriate mitigation measure for the specific case. Apart from the vibration attenuation, the economical and environmental factors must also be examined [16]. Numerical prediction tools can assess the performance of the system and have become crucial to determining the most appropriate design [17].

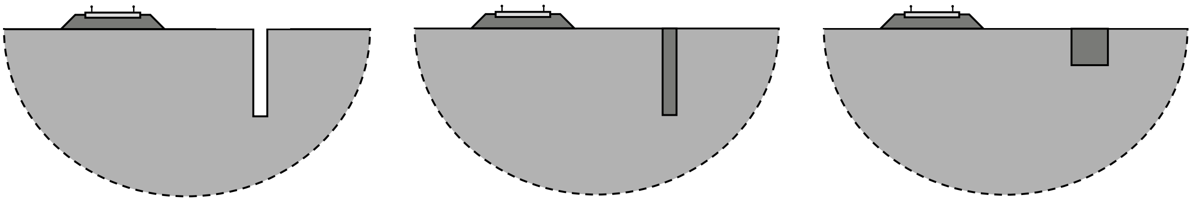

(a) Open trench. (b) In-filled trench. (c) Subgrade stiffening.

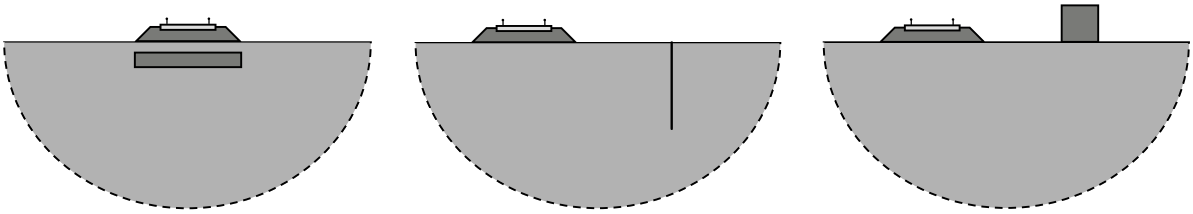

(d) Wave impeding block. (e) Sheet pile wall. (f) Heavy mass.

Figure 1: Mitigation measures on the transmission path.

## Aim of the work

The growing interest in mitigation measures gives rise to numerous engineering challenges that have been studied over the years [18]. Several works have been published to examine the effects of different countermeasures, which are applied on the transmission path to reduce railway induced vibration. The present thesis intends to contribute to this research field by investigating the effect of a stiff in-filled trench and proposing an innovative mitigation solution which is the metawedge.

The so-called stiff trench is an already existing mitigation measure, which is analysed in detail in the current work to build a deep knowledge of its physical behaviour. A better understanding of its mitigation mechanisms provides the opportunity to achieve improved performance by means of more effective and practically oriented design guidelines, which are usable in the engineering sector. The interest in enhancing the performance of the stiff in-filled trench with respect to the existing designs has motivated the development of this work.

The metawedge technology - inspired by seismic engineering applications - is introduced to suggest and incite future projects related to an innovative vibration attenuation method. Making use of its new mitigation strategy that is based on the divergence of the surface waves into the deep soil, this system is considered a possible alternative to the usual vibration countermeasures. Indeed, its conception originates from the need of overcoming the weak points of the other mitigation measures.

The goal of this thesis lies in the research of the answers to the following research questions:

- **Which are the vibration mitigation mechanisms that dominate the stiff trench behaviour? How can its performance and effectiveness be improved?**

  By performing numerical simulations and analysing in-situ tests results, the effect and the fundamental attenuation principles of the stiff trench are assessed. The role of different model parameters is studied and discussed thoroughly to explore the possible enhancement of the vibration mitigation.

- **Can the metawedge be an effective mitigation measure for railway induced ground vibration? How does it work and could it become a competitive alternative to other commonly adopted mitigation measures?**

  The efficacy of a metawedge is numerically demonstrated for the excitation induced by railway traffic. The key mitigation mechanism is studied to propose a practical solution that shows favourable attenuation performance. The influence on the mitigation effect is studied for the most relevant model parameters.

In a few words, the current work aims at clarifying and resolving the theoretical and practical aspects concerning the stiff in-filled trench and metawedge mitigation measures for the railway application. Different models and approaches are embraced with this purpose.

## State of the art

In order to attenuate the railway traffic-induced ground vibration, the application of mitigation measures on the transmission path can represent the most appealing answer since it left unmodified the source and the receiver. Sometimes, modifying the source and receiver is unfeasible, so adopting a countermeasure on the transmission path is the only available solution for the ground vibration problem. This section provides a state of the art of the two countermeasures analysed in this work: the stiff in-filled trench and the metawedge.

Stiff in-filled trenches can be installed to hinder the propagation of railway induced waves from the source to the receiver, as qualitatively depicted in Fig. 1b. Contrary to the open trenches (see Fig. 1a), they do not suffer from stability problems and can be built deeper into the soil [19]. These side effects can be solved by filling the trench with a material that is softer than the surrounding soil, a numerical and experimental analysis is available for the soft in-filled trench in [20]. The reflection of the incoming wave guarantees a beneficial vibration reduction for both open and soft trenches because the transmitted wave carries less energy [7, 21–24]. Concerning the stiff in-filled trench, its material is stiffer than soil. This feature represents a key aspect of its mitigation mechanism and behaviour [8]. Design guidelines are formulated and proposed for the above-mentioned trenches in [25]. Regarding the dimension of the trench, for the case of open or soft trenches, only the depth is relevant, whereas also the width becomes important for stiff trenches. Examples of stiff trenches made of concrete are found [25, 26], while the description of a jet grouting one is available in [27]. The effect introduced by a stiffer material into the soil is studied for a squared subgrade stiffening (see Fig. 1c) with a 2.5D approach in [9, 10, 28]. The Timoshenko's beam is proposed to model the mitigation measure and the effect of its bending mode is investigated. Similar attenuation phenomena and outcomes are observed with 2D and 2.5D models in [17]. Some of these concepts are applied to a stiff trench in [8]. The stiffness contrast effect and the bending stiffness role are further analysed for a stiff sheet pile wall in [12, 13], a schematic representation of this countermeasure is displayed in Fig. 1e. In these works, the results of an in-situ test related to the records of train passages are also compared to the outcomes of a 2.5D model. The effectiveness of a stiff trench is similarly assessed through a 2.5D approach and an experimental campaign in [27], where the beneficial vibration attenuation appears particularly efficient in soft soil sites. Inspired by building acoustics, the potential of using a double stiff trench in reducing ground vibration transmission is investigated by means of a 2.5D procedure in [8, 29].

The application of a metawedge mitigation measure for civil engineering problems has been studied in literature over the past few years. Being a relatively new technology, only a limited number of studies have been published to investigate its performance in terms of vibration mitigation. Moreover, its application to ground vibration cases regards the seismic field. The ability of this system to convert the incoming surface waves into bulk ones is mainly exploited to protect the existing buildings or sensitive facilities from far-field damages caused by possible earthquakes. Several systems characterized by different levels of complexity have been proposed to achieve the vibration reduction at the surface exploiting the redirection of the incoming energy deep into the ground. This vibration mitigation mechanism is numerically and experimentally observed for an array of randomly distributed trees in [30]. The behaviour and performance of a metawedge composed of trees are analysed with a 2D model in [31]. This type of system is further investigated in [32]. The beneficial contribution of the bulky side branches connected with the main stem is demonstrated in [33]. They are able to enhance the frequency range of operation of the system, improving the resulting vibration attenuation. The procedure to design a metawedge made of two-dimensional rectangular boards is examined in detail in [34]. The influence of different design parameters on the attenuation effect is also considered. In [35, 36], the possibility to achieve the wave-mode conversion of surface waves into body ones with more complex engineered systems is analysed. The author proposes single or multi mass-spring compact solutions to achieve the wave-mode conversion mechanism. This idea is promoted in [37], where the metawedge layout is designed and tested with 3D FEM models. The seismic waves affect the frequency below 20 Hz [38], this typical aspect of earthquake problems has inspired the design of a metawedge for a railway application in this work. Indeed, about the same interval of frequency is excited by the passage of cargo trains [39].

## Overview

The thesis is organised as follows. In Chapter 1, the fundamental knowledge of wave propagation in elastic media is reviewed. After that, the analysis and discussion of the stiff in-filled trench and of the metawedge are presented in four chapters, which belong to three different parts. The stiff trench mitigation measure is investigated in Chapter 2 and Chapter 3, which constitute Part A. The metawedge effect is assessed in Chapter 4, which corresponds to Part B. The conclusions and the recommendations for further development are addressed in Part C.

**Chapter 1** proposes the theoretical background of wave propagation in elastic solids. This chapter aims at providing the reader with basic knowledge to understand the following analyses. The ground response to an arbitrary and uniformly distributed excitation source is computed in the frequency domain with a 1D model. The perturbation generated by a line load is also presented with a 2D model.

**Part A - Chapter 2** illustrates the field measurement campaign that has been previously performed to assess the mitigation effect of the stiff trench through in-situ tests. The site and the set measurement setup for the tests are described. The recorded time histories are processed to prove the trench effectiveness through the insertion loss parameter.

**Part A - Chapter 3** investigates numerically the physical behaviour and the mitigation mechanisms of a stiff trench. By means of a 2.5D model, the influence of different parameters is evaluated in order to define the design guidelines. The case of a stiff trench embedded in a homogeneous half-space is firstly studied and the results are discussed in detail. Then, a layered half-space is analysed to prove the validity of the mitigation mechanisms in a more realistic dispersive medium. The outcomes of the numerical simulation are compared to the in-situ test results.

**Part B - Chapter 4** introduces the metawedge as a mitigation measure for surface induced ground vibration. Its effect based on metamaterial and resonant unit cells is explained and the key wave-mode conversion mechanism is discussed. Through this technology, the incoming surface wave is diverted into the deep soil reducing the vibration amplitude at the surface. The development of a metawedge for the railway application is discussed and the influence of several design variables is considered.

In **Part C** the main conclusions of the thesis and gives some recommendations for further research are given.

# 1 | Wave propagation in soil

*In this chapter, the fundamental knowledge related to wave propagation in elastic solids is reviewed. The aim is to provide the reader with the basic theoretical background to understand the analyses presented in the following chapters. The thesis topic mainly deals with wave propagation in soil, therefore the discussed examples focus on this medium. In Section 1.1 the equations of motion and the main existing waves are presented. Subsequently, in Section 1.2, the soil response to an arbitrary and uniformly distributed loading is computed in the frequency domain with a 1D model. In Section 1.3 the level of complexity is increased through the introduction of the 2D model, which gives the soil response imposed a harmonic line load.*

## 1.1. Equations of motion

The soil is an inhomogeneous medium with nonlinear and anisotropic behaviour when loaded. For the case of traffic-induced vibration, the level of strain induced in the ground is small and thus its behaviour can be idealized as linear and elastic [17]. Therefore, the governing equations of the waves propagation in a homogeneous, isotropic and elastic continuum are further discussed.

The following derivation adopts a Cartesian coordinate system $(x, y, z)$ described by the coordinate vector $\mathbf{x} = [x, y, z]$, where the vector $\mathbf{u}(\mathbf{x}, t) = [u_x, u_y, u_z]$ expresses the corresponding displacements of a material point as functions of space and time. The constitutive equations of the generalized Hooke's law relate stresses and strains in the medium, as shown by Eq. (1.1). Similarly, the kinematic equations express the strain-displacement relations in Eq. (1.2).

$$\sigma_{ij} = \lambda \varepsilon_{kk} \delta_{ij} + 2\mu \varepsilon_{ij}, \tag{1.1}$$

$$\varepsilon_{ij} = \frac{1}{2}(u_{i,j} + u_{j,i}). \tag{1.2}$$

As suggested in [40], the index notation is employed with $i$ and $j$ that refer to the three different directions in space $(x, y, z)$. The subscript after the comma expresses the partial derivative of the function with respect to that variable (e.g., $u_{x,y} = \frac{\partial u_x}{\partial y}$).

Referring to Eq. (1.1), $\varepsilon_{kk} = \varepsilon_{xx} + \varepsilon_{yy} + \varepsilon_{zz}$ indicates the volumetric strain, while the $\delta_{ij}$ function denotes the Kronecker delta (with $\delta_{ij} = 0$ if $i \neq j$ and $\delta_{ij} = 1$ if $i = j$). Consequently, the stress tensor results symmetric $\sigma_{ij} = \sigma_{ji}$. The Lamé constants $\mu$ and $\lambda$ describe the elastic properties of the material, the former is also known as the shear modulus [41]. They can be expressed in terms of the Young's modulus $E$ and Poisson's ratio $\nu$:

$$\mu = \frac{E}{2(1+\nu)}, \qquad \lambda = \frac{E\nu}{(1+\nu)(1-2\nu)}. \tag{1.3}$$

Nevertheless, the internal energy dissipation of the material can be taken into account by including hysteretic damping in the model. As described in [42] and [43], the Lamé parameters become complex, with the imaginary part depending on the hysteretic damping coefficient $\xi_\mathrm{d}$. In Eq. (1.4) they are labelled $\mu^*$ and $\lambda^*$.

$$\mu^* = \mu(1 + \mathrm{i}\,\xi_\mathrm{d}), \qquad \lambda^* = \lambda(1 + \mathrm{i}\,\xi_\mathrm{d}). \tag{1.4}$$

The stress equation of motion is shown on the left side of Eq. (1.5). This one can be expressed in terms of displacements, substituting the strain-displacement relations into the Hooke's law and handling the resulting relation. The Navier's equations for the medium is obtained [41]:

$$\sigma_{ij,j} + \rho \mathrm{f}_i = \rho \ddot{u}_i \qquad \Rightarrow \qquad (\lambda + \mu) u_{j,ji} + \mu u_{i,jj} + \rho \mathrm{f}_i = \rho \ddot{u}_i, \tag{1.5}$$

where $\rho$ is the mass density and $\mathrm{f}_i$ is the body force per unit mass of material [40]. The double dot is adopted to express the second partial derivative with respect to time. Applying the vector form, Eq. (1.5) becomes

$$(\lambda + \mu)\nabla\nabla \cdot \mathbf{u} + \mu \nabla^2 \mathbf{u} + \rho \mathbf{f} = \rho \ddot{\mathbf{u}}. \tag{1.6}$$

The highly complex nature of the displacement equations of motion is highlighted in [40]. The system of equations has the disadvantageous feature of coupling the three displacement components [41]. So, to avoid a cumbersome solving procedure, the equations are decoupled applying the Helmholtz decomposition [44], as follows:

$$\mathbf{u} = \nabla \varphi + \nabla \times \boldsymbol{\psi}, \quad \text{with } \nabla \cdot \boldsymbol{\psi} = 0. \tag{1.7}$$

This procedure enables to write the $\mathbf{u}(\mathbf{x},t)$ vector as the gradient of a scalar and the curl of a zero-divergence vector. The additional condition on the right side of Eq. (1.7) is needed to uniquely determine the three components of $\mathbf{u}(\mathbf{x},t)$ from the four components of $\varphi(\mathbf{x},t)$ and $\boldsymbol{\psi}(\mathbf{x},t)$ [40].

The physical meaning is found in the theory of elasticity by realizing that the potentials can also be expressed through the displacement vector as $\varphi(\mathbf{x},t) = \nabla\cdot\mathbf{u}(\mathbf{x},t)$ and $\boldsymbol{\psi}(\mathbf{x},t) = \nabla\times\mathbf{u}(\mathbf{x},t)$ [45]. It becomes evident that $\varphi(\mathbf{x},t)$ contains the compressional part and $\boldsymbol{\psi}(\mathbf{x},t)$ the rotational part of the particle motion [46].

Substituting Eq. (1.7) into Eq. (1.6) and assuming the absence of body forces, the outcome reads

$$(\lambda+\mu)\nabla\nabla\cdot(\nabla\varphi+\nabla\times\boldsymbol{\psi})+\mu\nabla^2(\nabla\varphi+\nabla\times\boldsymbol{\psi})=\rho(\nabla\ddot{\varphi}+\nabla\times\ddot{\boldsymbol{\psi}}). \tag{1.8}$$

The previous equation can be rearranged[1], obtaining

$$\nabla\underbrace{\left(\rho\ddot{\varphi}-(\lambda+2\mu)\nabla^2\varphi\right)}_{=0}+\nabla\times\underbrace{\left(\rho\ddot{\boldsymbol{\psi}}-\mu\nabla^2\boldsymbol{\psi}\right)}_{=0}=\mathbf{0}. \tag{1.9}$$

The ensuing expression is satisfied requiring the two terms highlighted by the horizontal brackets to be zero. This is not the only available option but it is the most convenient one [46]. A system of decoupled equations arises and the shape of the classical wave equation is recognized, giving the opportunity to define the propagation velocities. It is concluded that the compressional wave speed $c_P = \sqrt{(\lambda+2\mu)/\rho}$, whereas the shear ones travel with $c_S = \sqrt{\mu/\rho}$. Introducing the velocities formulae, the system is rewritten:

$$\begin{cases}\nabla^2\varphi = \dfrac{1}{c_P^2}\ddot{\varphi},\\[2ex] \nabla^2\boldsymbol{\psi} = \dfrac{1}{c_S^2}\ddot{\boldsymbol{\psi}}.\end{cases} \tag{1.10}$$

It is demonstrated that two types of waves - classified as body waves - can propagate in the infinite medium with two different speeds. The compressional waves are also named P-waves or primary waves. If an excitation occurs, the compressional wave will always reach a target point faster than the shear one because $c_P > c_S$. Indeed, they are called S-waves or secondary. This is evident writing down the velocities ratio (see Eq. (1.11))

---

[1] Note that $\nabla\cdot\nabla\varphi = \nabla^2\varphi$, $\nabla^2(\nabla\varphi) = \nabla(\nabla^2\varphi)$, $\nabla^2(\nabla\times\boldsymbol{\psi}) = \nabla\times(\nabla^2\boldsymbol{\psi})$ and $\nabla\cdot(\nabla\times\boldsymbol{\psi}) = 0$ must be used

and remembering that the Poisson's ratio is $0 \leq \nu \leq 0.5$.

$$\frac{c_P}{c_S} = \sqrt{\frac{\lambda + 2\mu}{\mu}} = \sqrt{\frac{2 - 2\nu}{1 - 2\nu}}. \tag{1.11}$$

The P-wave is a longitudinal wave; this means that the particles oscillate in the same direction of the wave propagation. On the other hand, the S-wave is a transverse wave, showing the displacement of a particle orthogonal to the wave propagation direction. This observation arises a distinction between shear waves moving in two perpendicular planes can be made (eg., $xy$-plane and $xz$-plane). A difference is commonly identified between the vertically polarized waves (SV-waves) and the horizontally polarized waves (SH-waves) that travel in the vertical and horizontal plane, as depicted in Fig. 1.1. Introducing the two wave types, it is worth specifying that $\varphi$ and $\boldsymbol{\psi}$ are called P-wave and S-wave potentials [47], respectively.

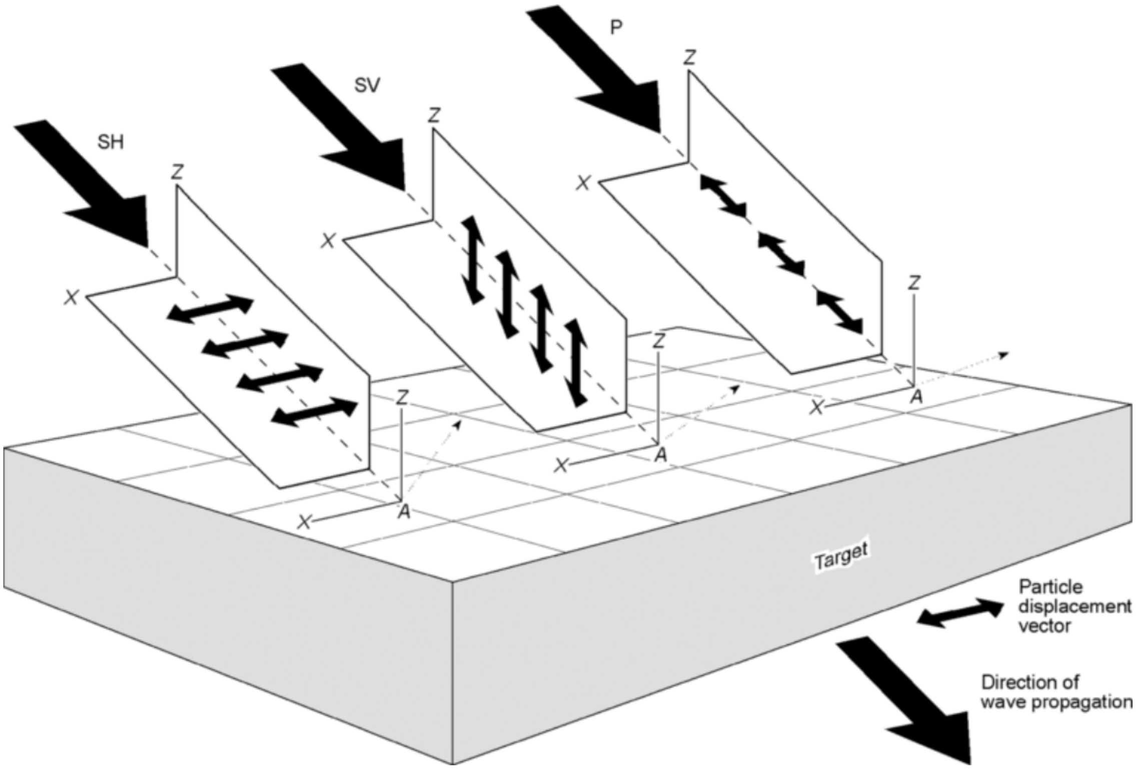

Figure 1.1: Distinction among P-waves, SV-waves and SH-waves particle oscillation [48].

If a bounded domain is considered - as in the half-space case in Section 1.3 - another type of wave may exist. This is known as Rayleigh waves, due to the first investigations conducted by Lord Rayleigh in [49]. The Rayleigh wave solution is found imposing the stress-free boundary condition at the surface level. Their effect is confined closely to the surface and it decreases exponentially with distance from the free surface. As proclaimed in [46], the Rayleigh waves are given by a combination of evanescent compressional and shear waves in the depth direction. The particle motion on the surface is characterized by a retrograde elliptical motion with respect to the wave propagation direction, with the vertical displacement component generally larger than the horizontal one. In the case of a non-dispersive medium[2], approximated expressions to compute the Rayleigh wave propagation velocity are found in literature. From [40] and [50], the $c_R$ and $c_S$ correlation reads

$$c_R = c_S\,\frac{(0.87 + 1.12\nu)}{(1 + \nu)}. \tag{1.12}$$

Surface waves are essentially two dimensional. Thanks to the geometric damping phenomenon, the energy associated with them does not spread as rapidly as the energy associated with the three-dimensional body waves [40]. Considering for example the case of a harmonic point load on a half-space, this is straightforward because the surface wave moves with circular wavefront on a plane, while the body wave propagates with a half-sphere one in the 3D medium. Indeed, the geometric damping and the shapes of the generated wavefronts are generally different. This aspect is further investigated in Section 1.3. The Rayleigh waves are widely studied for the railway research field, since they interact with surface engineering applications.

## 1.2. Soil response to an arbitrary and uniformly distributed loading (1D model)

The 1D model is the most intuitive one when solving the wave propagation in an elastic half-space. The medium response is derived through the imposition of a load at the boundary surface, which is located at $z = 0\,\mathrm{m}$. The stress is uniformly distributed over the entire area, generating a plane wavefront invariant in the horizontal directions. This is why the analysed half-space can be modelled through a one-dimensional model. The ensuing behaviour is one-dimensional because the problem is essentially invariant along with the two horizontal directions $x$ and $y$. The excitation direction is such that either compressional or shear waves appear, as visible in Fig. 1.2.

In the next sections, the receptance - defined as $u(\omega)/F(\omega)$ - is computed for both homogeneous and layered soil. The soil is assumed to be at rest prior to the loading application. This entails zero displacement and velocity at $t = 0$, which means $u_i(\mathbf{x}, t = 0) = 0$ and

---

[2] A medium is classified as non-dispersive when the phase velocity does not depend on frequency. Inhomogeneous soil and the addition of damping in the system model give examples of dispersive media.

$\frac{\partial u_i(\mathbf{x},t)}{\partial t}|_{t=0} = 0$ with $i = x, y, z$.

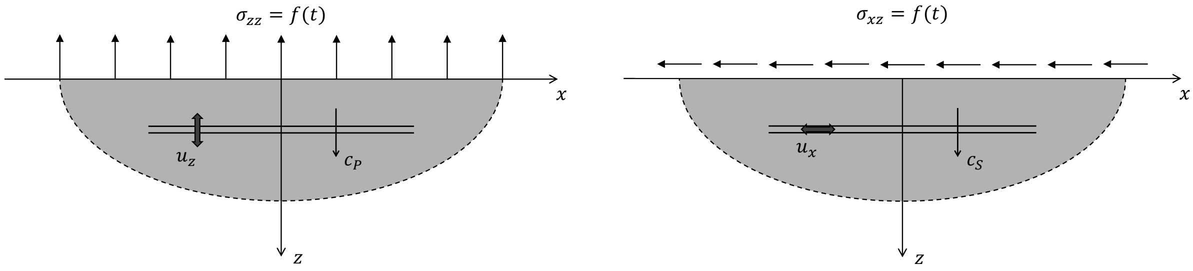

(a) Normal stress.

(b) Shear stress.

Figure 1.2: Homogeneous soil model with uniformly distributed loading.

### 1.2.1. Homogeneous soil

The first presented case takes into account a homogeneous soil excited by a normal stress at the surface (see Fig. 1.2a). From the boundary condition point of view, this implies that the stress is imposed at $z = 0\,\mathrm{m}$:

$$\sigma_{zz}(z = 0, t) = f(t), \tag{1.13}$$

where $f(t)$ is an arbitrary function of time, with $f(t < 0) = 0$. The loading does not vary along the horizontal directions. Thus, the response is independent of $x$ and $y$ coordinates, providing $\frac{\partial u_x}{\partial x} = \frac{\partial u_y}{\partial x} = 0$ and $\frac{\partial u_x}{\partial y} = \frac{\partial u_y}{\partial y} = 0$. Thanks to symmetry considerations, it is possible to affirm that $u_x(\mathbf{x}, t) = u_y(\mathbf{x}, t) = 0$ [46].

Eq. (1.5) reduces to a single equation for the displacement component along the $z$-axis, that reads

$$(\lambda + 2\mu)u_{z,zz} = \rho \ddot{u}_z. \tag{1.14}$$

This partial differential equation is the well known 1D wave equation. It is solved by passing to an ordinary differential equation by means of the forward Fourier transform over time (see Eq. (1.15)). From now on, the variables in the Fourier domain are expressed with capital letters.

$$U_z(z, \omega) = \int_{-\infty}^{+\infty} u_z(z, t)\mathrm{e}^{-\mathrm{i}\omega t}\mathrm{d}t. \tag{1.15}$$

Eq. (1.14) is written in the Fourier domain and the double prime symbol is employed to express the second derivative with respect to $z$ and reads

$$U_z'' = -\frac{\omega^2}{{c_P}^2}\, U_z. \tag{1.16}$$

The generated perturbation consists of a compressional wave that propagates at $c_P$. The general solution of Eq. (1.16) is given by a sum of two harmonic terms:

$$U_z(z,\omega) = A\mathrm{e}^{-\mathrm{i}\frac{\omega}{c_P}z} + B\mathrm{e}^{+\mathrm{i}\frac{\omega}{c_P}z}, \tag{1.17}$$

where $A$ and $B$ are unknown constants that can be obtained by the imposition of two boundary conditions. Only one condition has been explicitly discussed (cf. Eq. (1.13)) and this means that another one is needed. From the physical point of view, it is important to realise that the waves can only move from the source to the deep soil. The energy cannot be reflected at $z \to +\infty$ and consequently no waves can reach the surface. This observation is formalized by Sommerfeld's radiation condition, which can be considered as the missing boundary condition [46]. In Eq. (1.17), the right term is related to the harmonic regressive waves, which propagate in $z$ negative direction. It is concluded that $B = 0$. To find the $A$ constant the strain-displacement relation is substituted into Eq. (1.13) and the Fourier transform applied. The outcome reads

$$A = -\frac{1}{i\omega}\frac{c_P}{\lambda + 2\mu}F(\omega). \tag{1.18}$$

The receptance - ratio of displacement to force - is found as a function of $z$ and $\omega$:

$$\frac{U_z(z,\omega)}{F(\omega)} = -\frac{1}{\mathrm{i}\omega}\frac{c_P}{\lambda + 2\mu}\mathrm{e}^{-\mathrm{i}\frac{\omega}{c_P}z}. \tag{1.19}$$

The receptance absolute value is evaluated at $z = 0\,\mathrm{m}$ and the resulting curve is displayed with the solid line in Fig. 1.5. The described trajectory is a hyperbola that tends to infinite at null frequency. This is clear from Eq. (1.19), where $\frac{U_z(z=0,\omega)}{F(\omega)} \sim \frac{1}{\omega}$. Hence, the only "resonance" of a homogeneous half-space medium is located at $\omega = 0\,\mathrm{rad}/s$. From the physical point of view, it means that the undeformed soil is continuously shifted by the stress in the space. Such a situation is given by the model definition, it does not take into account any physical or spatial constraint at the bottom. To conclude, remind that the only dissipation effect is provided by the radiation damping, which reveals stronger and stronger increasing the frequency of excitation. This form of damping is associated with the fact that the energy introduced in the system can only move away from the source and that cannot be reflected back to the origin.

If a shear stress is imposed at the surface level as displayed in Fig. 1.2b, the steps to obtain the solution are the same. Nonetheless, the result in Eq. (1.19) would show $c_S$ and $\mu$ instead of $c_P$ and $\lambda + 2\mu$ and shear waves propagation would be experienced.

With a rigid bedrock inserted at a certain depth, no more a half-space is considered. The so-called shallow layer on a rigid bedrock is taken into account. The mentioned model is depicted in Fig. 1.3.

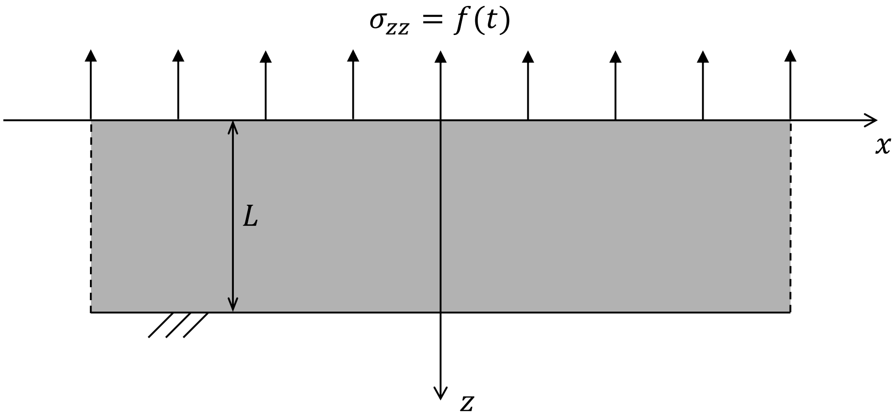

Figure 1.3: Shallow layer on a rigid bedrock model with uniformly distributed loading.

The receptance absolute value - depicted in Fig. 1.5 with a dotted line - experiences an infinite number of undamped resonances. This phenomenon appears due to the lack of a dissipation effect, the energy is entirely reflected at the bottom and it cannot travel to $z \to +\infty$. The spikes represent the resonances of the finite length layer, whereas the null values its antiresonances. The second boundary condition must be modified to properly compute the receptance expression. Imposing null vertical displacement on the rigid bedrock level is required. This means $u_z(z = L, t) = 0$, with $L$ that is the layer depth value. The Sommerfeld's radiation condition cannot be applied anymore: a perfect wave reflection occurs by definition of the rigid bedrock. For the sake of completeness, the receptance expression for a vertical stress is provided:

$$\frac{U_z(z,\omega)}{F(\omega)} = \frac{(\mathrm{e}^{+\mathrm{i}\frac{\omega}{c_P}(z-2L)} - \mathrm{e}^{-\mathrm{i}\frac{\omega}{c_P}z})}{\mathrm{i}\omega(1 + \mathrm{e}^{-\mathrm{i}\frac{\omega}{c_P}2L})} \frac{c_P}{\lambda + 2\mu}. \tag{1.20}$$

The reader could note that an indeterminate solution occurs at the surface level if $\omega = 0\,\mathrm{rad}/s$. To overcome this model limitation the limit as $\omega$ approaches 0 is solved, obtaining that $\lim\limits_{\omega \to 0} \frac{U_z(z=0,\omega)}{F(\omega)} = -\frac{c_P}{2(\lambda+2\mu)}$. It becomes clear that with a rigid constrain at the bottom the hyperbola shape disappears.

### 1.2.2. Layered soil

In this subsection, an inhomogeneous soil is analysed. This one consists of a half-space with a layer of 10 m at the top that has different material properties than the rest of the half-space. A vertical harmonic excitation is imposed at the surface level.

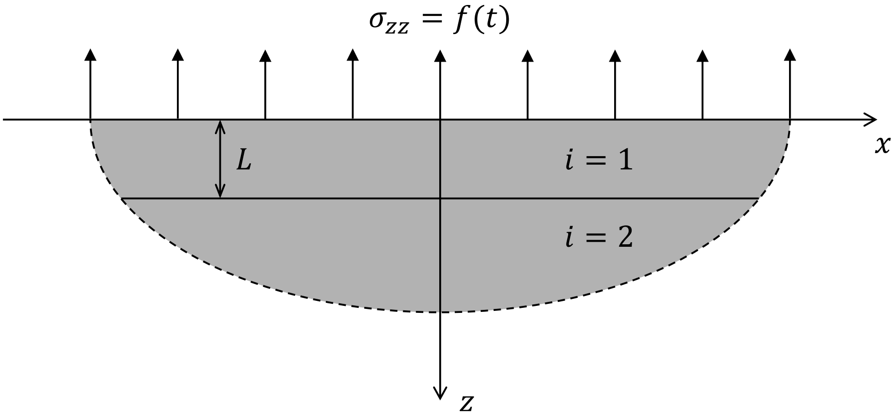

Figure 1.4: Layered soil model with uniformly distributed loading.

With the same approach adopted in the previous section, an equation of motion for each soil layer can be written in the Fourier domain, as presented in Eq. (1.21). The soil response is independent of the horizontal coordinates and the same symmetry considerations hold. Remember that the properties of the two materials differ, so the subscripts 1 and 2 are adopted to distinguish the two layers (cf. Fig. 1.4).

$$U_{z,i}'' = -\frac{\omega^2}{{c_{P_i}}^2} U_{z,i}, \qquad \text{with } i = 1, 2. \tag{1.21}$$

It follows that

$$\begin{cases} U_{z,1}(z,\omega) = A\mathrm{e}^{-\mathrm{i}\frac{\omega}{c_{P_1}}z} + B\mathrm{e}^{+\mathrm{i}\frac{\omega}{c_{P_1}}z}, & 0 < z < L, \\ U_{z,2}(z,\omega) = C\mathrm{e}^{-\mathrm{i}\frac{\omega}{c_{P_2}}z} + D\mathrm{e}^{+\mathrm{i}\frac{\omega}{c_{P_2}}z}, & z \geq L, \end{cases} \tag{1.22}$$

where $L = 10\,\mathrm{m}$. Compared to the previous case, the system dimension increases and four conditions must be imposed to find the four unknown constants $A, B, C$ and $D$. The same boundary conditions already described in Section 1.2.1 are still applicable. On the other hand, the continuity of stress and displacement must be ensured at the interface.

The following relations hold:

$$\begin{cases} u_{z,1}(z=L,t) = u_{z,2}(z=L,t), \\ \sigma_{zz,1}(z=L,t) = \sigma_{zz,2}(z=L,t). \end{cases} \tag{1.23}$$

Having the four conditions for the four unknowns, it is possible to solve the system of equations and compute the receptance at $z = 0\,\mathrm{m}$. The intermediate steps are not given for brevity, but they can easily be obtained by hand or using a symbolic mathematical software (e.g., Maple). The receptance reads

$$\frac{U_{z,1}(z,\omega)}{F(\omega)} = \frac{c_{P_1}(\mathrm{e}^{+\mathrm{i}\frac{\omega}{c_{P_1}}z} - \tilde{k}\,\mathrm{e}^{-\mathrm{i}\frac{\omega}{c_{P_1}}z})}{\mathrm{i}\omega(\lambda_1+2\mu_1)(1+\tilde{k})}, \quad \text{with } \tilde{k} = \frac{\frac{(\lambda_2+2\mu_2)}{c_{P_2}} + \frac{(\lambda_1+2\mu_1)}{c_{P_1}}}{\frac{(\lambda_2+2\mu_2)}{c_{P_2}} - \frac{(\lambda_1+2\mu_1)}{c_{P_1}}}\,\mathrm{e}^{+\mathrm{i}\frac{\omega}{c_{P_1}}2L} \tag{1.24}$$

The receptance is plotted as a function of frequency in Fig. 1.5. Realistic soil properties are used to realise this figure, the values are summarized in Appendix C.

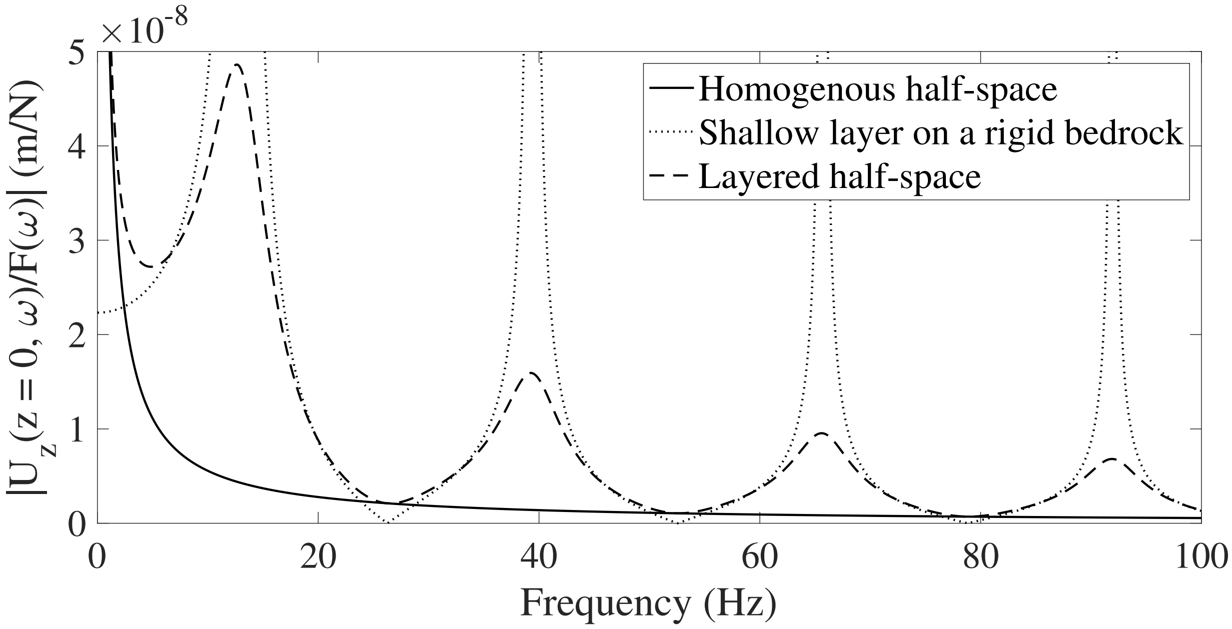

Figure 1.5: Receptance at $z = 0\,\mathrm{m}$ for homogeneous half-space (solid line), shallow layer on a rigid bedrock (dotted line) and layered half-space (dashed line).

From the physical point of view, the semi-infinite soil can be seen as a homogeneous half-space with a different material layer placed on top. This is visible in the plot, too. The dashed line describes the same asymptotic behaviour already given by Eq. (1.19). The effect of the finite layer results in infinite spikes (associated with resonances) or truly zero values (associated with anti-resonances). However, due to the radiation damping effect there are not infinite spikes or zero values. Increasing the frequency, this phenomenon is clearly more pronounced, giving smaller local maxima.

## 1.3. Lamb's problem (2D model)

A milestone in the classical theory of wave propagation is given by the so-called Lamb's problems. They get the name from Sir Horace Lamb, who significantly contributed to the study of the wave propagation in elastic solids. His leading work [51] focuses on the dynamic response of half-spaces subjected to a loading normal to the surface. Lamb obtained far field approximations, whereas closed form solutions were carried out in the last half century for very specific cases [52]. They are usefully compiled by Kausel in [53].

The Lamb's problem is presented for the case of a harmonic line load, which is depicted in Fig. 1.6. The excitation is applied on a half-space and the problem geometry is assumed invariant with respect to the $y$ direction (the same coordinate system of Section 1.2 is selected). From the previous statement it becomes evident that the problem can be studied with a 2D model.

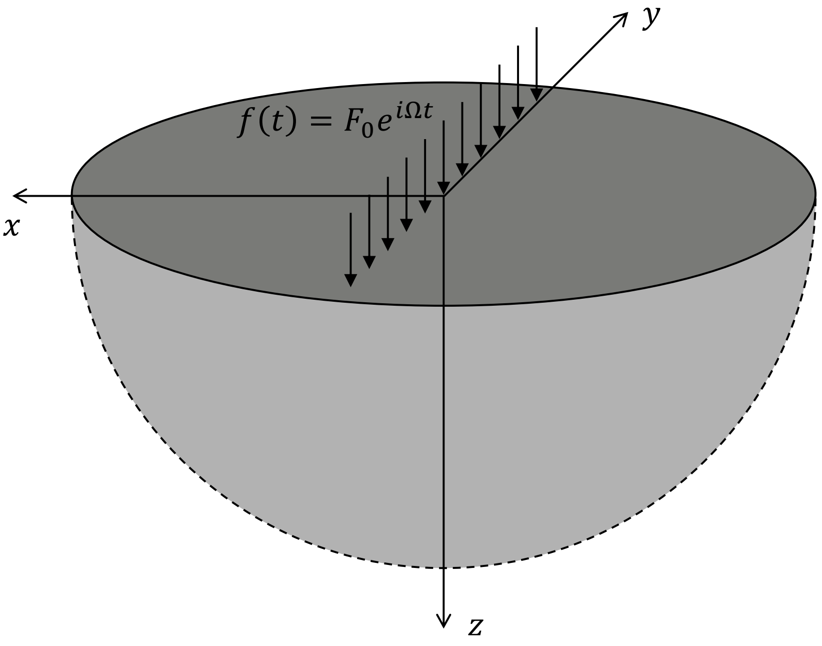

Figure 1.6: Homogeneous soil model.

The steps to derive the solution already performed in Section 1.1 are repeated to decouple the equations of motion with the Helmholtz decomposition. The line load generates a deformation in plane strain [40], leading to the displacement vector in the $xz$-plane and consequently the vector potential $\boldsymbol{\psi}$ directed perpendicular to that plane. The displacement components $u(x, y, t)$ and $w(x, y, t)$ are rewritten as $u = \frac{\partial \varphi}{\partial x} - \frac{\partial \psi}{\partial z}$ and $w = \frac{\partial \varphi}{\partial z} + \frac{\partial \psi}{\partial x}$. Consequently, the obtained two-dimensional wave equations read

$$\begin{cases} \dfrac{\partial^2 \varphi}{\partial x^2} + \dfrac{\partial^2 \varphi}{\partial z^2} = \dfrac{1}{c_P^2} \ddot{\varphi}, \\ \dfrac{\partial^2 \psi}{\partial x^2} + \dfrac{\partial^2 \psi}{\partial z^2} = \dfrac{1}{c_S^2} \ddot{\psi}. \end{cases} \tag{1.25}$$

The Fourier transform over time and space ($x$ coordinate) is applied to the system. In Eq. (1.26), the transform is defined for a generic function $f(x, z, t)$.

$$F(k_x, z, \omega) = \int_{-\infty}^{+\infty} \int_{-\infty}^{+\infty} f(x, z, t) \mathrm{e}^{-\mathrm{i}(\omega t - k_x x)} \mathrm{d}x \mathrm{d}t. \tag{1.26}$$

Knowing that $\omega = k_P c_P = k_S c_S$; system 1.25 becomes

$$\begin{cases} \Phi'' = \alpha^2 \Phi, \\ \Psi'' = \beta^2 \Psi, \end{cases} \tag{1.27}$$

where $\alpha = \sqrt{k_x^2 - k_P^2}$ and $\beta = \sqrt{k_x^2 - k_S^2}$. The square roots $\alpha$ and $\beta$ have two solutions, but only the one with positive real part is taken. Some additional remarks on the wavenumber definition may be found in [46]. The general solutions are written in Eq. 1.28 and Eq. 1.29 with the usual four unknown constants $A$, $B$, $C$ and $D$ (they are different from the ones in the previous section).

$$\Phi = A\mathrm{e}^{-\alpha z} + B\mathrm{e}^{+\alpha z}. \tag{1.28}$$

$$\Psi = C\mathrm{e}^{-\beta z} + D\mathrm{e}^{+\beta z}. \tag{1.29}$$

At this stage, the four boundary conditions are introduced. Regarding the surface, it is stated that

$$\begin{cases} \sigma_{zz}(x, z = 0, t) = f(t)\delta(x), \\ \sigma_{xz}(x, z = 0, t) = 0. \end{cases} \tag{1.30}$$

The Sommerfeld's radiation condition is applicable because the problem deals with a half-space. Waves that travel from $z \to +\infty$ to the surface cannot exist. It follows that

$B = D = 0$ because they are related to the terms of waves that propagate in negative $z$ direction. The same terms yield an exponentially increasing behaviour that is not feasible. Therefore, the last two unknowns $A$ and $C$ can be easily found from the two conditions 1.30, which must be transformed in the frequency-wavenumber domain. To finally find the displacement components in the time-space domain the inverse Fourier transform is performed. The load $F(\omega)$ is now introduced.

$$u(x,z,t) = \frac{1}{(2\pi)^2}\int_{-\infty}^{+\infty}\int_{-\infty}^{+\infty} F(\omega)U(k_x,z,\omega)\mathrm{e}^{+\mathrm{i}(\omega t - k_x x)}\mathrm{d}k_x\mathrm{d}\omega. \tag{1.31}$$

$$w(x,z,t) = \frac{1}{(2\pi)^2}\int_{-\infty}^{+\infty}\int_{-\infty}^{+\infty} F(\omega)W(k_x,z,\omega)\mathrm{e}^{+\mathrm{i}(\omega t - k_x x)}\mathrm{d}k_x\mathrm{d}\omega. \tag{1.32}$$

In this case a harmonic force is selected with $f(t) = F_0\mathrm{e}^{\mathrm{i}\Omega t}$, where $F_0$ is its constant amplitude. For this reason, it is possible to take advantage of the Delta function integral representation [54]:

$$\delta(\omega) = \frac{1}{2\pi}\int_{-\infty}^{+\infty} \mathrm{e}^{\mathrm{i}\omega t}\mathrm{d}t. \tag{1.33}$$

It follows that

$$F(\omega) = \int_{-\infty}^{+\infty} F_0\mathrm{e}^{i\Omega t}\mathrm{e}^{-\mathrm{i}\omega t}\mathrm{d}t = 2\pi F_0\delta(\omega - \Omega). \tag{1.34}$$

Inserting Eq. (1.34) in Eq. (1.31) and Eq. (1.32), the final outcome reads

$$u(x,z,t) = \frac{F_0}{2\pi}\int_{-\infty}^{+\infty} U(k_x,z,\Omega)\mathrm{e}^{\mathrm{i}(\Omega t - k_x x)}\mathrm{d}k_x. \tag{1.35}$$

$$w(x,z,t) = \frac{F_0}{2\pi}\int_{-\infty}^{+\infty} W(k_x,z,\Omega)\mathrm{e}^{\mathrm{i}(\Omega t - k_x x)}\mathrm{d}k_x. \tag{1.36}$$

The integrals are evaluated numerically. In the case of no material damping, the pole related to the Rayleigh wave lies on the path of integration resulting in an infinite integrand. To ease the numerical integration, a small amount of material damping is introduced, leading to a finite integrand for all wavenumber values and preventing numerical mistakes. Moreover, it is not possible to numerically integrate from $-\infty$ to $+\infty$. Proper limit values of $k_x$ must be selected.

At $z = 0\,\mathrm{m}$ the evaluation of the integrals was carried out by Lamb using contour integration and an expansion in the asymptotic form. After Lamb's contribution, the same problem has been studied and reproduced by several authors. The results provided in [55] are illustrated in Appendix C. Due to the approximation, this solution is only valid for large $x$.

In the ensuing equations, the contribution of the three wave types is shown. The first term is related to the Rayleigh wave while the other two to the shear and compressional ones, respectively. From the $x$ dependency, the body waves evidently present a rate of attenuation proportional to $x^{-\frac{3}{2}}$, while the surface wave is not affected by any geometric damping. It appears clear thinking about the wavefront shape generated by the line load. This is a cylinder for the body waves and a line on the surface for the Rayleigh ones. Thus, the body waves give an increasing energy spreading when the distance from the source increases, whereas the surface wave maintains the wavefront size unaltered along its path.

From the above discussion is understood how Rayleigh waves have a relatively good capability in travelling for a long distance on the surface and that they primarily exist near the surface. The same is not true for the body waves because they show a better performance in penetrating through the interior of the soil [50]. These observations solidify the reason why the two families of waves take the name of body and surface ones.

# Part A

# Assessment of a stiff in-filled trench: a railway application

# 2 | In-situ tests

*This chapter presents the measurement campaign that has been previously carried out to assess through in-situ tests the mitigation performance of a stiff trench. Section 2.1 describes the test site, providing the needed data related to the soil and the in-filled trench. In Section 2.2, the organization of the tests is explained and the excitation types are presented. The measurement setup with the location of the devices is illustrated, too. The data processing and the analysis through the Power Spectral Density and coherence function are explained in Section 2.3. In Section 2.4, the stiff trench impact and its mitigation effect assessment are evaluated by means of the insertion loss parameter, which compares the vibration level before and after the construction of the vibration countermeasure.*

## 2.1. Installation site

The in-filled trench under investigation is installed in the Dutch province of Gelderland, alongside the railway line from Utrecht to Den Bosch. The line is a classical ballasted track. Monitoring vibration campaigns have been performed due to the complaints of the lineside residents about annoyance generated by railway traffic. Moreover, the addition of an extra track and the increase of the cargo trains traffic are expected within 2030, according to a future work plan. Taking the railway line as a reference, the highest vibration amplitudes have been experienced in the northeast buildings.

For these reasons, adopting a mitigation measure has become essential to limit the undesired vibration caused by cargo trains. They have been revealed to be the most annoying source with the main energy content at low frequencies. The produced excitation is concentrated at frequencies below 15 Hz, where 6 Hz represents the dominant one [39]. This aspect is extensively discussed in Section 2.3.

The soil structure of the site has been evaluated through the cone penetration test CPT, which has confirmed the data provided by the DINOloket website [4]. The dynamic properties of the layers and the related waves propagation velocities (computed with the formulae presented in Chapter 1) are listed in Table 2.1. The soil profile is layered, consisting of softer upper layers overlying stiffer and heavier ones. This is a typical feature of the ground structure in the Netherlands.

Table 2.1: Tricht site soil properties [39].

| Layer | Depth (m) | $\rho$ (kg/m$^3$) | $E$ (MPa) | $\nu$ | $c_P$ (m/s) | $c_S$ (m/s) | $c_R$ (m/s) |
|---|---|---|---|---|---|---|---|
| 1 | 3.60 | 1700 | 15 | 0.40 | 137.5 | 56.3 | 52.8 |
| 2 | 3.25 | 1900 | 20 | 0.40 | 150.2 | 61.3 | 57.7 |
| 3 | 4.00 | 2039 | 100 | 0.35 | 280.6 | 134.8 | 126.0 |
| 4 | $\infty$ | 2039 | 150 | 0.35 | 343.6 | 165.1 | 154.3 |

The most suitable solution to decrease the vibration level has been evaluated with the support of numerical models and simulations in previous studies [39, 56]. The Cement Bentonite trench has been determined as the best countermeasure choice, thanks to its better effectiveness and more advantageous geometry control [39]. The in-filled trench has been designed to be placed 5 m far from the external track. It is characterized by a depth of 10 m, a width of 0.8 m and a total length of 320 m. Its construction phase was completed at the end of 2019.

Figure 2.1: Cement Bentonite in-filled trench construction phase [56].

Table 2.2 summarises the material and geometry properties of the constructed in-filled trench. The trench material has a larger Young's modulus $E$ than any soil layer, so it is called stiff in-filled trench.

Table 2.2: Cement Bentonite in-filled trench properties [39].

| Material | $\rho\,(\mathrm{kg/m^3})$ | $E\,(\mathrm{MPa})$ | $\nu$ | Depth (m) | Width (m) | Length (m) |
|---|---|---|---|---|---|---|
| Cement Bentonite | 1400 | 1000 | 0.2 | 10 | 0.8 | 320 |

A qualitative representation of the system lateral view is provided in Fig. 2.2. The $x$ and $y$ axes of the reference frame are taken horizontal; the former is orthogonal to the track, while the latter is parallel to the rail. The vertical axis is perpendicular to the soil surface. Note that its direction is opposite as compared to the convention adopted in Chapter 1 (see Fig. 1.6).

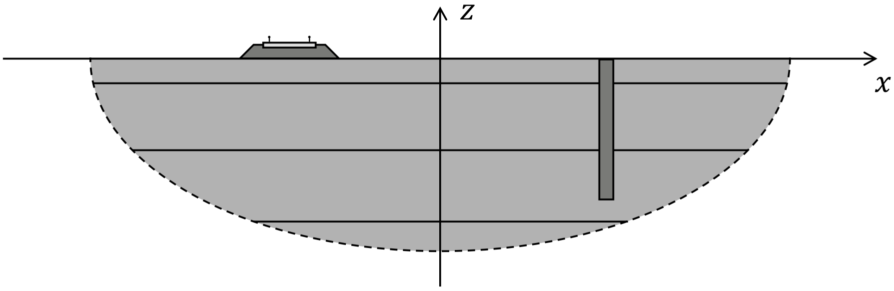

Figure 2.2: Lateral view of the in-filled trench in Tricht site (figure not to scale).

## 2.2. Test excitations and measurement setup

An extensive measurement campaign has been carried out to compare the level of vibrations before and after the stiff trench installation. The efficiency and the performance of the mitigation measure are assessed through two excitation types: train passage and dropping load. In both cases, geophones have been placed to record the velocity of the installation point along the three spatial axes $x$, $y$ and $z$.

### Train passage

In one case the vibration generated by the passage of cargo trains has been recorded at least for one week. In particular, 4839 time histories were recorded in September 2019, while there are 3704 records after the trench construction in January 2020. The geophones are not able to recognise the source that generates the vibration. Thus, only the records really given by cargo trains passage must be identified, disregarding the ones generated by other causes or malfunctioning (eg., truck passing by, people walking close to the measurement instrument or geophone saturation). Note that no distinction is made for the trains running on different tracks or directions.

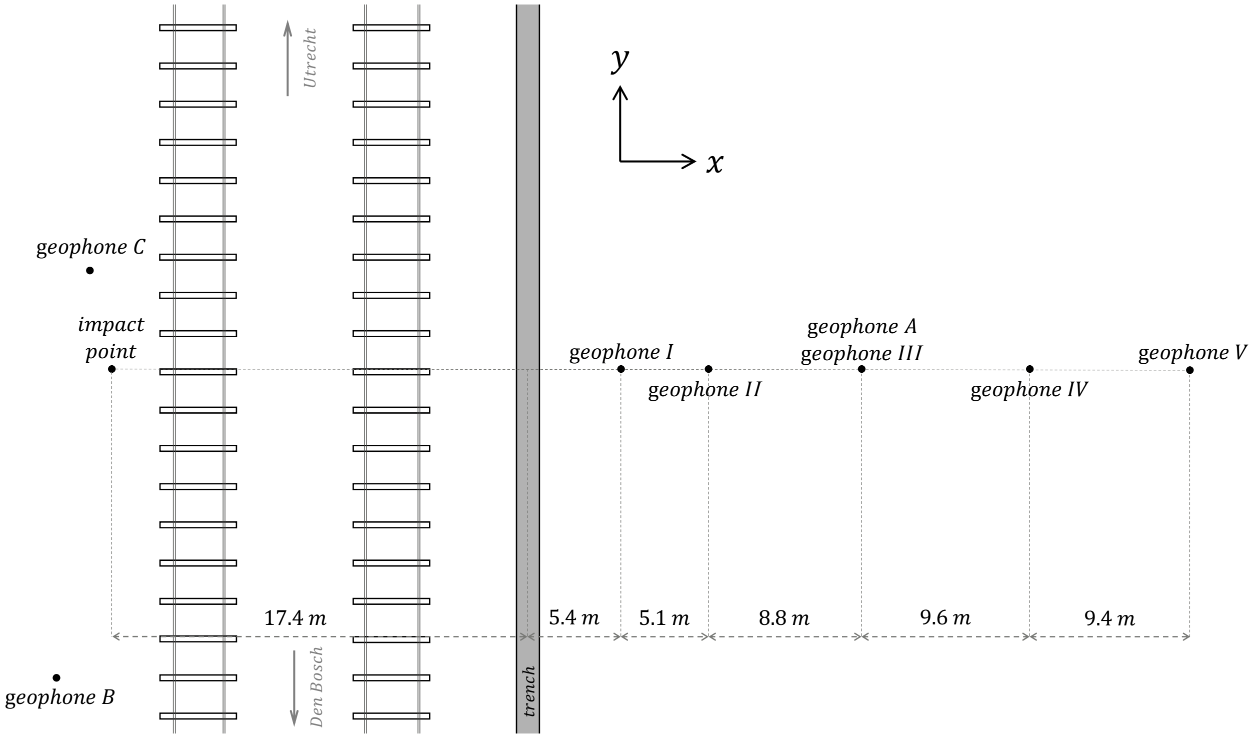

Figure 2.3: Measurement setup (figure not to scale) [56].

Only three geophones are taken into account during the train passage test. Two of them have been installed on the right side of the track, in the area affected by the highest vibration amplitude. One device is placed on the soil, while the other one is fixed to the structure foundations. The output of the second geophone is not analysed because the response is filtered by the unknown building dynamics, whose effect is not relevant for this work. The measurement setup adopted during the in-situ tests is depicted in Fig. 2.3, the ground device takes the name of geophone A. The third measurement instrument - called geophone B - has been fastened to the building foundations on the west side of the railway line. As further explained in Section 2.3, its records represent a reference point because the filtering effect of the construction is no more significant for this case. Given the large distance from the countermeasure (about 50 m) and according to a previous study [56], the trench effect on the vibration level of this location can be neglected. Indeed, the amplitude of the vibration did not experience substantial differences after its installation.

### Dropping load

The measurements of the second excitation source are related to the ground surface response due to a vertically dropping load. The test before the trench realisation was carried out in September 2019, and in January 2020 after its completion. There are 16 and 11 available drops, respectively.

The procedure consists in a 80 kg load dropped from a 2 m tall frame on an iron plate. The mass impact point and the five employed devices are shown in Fig. 2.3. They are arranged in a row that is perpendicular to the track. The different locations allow examining the effect of the trench at increasing distances. Letting the weight drop directly on the ballast is not possible, it could damage the infrastructure. Stopping the traffic on the line is not admissible, too. The frame has been placed on the west side at 17.4 m from the trench, where the added track will appear in future. Note that geophone III coincides with the geophone A employed in the train passage test described in Section 2.2. Furthermore, not all the measurement instruments are inserted into the ground, the geophone IV and geophone V are supported by concrete. Being also the farthest, they result in the least reliable due to the expected lowest signal-to-noise ratio.

There is an extra measurement device that is placed close to the impact point, at a distance of 6 m. It is depicted with the name of geophone C in Fig. 2.3. Its time histories ensure that the input nature does not significantly change before and after the stiff trench installation. The dropping load effect should always be the same from the theoretical point of view. Nevertheless, having exactly the same conditions is not possible and cannot be practically guaranteed. This is true for both the tests, not depending only on human control. For example, the different weather conditions or the wheel and rail roughness change could play an important role. Unfortunately, taking into account the changing conditions of vehicles, track and soil is unfeasible. These differences might be significant as there was a five-month period between the measurements [27]. From the beginning, remembering that this kind of measurement campaign is affected by several variables becomes important, they cannot be entirely known or kept under control. A certain level of uncertainty is always present, being aware of that becomes crucial while the data are being interpreted.

## 2.3. Vibration measurements analysis

In this section, the data processing phase is presented for both the excitation types. This allows investigating the stiff trench effect and behaviour through the in-situ tests. The

Power Spectral Density analyses the signal power distribution as a function of frequency, while the coherence function can be adopted to describe the correlation level between two records.

## Train passage

The number of available records is reduced, from 4839 and 3704 to 25 and 28, respectively. Only the time histories surely related to cargo train passage are selected. The record of the same train passage is also necessary for both the measurement instruments employed during the test. Attention is paid to a reduced number of data to enhance the quality of the final result.

Once the input data are selected, the Fourier transform is adopted to obtain the signal in the frequency domain. A generic signal is called $s(t)$ in the time domain, while its spectrum is named $S(\omega)$ in the Fourier one. The Hanning window is applied to limit the leakage effect, which is generated by the discontinuities at the extremities of the time histories. An example of geophone output in both domains is shown in Fig. 2.4.

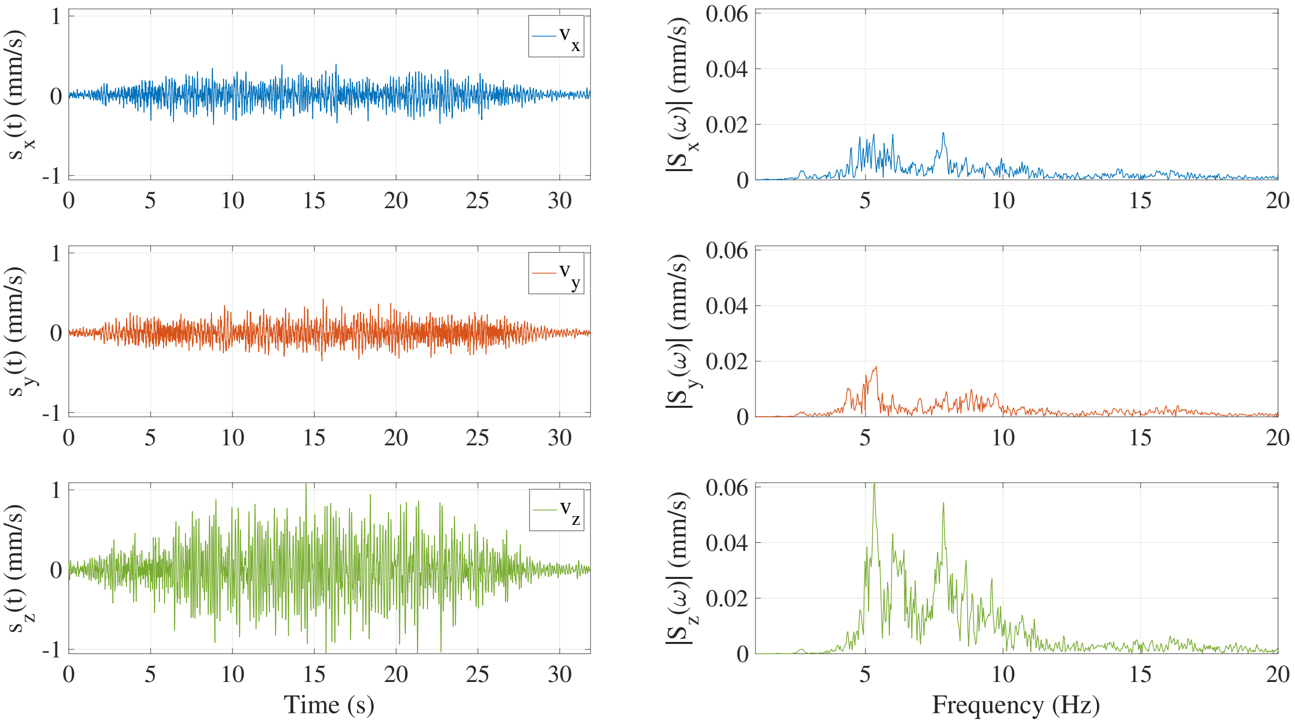

Figure 2.4: Typical time history and spectrum before the trench construction acquired by geophone A. It is associated to the passage of a cargo train in $x$ (blue), $y$ (orange) and $z$ (green) directions.

Several observations concerning the effect of a cargo train passage come to light from these plots. The time history can be separated into three parts: an increasing level when the railway vehicle approaches the receiver position, an approximately stationary level when the cargo train passes the device and a decrease when the coaches move away [8]. The largest amplitudes are visible in the stationary part of the response, which can be well approximated by a prediction characterized by the dynamic axle loads that are applied at fixed positions [57]. Cargo trains generate a long disturbance with larger amplitudes with respect to passenger ones, usually more than 25 s. From Fig. 2.4, the vertical component appears as the most excited for both the domains. Indeed, when the source is far away, the biggest contribution is provided by the Rayleigh wave that generates the largest displacements in the vertical direction, as seen in Chapter 1. This agrees with literature studies that present experimental measurements of passing trains [12–14, 27, 58], where generally only the vertical direction is investigated. The three spectra reveal that the largest amplitudes are in the range of $5 - 10\,\mathrm{Hz}$ for the $z$ direction and at slightly lower frequencies for the horizontal ones. The high frequency components are especially attenuated due to material damping in the soil [27]. Therefore, analysing the phenomenon at frequencies higher than 20 Hz is out of the scope of this work. These low frequencies are the most critical because they are the hardest to attenuate with mitigation measures [3, 22, 59]. This specific spectrum shows a peak around 6 Hz, which is the dominant frequency excited by cargo trains, as concluded in [39]. For this reason, the effort to mitigate vibration principally focuses on that frequency.

The field measurements are collected to better understand the excitation source nature and to successively evaluate the in-filled trench effect comparing the measurements before and after its construction. The power distribution is inspected as a function of frequency through the single-sided Power Spectral Density (PSD). For a generic single signal $s(t)$, it reads

$$\overline{\mathrm{PSD}}s(\omega) = \frac{S^*(\omega)S(\omega)}{\Delta f}, \tag{2.1}$$

where $S^*(\omega)$ is the complex conjugate of $S(\omega)$ that is the spectrum amplitude and $\Delta f$ is the frequency resolution. The latter is defined as the inverse of the acquisition time $T$, which means $\Delta f = 1/T$. From its definition, PSD is evidently a real function of frequency because $S^*(\omega)S(\omega) = \mathrm{Re}(S(\omega))^2 + \mathrm{Im}(S(\omega))^2$. Note that the overline marks the non averaged PSD.

To achieve a statistically correct estimation of the Power Spectral Density, the mean function of the same group of signals is obtained with a final average. This step is repeated for the two analysed cases (before and after the trench installation). Eq. (2.2) shows how working with more samples increases the outcome reliability from the statistical point of view. Having $n_s$ records of the $s(t)$ signal grouping, it follows:

$$\mathrm{PSD}s(\omega) = \frac{1}{n_s}\sum_{i=1}^{n_s}\frac{S_i^*(\omega)S_i(\omega)}{\Delta f_i}. \tag{2.2}$$

The reduction of the power that is transmitted through the stiff in-filled trench is expected to be frequency dependent. The main goal of the trench is the reduction of the energy that reaches the building on the east side of the railway line, while it has no side effects on the west edifices that experience negligible changes. The idea of using the geophone B arises from these observations. Before starting to analyse what is happening in the location monitored by the geophone A, ensuring almost the same power input before and after the trench installation is important. This is done to compare the outcomes generated by almost the same input, guaranteeing a proper assessment of the trench impact. Following this reasoning, the PSD($\omega$) is computed for the reference geophone B for the three direction components. The outcome is displayed in Fig. 2.5.

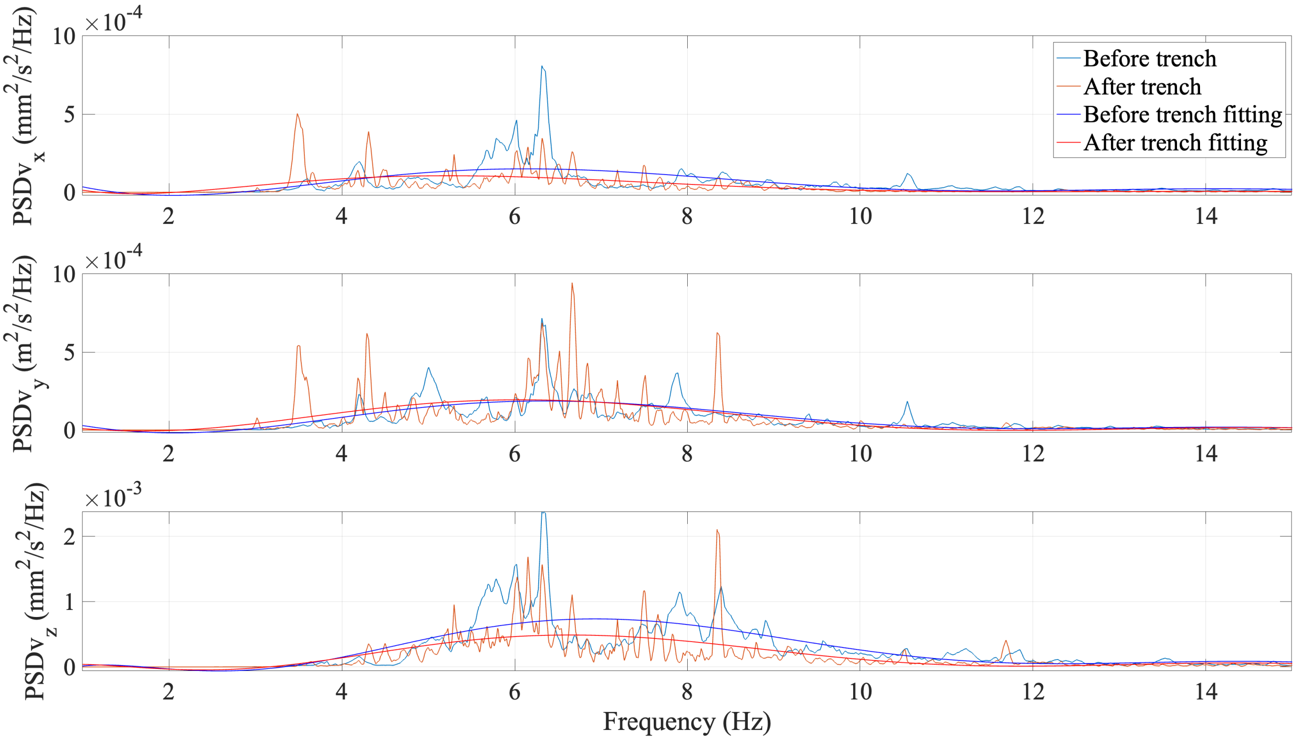

Figure 2.5: Averaged PSD in geophone B location associated with the passage of cargo train before (blue) and after (orange) the trench construction.

Concerning the case before the trench construction, the curves are derived from Eq. (2.2) with $n_s = 25$. They give the PSD($\omega$) before the trench construction. For the case after the trench installation, the curves are computed with $n_s = 28$. Despite having a perfect overlap of the two curves would be the ideal situation, this is not practically feasible. The other two curves display the related global trends, they are polynomials that best fit the data in a least-square sense. A good agreement between the curves appears, especially for the vertical direction where the higher fitting curve for the case before the trench construction states a larger energy content from the beginning. This highlights how the overall shape could help with the discussion of the final results. Note that the PSD($\omega$) in the $z$ direction are one order of magnitude larger than the ones in $x$ and $y$, showing again the bigger energy content for the vertical component.

Once the initial data check is performed through the geophone B, the mean PSD can be computed for the geophone A location. The outcome is presented in Fig. 2.6, as similarly done for the other receiver in Fig. 2.5.

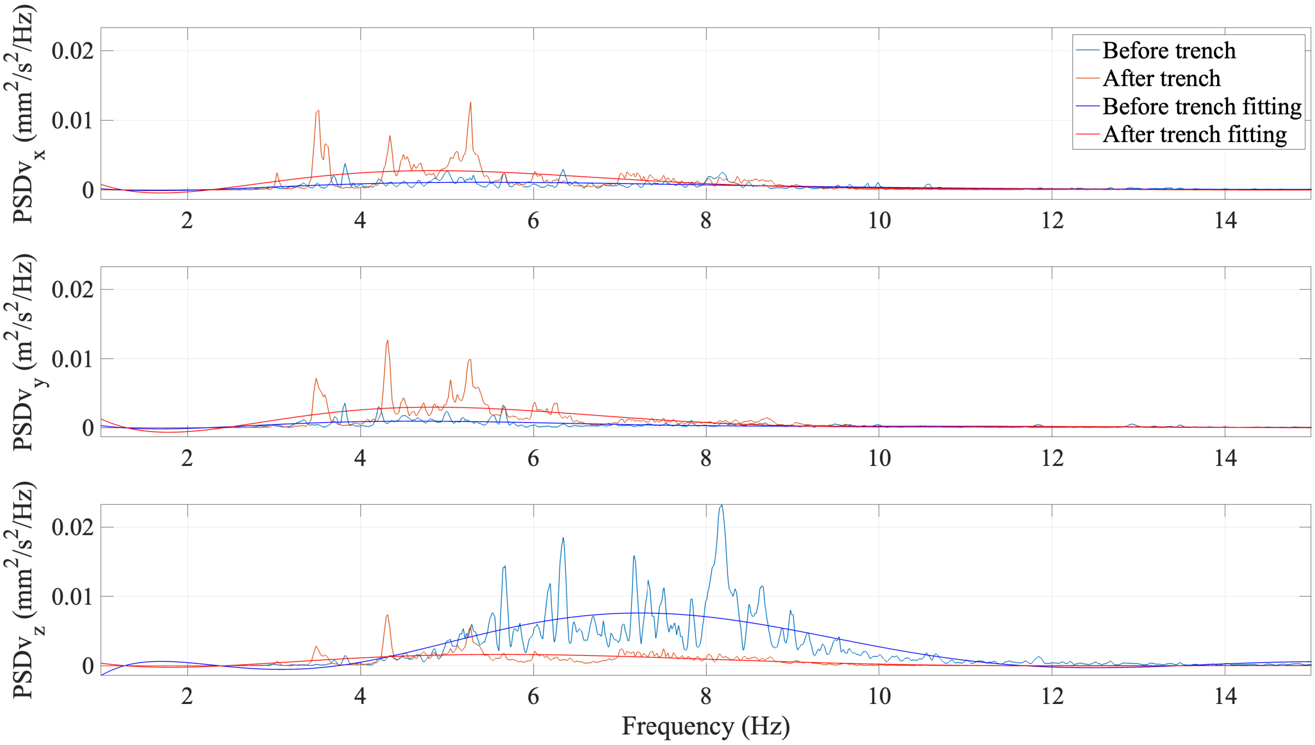

Figure 2.6: Averaged PSD in geophone A location associated with the passage of cargo train before (blue) and after (orange) the trench construction.

For the vibrations measured before the trench installation, the vertical direction appears the most excited, showing the largest energy content among the three components. The excitation contribution is mainly evident in the frequency range of 5 − 10 Hz. The horizontal directions show the largest amplitudes at slightly lower frequencies with ten times smaller peaks. Starting from the vertical direction, the in-filled trench presence ensures a pronounced reduction of the vibration level. The energy content that reaches the building strongly decreases, especially for frequencies larger than 5 Hz. The two curves seem almost superimposed until that frequency, while a clear energy content decrease is experienced above it. In Chapter 3, this phenomenon is explained though the critical frequency parameter. Regarding the other two plots for the horizontal components of velocity, the energy content seems to lightly increase after the trench construction. However, the peak below the 4 Hz for the outcome after the trench construction is also visible in Fig. 2.5. Despite its presence, a weak increase appears also above the 4 Hz. The in-situ test results after the trench installation show how the energy content in the horizontal directions seems to be of the same order of magnitude as the $z$ one. So, a beneficial decrease appears in $z$, while $x$ and $y$ seem to experience a slight increase.

## Dropping load

The same data processing procedure is implemented for the dropping load test, as described in Section 2.3 for the train passage one. The time histories do not show any particular property and their shapes resemble the usual peak generated by an impact test. Before the analysis of the trench effect, recalling the role of the geophone installed 6 m far from the impact point is important. This small distance between the impact and the device guarantees that the recorded vibration approximate the input record, which is generated by the mass into the soil. This information is not available for the train passage test. Assuming that this signal is the input to the system, the average Power and Cross Spectra can be computed to obtain the coherence function. This is a scalar function that expresses the level of correlation between two signals; it turns into 0 in case of complete lack of correlation, while it becomes equal to 1 when there is a perfect correlation. Taken two signals $A(\omega)$ and $B(\omega)$, it is defined as $\gamma^2_{AB}(\omega)$ in Eq. (2.3), which reads

$$\gamma^2_{AB}(\omega) = \frac{|\mathrm{CS}_{AB}(\omega)|^2}{\mathrm{PS}_{AA}(\omega)\,\mathrm{PS}_{BB}(\omega)}, \tag{2.3}$$

where $\mathrm{CS}_{AB}(\omega) = A^*(\omega)B(\omega)$ is the Cross Spectrum and $\mathrm{PS}_{AA}(\omega) = A^*(\omega)A(\omega)$ is the Power Spectrum of $A(\omega)$ (analogously for $\mathrm{PS}_{BB}(\omega)$ with $B(\omega)$). The coherence is calculated for the first three geophones and is displayed in Fig. 2.7 for frequencies smaller than 15 Hz. It is computed for both cases before and after the construction of the Cement Bentonite trench.

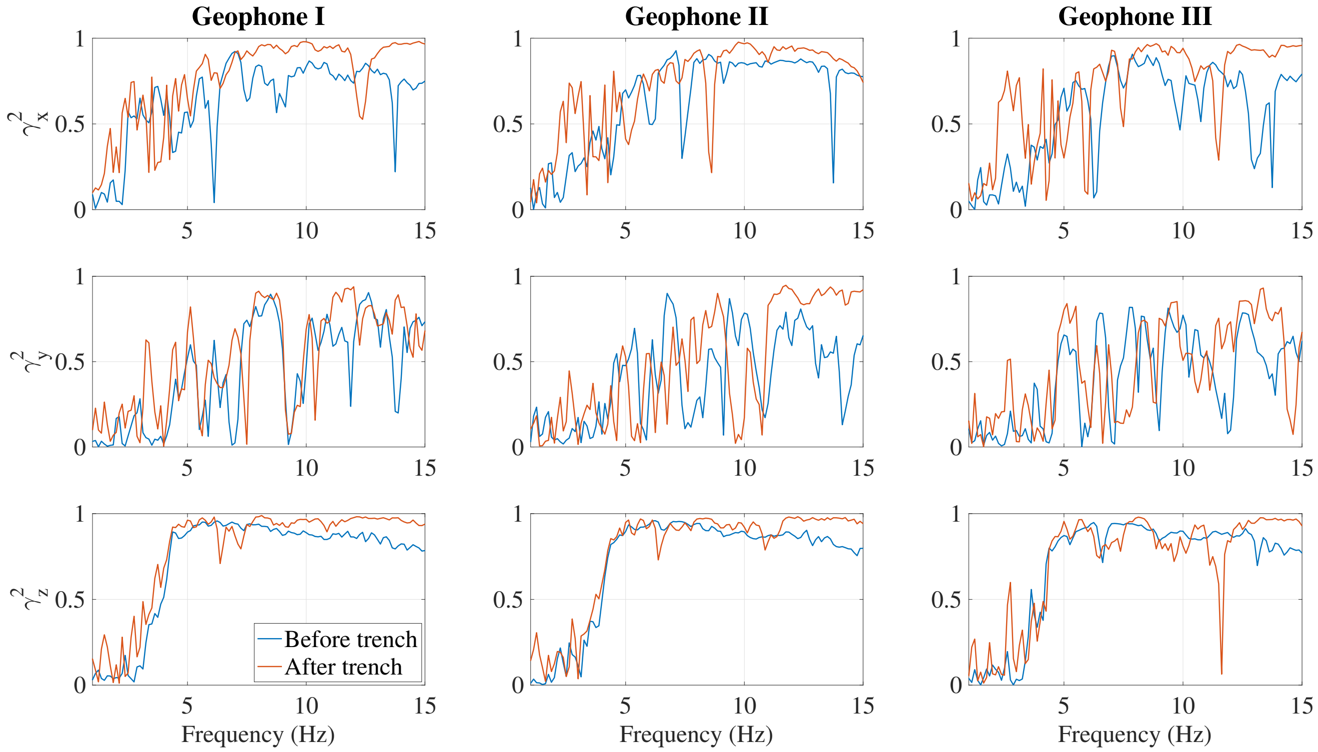

Figure 2.7: Coherence function of dropping load test computed before (blue) and after (orange) the trench construction in the three directions for the first three geophones.

Important preliminary considerations emerge from Fig. 2.7. The vertical direction is distinctly the most reliable because it shows the largest coherence values. This is perfectly in agreement with the test typology: a vertical falling mass generates strong vibration mainly in that direction, resulting in a large the signal-to-noise ratio. On the other hand, the horizontal directions display lower values and worse quality. The $y$ direction is the poorest one, a vertical load generates null displacement in that direction along the $x$-axis. Theoretically $u_y(x = 0, y, z, t) = 0$ due to the symmetry of the problem. For this reason, the $y$ horizontal direction is not taken into account during the investigation of these test results. The resulting functions in $x$ are better but still less reliable than the $z$ direction. Due to the growing general trend of the function, the signals are definitely more reliable at large frequencies than at small ones (below 5 Hz). To conclude this figure comment, moving from the left column to the right one means that the distance between the impact point and the receiving device is increasing. As predictable, the coherence values are lowering because the excitation effect generated by the mass decreases when the receiver is moved away from the source. This is why the outcomes from geophones IV and V are not depicted here and the focus is only on the first three measurement instruments of the row. Refer to Appendix C for the outcomes of the other geophones. Remind that the last two devices are positioned on pavement and not on soil as the first three.

To determine the effect of the trench, the power distribution of the geophones at different locations is studied through the averaged PSD. This is computed with Eq. (2.2) for both $x$ and $z$ direction. The results are gathered in Fig. 2.8 for the first three geophones. Consult Appendix C for the PSD in the geophone IV, geophone V and for the $y$ direction.

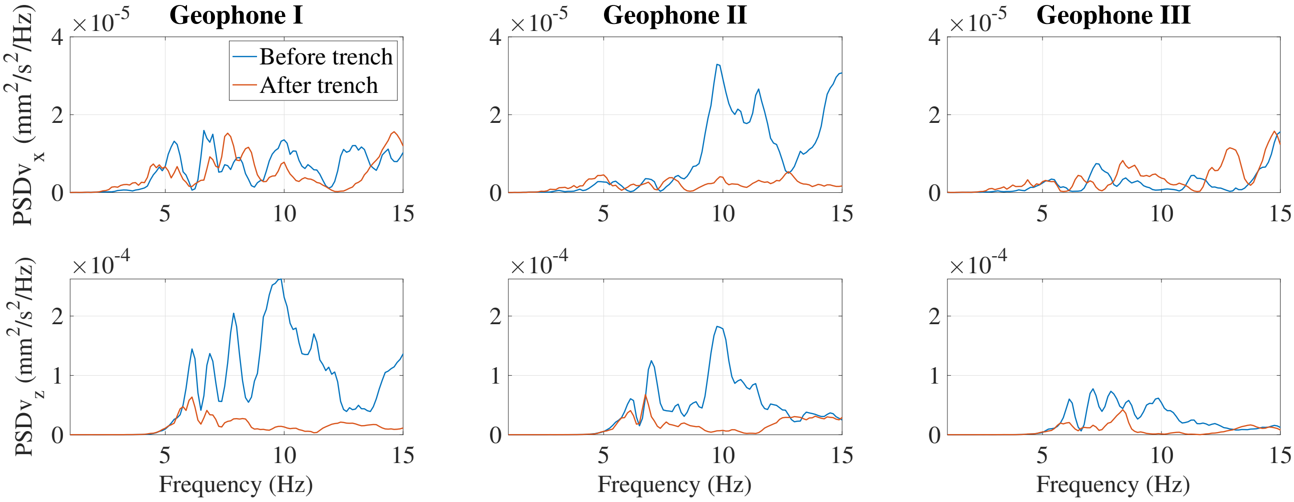

Figure 2.8: Averaged PSD for the first three geophones associated with the dropping load test before (blue) and after (orange) the trench construction.

From Fig. 2.8, it follows that the curves are coherent with the expectations. This direction is clearly the most excited before and after the trench construction (note the different scales in $x$ and $z$). The trench effectively mitigates the vibration but its effect seems to become active around 5 Hz. The curves are almost overlapped before this threshold, as observed in Fig. 2.6. The curves on the bottom row of the figure reveal how the power content of the signal decreases when moving away from the source, while the ones on the top row do not. The effect of the trench in the $x$ direction is not clear because contradictory trends arise. The trench seems very effective as in the vertical direction for the second geophone, while the other geophones do not provide a consistent performance. An increase is experienced for some frequencies, whereas a decrease is revealed for others. The last two geophones do not provide a clearer interpretation, displaying also unclear results. To state that this test shows an increase of the vibration level after the in-filled trench assembly is not possible, as slightly done for the train passage test (see Section 2.3). The beneficial contribution of the trench in the vertical direction is clearly visible for frequencies above the 5 Hz.

## 2.4. Mitigation effect assessment

The assessment of the mitigation performance of the stiff trench is presented through the computation of the insertion loss parameter. The efficiency of a mitigation measure can be quantified through the vertical insertion loss $\mathrm{IL}_z$ [8–10, 28, 29]. This work pays attention also to the horizontal directions given the results in Fig. 2.6, where the plots related to the horizontal directions show a slight decrease. Generally, it is defined as

$$\mathrm{IL}_i(x, y, z, \omega) = 20\log_{10}\frac{|U_i^{ref}(x, y, z, \omega)|}{|U_i(x, y, z, \omega)|}, \quad \text{with } i = x, y, z, \tag{2.4}$$

where $U^{ref}(x, y, z, \omega)$ is the displacement before and $U(x, y, z, \omega)$ the displacement after the introduction of the considered vibration countermeasure in the soil. The countermeasure introduces a vibration mitigation at the receiver position if the resulting insertion loss is positive, while an increase is experienced if this is negative. It can also be computed in the space-wavenumber-frequency domain.

### 2.4.1. Train passage

The insertion loss is computed for geophone A records, this receiver implicates $x = 36.7\,\mathrm{m}$ and $y = z = 0\,\mathrm{m}$ with the reference system origin that is positioned in the impact point (see Fig. 2.3). The amplitudes of the mean spectra are inserted in Eq. (2.4) for the three directions. The results in one-third-octave bands are plotted in Fig. 2.9. The bands lower than 3.15 Hz are not displayed because of lower amplitudes (see Appendix C).

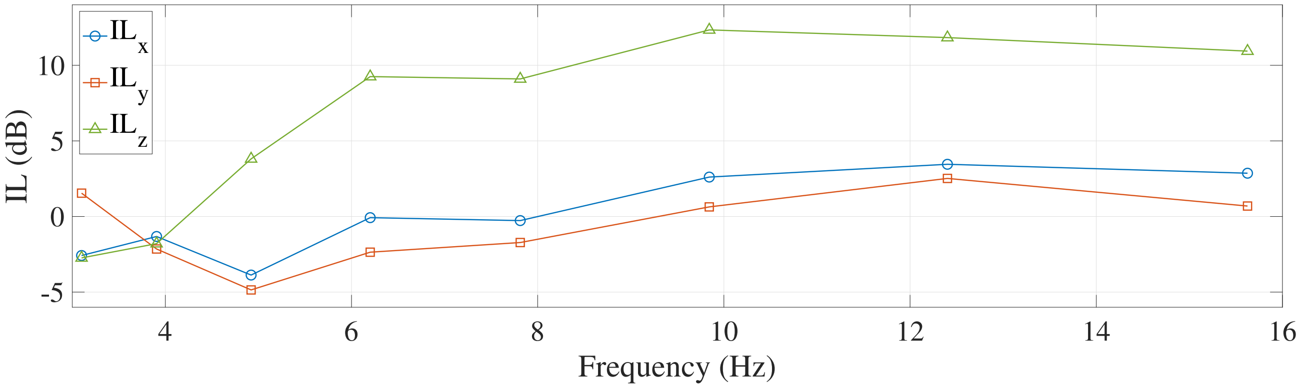

Figure 2.9: Insertion loss in geophone A location associated to the passages of cargo train in $x$ (blue circle), $y$ (orange square) and $z$ (green triangle) direction.

The mitigation performance of the trench for the vibration in the vertical direction appears evident in Fig. 2.9. Only two bands are negative (3.18 Hz and 4.00 Hz) and a positive maximum is reached near 10 Hz after a gradual growth. Despite the negative values for the first five one-third-octave bands, almost the same behaviour is observed for the IL in the horizontal directions $x$ and $y$. Also in this case, the maximum is reached but with smaller magnitudes and in the 12.5 Hz band. Furthermore, the $\mathrm{IL}_y$ curve is almost everywhere below the other lines, expressing the least attenuation performance for frequencies above the first one-third-octave band.

Recalling that the results strongly depend on the selected time histories and that they are affected by several uncontrolled and unknown variables is important. Referring to the meaningful case in [13], the insertion loss plots related to the cargo train passages show wide 95 % confidence interval estimates. Wide means that the insertion loss mean value estimation could be positive or negative for a band, even ranging from −10 dB to 20 dB in extreme cases. Moreover, the figures show wider uncertainty intervals at lower frequencies. This study demonstrates the big variability and uncertainty that can characterize these kinds of in-situ tests.

### 2.4.2. Dropping load

The insertion loss is computed for the dropping load test for the $x$ and $z$ directions with the Eq. (2.4). The results are expressed in one-third-octave bands in Fig. 2.10. Appendix C presents the results of the other two devices that are hidden in the following figure.

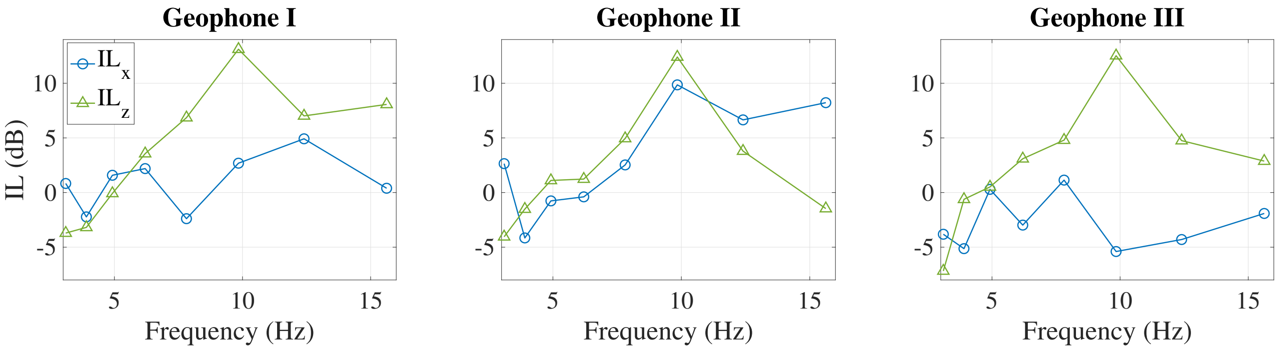

Figure 2.10: Insertion loss for the first three geophones associated to the dropping load test in $x$ (blue circle) and $z$ (green triangle) direction.

Starting from negative values - approximately below 5 Hz - the $\mathrm{IL}_z$ curves show growing trends that reach the maximum value around 10 Hz. There is a drop after the peak, involving a slightly negative value for the second geophone. The three measurement instruments give conflicting curves in the $x$ direction. For example, the geophone II exhibits an increasing shape similar to the ones of the vertical direction, whereas the geophone III is mostly negative. Neither the last two geophones - reported in Appendix C - can support the research of a prevalent trend.

### 2.4.3. Summary

In this chapter, the trench mitigation performance is assessed from the field measurements. Results of two distinct in-situ tests were available to examine the stiff trench effect. The different vibration amplitudes at the same receiver position with and without the presence of the stiff trench are compared and the insertion loss is computed. The results are presented in one-third-octave bands to present the effect of the mitigation measure in the frequency domain.

In Section 2.4.1 the outcomes originated by the passage of cargo trains are discussed. A strong decrease of vibration cases is observed in the vertical direction, for frequency above 5 Hz. The resulting insertion loss curves for the horizontal directions show similar behaviour, but positive values appear at higher frequencies. Despite these considerations, recalling the high level of uncertainty related to these types of tests becomes important.

The dropping load test investigation is presented in Section 2.4.2. The $y$ direction is not considered due to the problem geometry and consequent symmetry. The $\mathrm{IL}_z$ shows more or less the same result as the train passages test: negative values for the first one-third-octave bands (3.18 Hz and 4.00 Hz) and an increase that reaches the positive maximum near 10 Hz. The trench shows to be effective for frequencies higher than 5 Hz. For the $x$ direction, no clear trend is found.

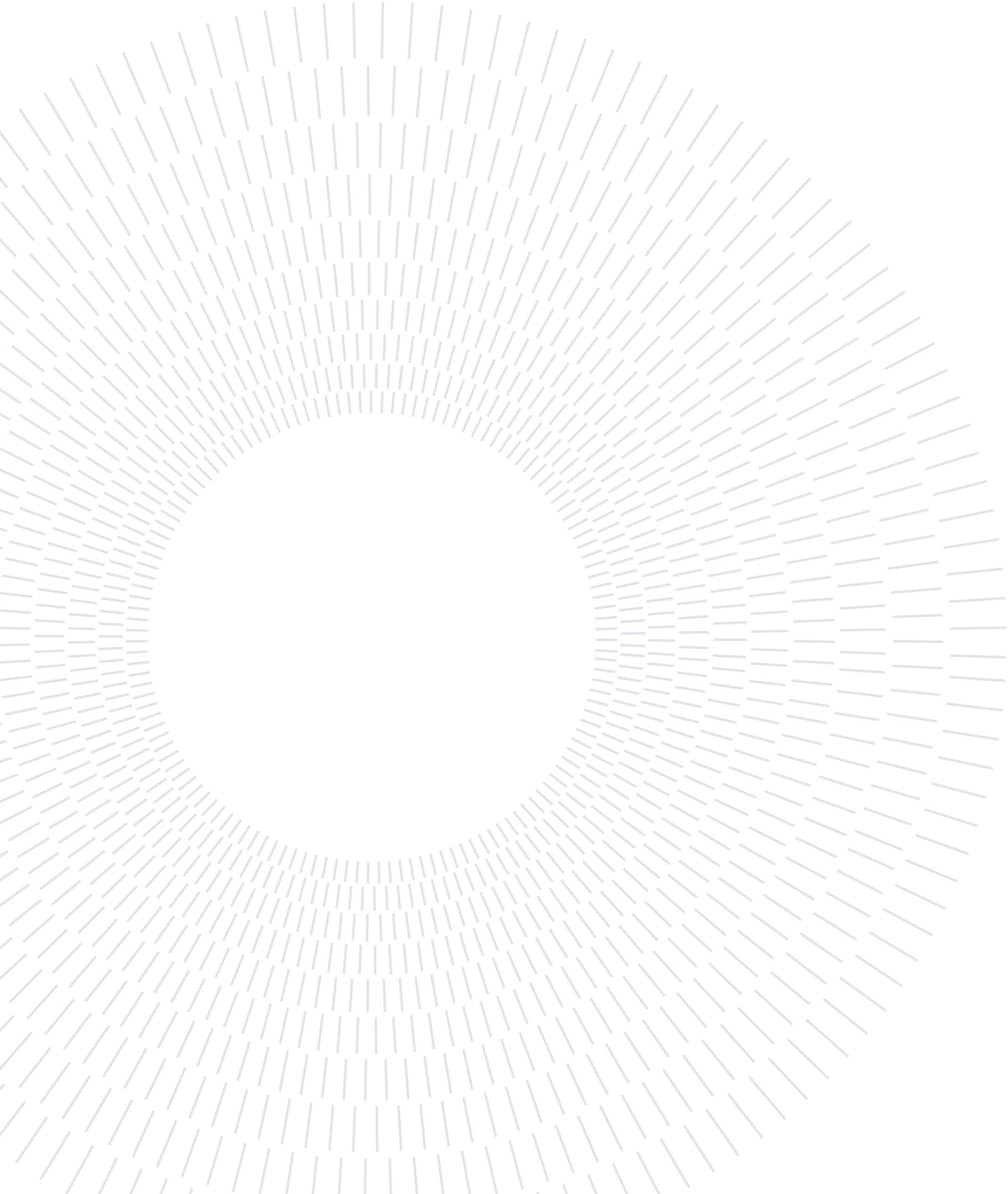

# 3 | Modelling, investigation of mitigation mechanisms and simulation

*The effect and behaviour of a stiff in-filled trench are numerically studied in this chapter. The software adopted for the analysis and the modelling procedure is presented with an example case in Section 3.1.1. The model and solution approach are validated through the comparison of results with a literature case in Section 3.1.2. In Section 3.2, the investigation of the key mitigation mechanisms is presented. To support the physical interpretation, a stiff trench embedded in a homogeneous half-space is initially proposed. In the same section, the influence of excitation frequency and Young's modulus parameter is discussed. In Section 3.3, the performance of the vibration countermeasure is further examined for a layered half-space to evaluate the effects in a dispersive medium. Concerning the vibration attenuation assessment, the comparison of the numerical and in-situ test results is provided.*

## 3.1. Modelling

The model adopted for the simulations of this work is presented in the current section. An example case is proposed to describe the modelling procedure for the different problem entities: source, transmission path, mitigation measure and receiver. The approach is validated by comparing the outcomes with a literature case. The good agreement of the achieved results is verified.

### 3.1.1. Adopted 2.5D model

A numerical 2.5D model is used to predict the response to a generic load for a half-space of soil that includes the in-filled trench. In this work, a 2.5D model is adopted for this purpose. The procedure follows the modelling approach implemented by Barbosa in

FEMIX software [17].

The model can compute the perturbation generated by an excitation source at a receiver point, taking into account the presence of a countermeasure along the transmission path. To explain how the solution is achieved and how the different entities are modelled, an example problem is introduced with a schematic diagram in Fig. 3.1. This figure displays a typical example for the model adopted in this study: the excitation point is imposed, while the displacement output is calculated at the receiver location to assess and analyse the effect of the stiff trench. In particular, the vertical harmonic unit force represents the perturbation source and the system energy input. The half-space represents the wave transmission path, while the in-filled trench represents the considered mitigation measure. For this specific case, a layered ground is chosen but the modelling procedure would not change for a homogeneous one. According to the imposed right-hand Cartesian frame, the $xz$-plane and $xy$-plane are depicted in Fig. 3.1a and Fig. 3.1b, respectively.

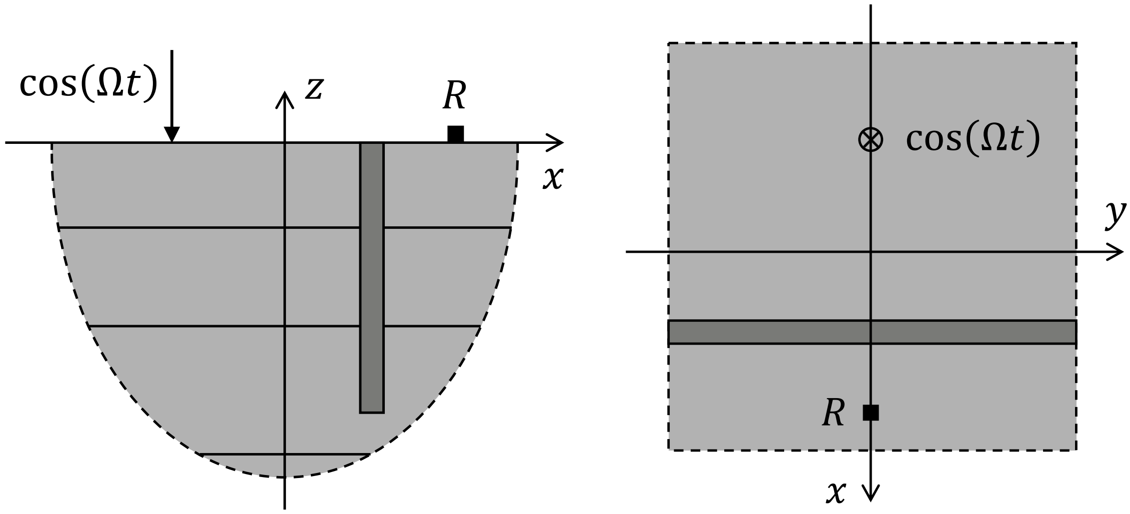

(a) Lateral view.

(b) Top view.

Figure 3.1: Model example.

Different modelling strategies are used for the soil and the trench. The wave propagation in soil is modelled with the Boundary Element Method (BEM), while the in-filled trench is modelled with the Finite Element Method (FEM). Any other finite body in the $xz$-plane would be modelled with finite elements, too. Note that the BEM relies on the discretization of just the domain boundaries, whereas in the FEM also the interior of the system domain is modelled. The motion of the soil is formulated through a finite element approach namely Thin Layer Method (TLM). This concept is graphically shown in Fig. 3.2. The two sub-domains are coupled by enforcing the compatibility of displacements and the equilibrium of forces at the interface.

Concerning the imposed system input, a non-moving vertical harmonic force of unitary amplitude is given. The excitation source is split into two equal components to avoid a punctual stress, which can cause numerical problems. These components are applied on the top nodes of a square finite element at $x = -0.1\,\mathrm{m}$ and $x = +0.1\,\mathrm{m}$, having imposed the reference frame origin at the force application point. Once the perturbation source is set, the soil response is computed at the receiver position. Only one output point is shown in Fig. 3.1, but different ones can be generally taken to obtain the displacement field at various locations.

The BEM uses Green's functions to predict the vibration at the receiver point. They are obtained with the TLM for the layered half-space auxiliary domain, which represents an intermediate domain for the soil medium. The Green's functions relate the response of a receiver with a source located anywhere in the medium [60]. In this work, the layered half-space is assumed as the auxiliary domain to keep the approach as general as possible. This choice leads to the solely discretization of the surfaces of the soil that interact with the FEM structures [17]. For the proposed example case, the boundary elements are only placed along the trench profile (see Fig. 3.2).

The most common tools used to determine the Green's functions are based on integral transformation techniques, in which the displacement field is reconstituted in the wavenumber-frequency domain and the wave equations are solved [17]. The spatial displacements can be transformed back to the space and time domain by evaluating the integrals of the inverse Fourier transform. This is the basic working principle of the 2.5D model, which can be adopted only if the problem geometry is assumed invariant in one of the two horizontal directions. This means that the geometry does not change along that direction. In this way, the reduction of the dimension of the problem by one is obtained; passing from a generic 3D analysis to a summation of 2D independent cases. The 2.5D approach is more efficient than a full 3D approach, while avoiding the simplifications present in a purely 2D model [1]. The computation time is also drastically lower [28], but systems with finite dimensions cannot be modelled along the horizontal direction because the constant geometry assumption holds. This applies to the $xz$-plane in Fig. 3.1a since its geometry is considered invariant along the $y$-axis, as depicted from the surface top view in Fig. 3.1b. The 2.5D methodology is often implemented for the study of railway induced vibration, since in the majority of cases the track cross section geometry and the soil profile do not significantly change in the longitudinal direction [61]. This procedure has been widely applied by several authors to assess the mitigation effect of longitudinally invariant mitigation measures. Some examples are offered in [7, 20, 23, 28, 62, 63].

In FEMIX, the Green's function for the auxiliary layered half-space is obtained in the transformed wavenumber-frequency domain through the Thin-Layer Method (TLM). This technique is based on the finite element discretization of the auxiliary domain in the direction of layering, which is the $z$-axis according to Fig. 3.2. The displacement field within the discrete layers is approximated through interpolation functions along the vertical axis, whereas analytical solutions determine the wave motion in the horizontal directions thanks to the assumed constant and homogeneous properties. To adopt the semi-discrete character of the TLM in an unbounded half-space domain, the Perfectly Matched Layer (PML) technique is implemented in FEMIX [64]. A schematic representation of the coupling between the PML and the TLM is proposed in Fig. 3.2. The PML numerical tool is used for absorbing boundary purposes; in other words, it suppresses the unwanted reflection of waves in infinite media modelled through discrete finite systems [17]. The implemented PML is based on the coordinate stretching approach, which - as suggested by the name - stretches the real space to a complex one. The wave decays exponentially within the PML and no reflection can appear thanks to the absence of impedance contrast at the boundary [65].

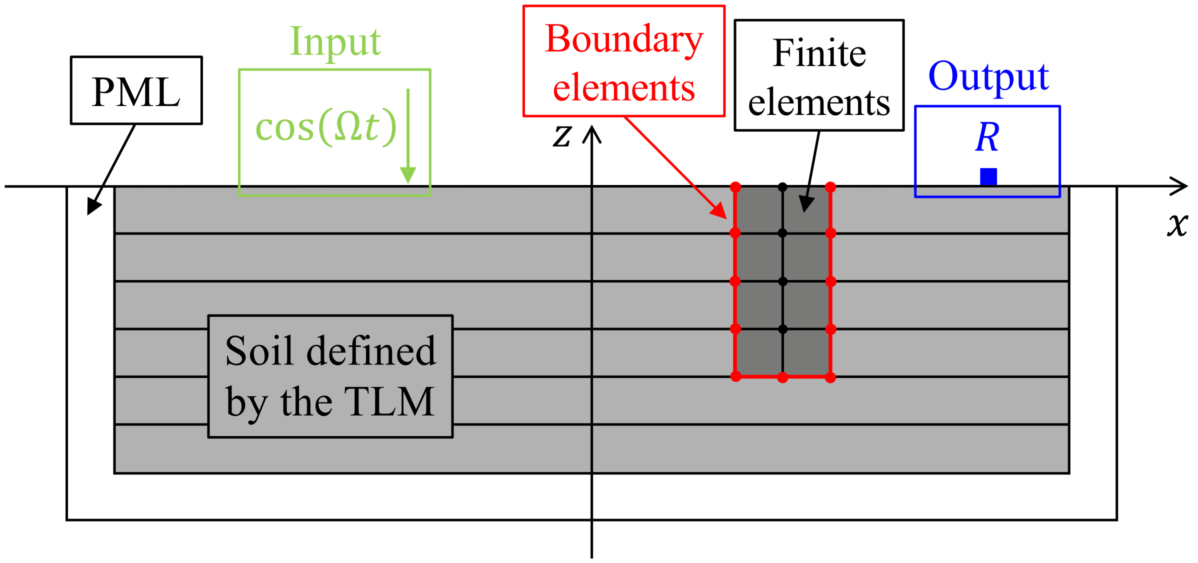

Figure 3.2: Software modelling approach.

From the practical point, an input file is written by the user to define a model in the FEMIX environment. This file is generated with a MATLAB script in the current work. Its role essentially consists in the definition of the problem geometry and in the imposition of frequency and longitudinal wavenumber at which the problem is solved. Referring to the example case in Fig. 3.1, this information is set for the $xz$-plane, while the third dimension along the $y$-axis is recovered through the computation of the inverse Fourier transform over the longitudinal wavenumber $k_y$. The constant geometry is specified through the type and position of the finite elements and consequent boundary ones. The force position and the receiver points are expressed, too. Note that only square elements with four nodes are used for the simulations of this work. Depending on the selected frequencies, the finite element dimension must be adjusted to guarantee the presence of at least 10 elements per shear wavelength $\lambda_{S,min}$ at the largest frequency considered $f_{max}$ [28]. Taking $p$ as the distance between two consecutive nodes belonging to the same square finite element, this means $\lambda_{S,min} \geq 10\,p$ with $f_{max}\,\lambda_{S,min} = c_{S,Trench}$. As depicted in Fig. 3.2, the TLM discrete layers must coincide with the nodes of the embedded finite elements. The outputs produced by FEMIX are post-processed in MATLAB. Note that the solution computed at null longitudinal wavenumber ($k_y = 0$) implies the plane strain condition, which involves no deformation and no displacement along the $y$-axis. In this way, a 2D model is considered, this approach is adopted to obtain several results in Chapter 4.

The new contribution of the current work has been mainly carried out during the writing phase of the software input file. This has been adapted to obtain the needed results from the desired model. The post-processing phase of the simulation outputs has been entirely developed by the author.

### 3.1.2. Model validation

Before analysing the trench effect on the soil response and its behaviour, the solution method is validated by comparing the results with a literature case. The stiff trench embedded in homogeneous soil considered in [8] is chosen as a reference. This study is part of the set published by the research group of the Katholieke Universiteit Leuven University, which is identified as a reference point for the investigation of the stiff trench performance.

The same geometry of the proposed case is reproduced with identical proprieties of trench and soil. The in-filled trench with a 7.5 m depth and a 2 m width is placed in between the vertical harmonic excitation and the receiver, which are 15 m distant. The properties of the half-space and trench materials are summarised in Appendix C. The trench is called stiff because it is stiffer than the surrounding soil.

Imposing the same convention of the previous section the vertical insertion loss - computed with Eq. (2.4) - is plotted as a function of longitudinal slowness $K_y = k_y/\omega$ and frequency $f = \frac{\omega}{2\pi}$ (i.e., $\mathrm{IL}_z(x = 15, K_y, z = 0, \omega)$). Note that $k_y$ represents the wavenumber along the horizontal $y$-axis. The inverse Fourier transform is applied to display the insertion loss for the unit monoharmonic load in the three-dimensional space. The real part of the vertical displacement Re($u_z$) is shown for the original homogeneous half-space and the one with the trench. In [8], the figures for $f = 25\,\text{Hz}$ and $f = 50\,\text{Hz}$ are available. For brevity, just the latter case is compared in Fig. 3.3, although also the former one shows a very good agreement.

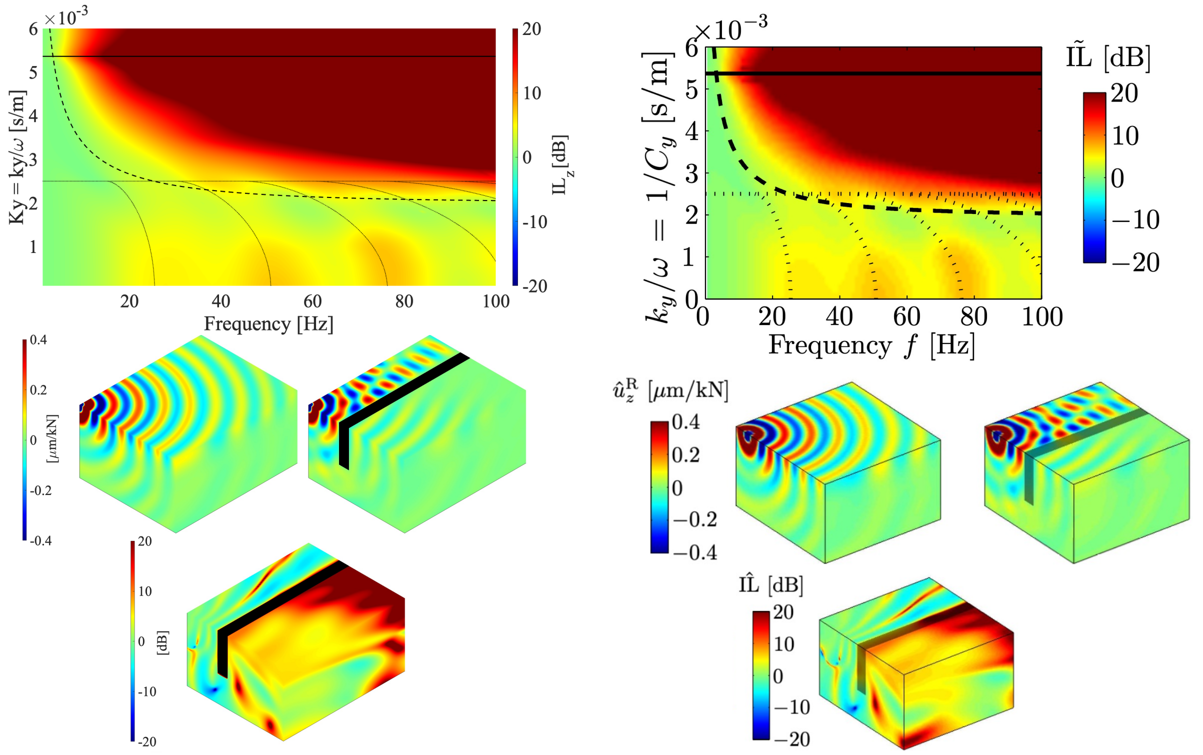

(a) Results from FEMIX.

(b) Results from [8].

Figure 3.3: Model validation through results comparison with [8]. $\text{IL}_z(x = 15, K_y, z = 0, \omega)$ (first row), $\text{Re}(u_z(x, y, z, \Omega = 2\pi \times 50\,\text{Hz}))$ without and with in-filled trench (second row) and $\text{IL}_z(x, y, z, \Omega = 2\pi \times 50\,\text{Hz})$ (third row).

Starting from the top plot of Fig. 3.3a and Fig. 3.3b, it appears evident that the insertion loss is correctly computed because the colour pattern appears very similar. A good match is also shown by the superimposed black curves. The black solid line is the Rayleigh wave slowness that is $K_R = \frac{1}{c_R}$ for the non-dispersive homogeneous soil, the black dashed line is the Timoshenko's beam bending mode around the $x$-axis and the black dotted lines show the phase shift between wavefronts in the case with and without the trench. Despite the slightly different plot sizes, the other plots are also experiencing a good matching. The black band represents the in-filled trench.

From the good agreement of the outcomes in Fig. 3.3, the model is validated. It is adopted in the coming sections to investigate the vibration mitigation mechanisms of a stiff in-filled trench.

## 3.2. Investigation of mitigation mechanisms and effect of modelling parameters

This section focuses on the analysis of the effect and performance of the stiff in-filled trench. It aims to provide an overview of this vibration countermeasure, highlighting the key mitigation mechanisms. The study of the trench embedded in a homogeneous half-space is pursued. This is the simplest model to examine the stiff trench mitigation mechanisms. The influence of different modelling parameters is also investigated. In particular, different excitation frequencies are studied and the effect of the Young's modulus variable is discussed for both soil and trench. The study presents the response in the space-wavenumber-frequency domain as well as in the space-frequency one.

### 3.2.1. Case study: stiff trench embedded in a homogeneous half-space

The mitigation mechanisms of a stiff in-filled trench embedded in a homogeneous half-space are discussed in this section. The problem geometry is modelled using FEMIX software with a 2.5D method, assuming a longitudinal invariant cross section. This methodology is described in Section 3.1.1. The track is disregarded and the half-space is assumed homogeneous to facilitate the physical interpretation of the mitigation mechanisms, as suggested in similar researches [8, 27].

The soil is characterized by density $\rho = 2039\,\mathrm{kg/m^3}$, Young's modulus $E = 150\,\mathrm{MPa}$ and Poisson's ratio $\nu = 0.35$. The hysteretic damping coefficient $\xi_\mathrm{d}$ is set equal to $2.5\,\%$. The medium has the same properties as the last semi-infinite layer of the Tricht site (cf. Table 2.1). To keep a strong link with the Dutch application, the Cement Bentonite material is chosen for the embedded trench, which has the same width and depth as the constructed one in Tricht (cf. Table 2.2).

The ground is excited at the surface level by a unit vertical harmonic point force. The right-hand Cartesian frame is placed with the origin at the loading position. The $x$-axis is perpendicular to the trench, while the $y$ one is parallel to it. The measurement setup employed during the dropping load test (described in Chapter 2) is recalled by the position of the source, vibration countermeasure and receiver. The trench is placed 17.4 m far from the frame origin and the receiver is located at the first geophone location, which implies a distance 22.8 m from the loading. The invariant geometry of the system in the $xz$-plane is depicted in Fig. 3.4.

The decision to investigate the wave field generated by the unit vertical harmonic force is made to facilitate the physical interpretation. Indeed, any type of loading - including moving loads - can be represented by a summation of harmonic components. Considering a passing train in the model would increase the level of complexity [28]. In [57], the author demonstrated how the stationary part of a time history generated by a moving train can be well approximated by a simplified model involving dynamic axle loads applied at fixed locations, as a series of incoherent vertical points. The designed model recalls this aspect, too. Furthermore, the vertical harmonic excitation conveniently simulates the dropping load test, making possible the comparison of experimental and numerical results. The settled simulation allows observing the trench performance depending on materials properties and excitation frequency, investigating how the different physical mechanisms act. The effect of the incoming wave characterized by different incident angles can also be observed.

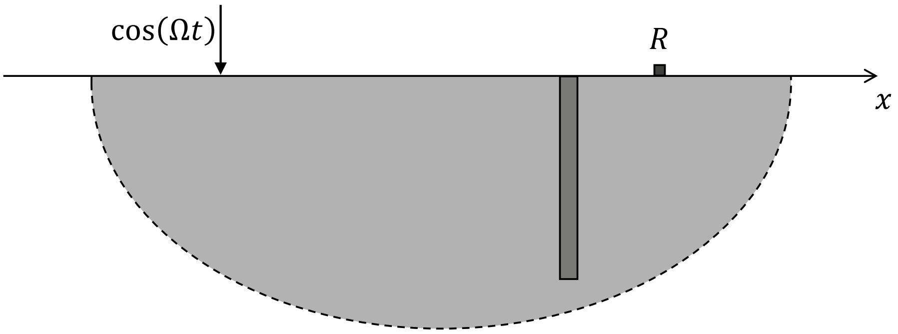

Figure 3.4: Lateral view of the wave propagation problem in the homogeneous half-space with stiff in-filled trench, the grey cube with the $R$ letter indicates the receiver location.

The effect of a generic trench is essentially based on two key phenomena: the reflection effect and the stiffness effect [8]. These mitigation mechanisms are explained in Section 3.2.2 and Section 3.2.3, respectively. Depending on the trench nature, one effect prevails over the other. The performance of open trenches is completely dominated by the reflection of the incoming wave, while the behaviour of stiff trenches is mainly controlled by the stiffness effect and just a limited contribution of the reflection effect could be experienced [13].

Note that this work focuses on the analysis of a stiff trench. The idea is to refer the study to the stiff Cement Bentonite trench installed along the railway line in the Tricht site. This case study is extensively described and discussed in Chapter 2.

### 3.2.2. Reflection effect

The reflection of incoming waves plays a fundamental role for open trenches while a marginal one for stiff in-filled trenches. This mechanism is based on the reflection of a significant part of the incoming waves, leading to less energy transmission beyond the countermeasure. The reflected part guarantees that a beneficial vibration mitigation is achieved behind the trench. The open trench mitigation measure poses realization issues due to safety and stability reasons, these generally limit its depth to shallow ones [28]. Another drawback is the rainwater filling the hole, which can negatively alter its performance. The trench can be filled with soft materials to solve these side effects, finding the best compromise for the final performance of the system. If this solution is adopted, the behaviour of the soft in-filled trench resembles that of an open one [20]. Indeed, the reflection effect becomes crucial for soft in-filled trenches, too.

The reflection effect beneficially reduces the vibration level when the depth of the mitigation measure is at least 0.6 times the Rayleigh wavelength $\lambda_R$ in soil [27]. Thus, to ensure a sufficient wave reflection, the following relation should hold $d \geq 0.6\lambda_R$, where $d$ is the trench depth. This rule of thumb is demonstrated experimentally in [66] and numerically in [21, 28]. This implies that for the considered trench with a depth of 10 m, the reflection effect acts for $f > 9.3\,\mathrm{Hz}$. Above this frequency, the penetration depth of the approaching Rayleigh waves is small compared to the trench depth, making the reflection contribution effective for the reduction of the transmitted waves [8]. This phenomenon does not advantageously depend on the trace wavenumber $k_y$, differently from the stiffness effect [27].

From the engineering point of view, the simple relation between the trench depth $d$ and the Rayleigh wavelength $\lambda_R$ has an important practical relevance. In the design phase of a trench or for an existing one, it is possible to get an idea of the frequencies at which the trench would start reflecting waves, ensuring an effective vibration attenuation thanks to this effect.

### 3.2.3. Stiffness effect

When the in-filled trench material is stiffer than the surrounding soil, the key factor determining its effectiveness strongly depends on the stiffness contrast between the two media [20]. Stiff in-filled trenches act as wave impeding barriers that result particularly efficient at sites with soft soil. Increasing the stiffness of the mitigation measure is beneficial for its mitigation effect [10]. In the following, the stiffness effect mitigation mechanism is investigated in the space-wavenumber-frequency domain and in the space-frequency one. A better understanding of the mechanism is presented to improve the vibration attenuation performance of the stiff trench solution.

## Analysis in the space-wavenumber-frequency domain

To highlight this physical mitigation mechanism, the trench performance is quantified by the insertion loss parameter in the space-wavenumber-frequency domain. The outcome of Eq. (2.4) is plotted in Fig. 3.5 for the vertical component. The figure displays the vertical insertion loss at the receiver position ($x = 22.8\,\mathrm{m}$ and $z = 0\,\mathrm{m}$) as a function of longitudinal slowness $K_y = k_y/\omega$ and frequency $f$. Remember that positive values of $\mathrm{IL}_z$ express the decrease of the vibration amplitude, whereas negative ones the increase.

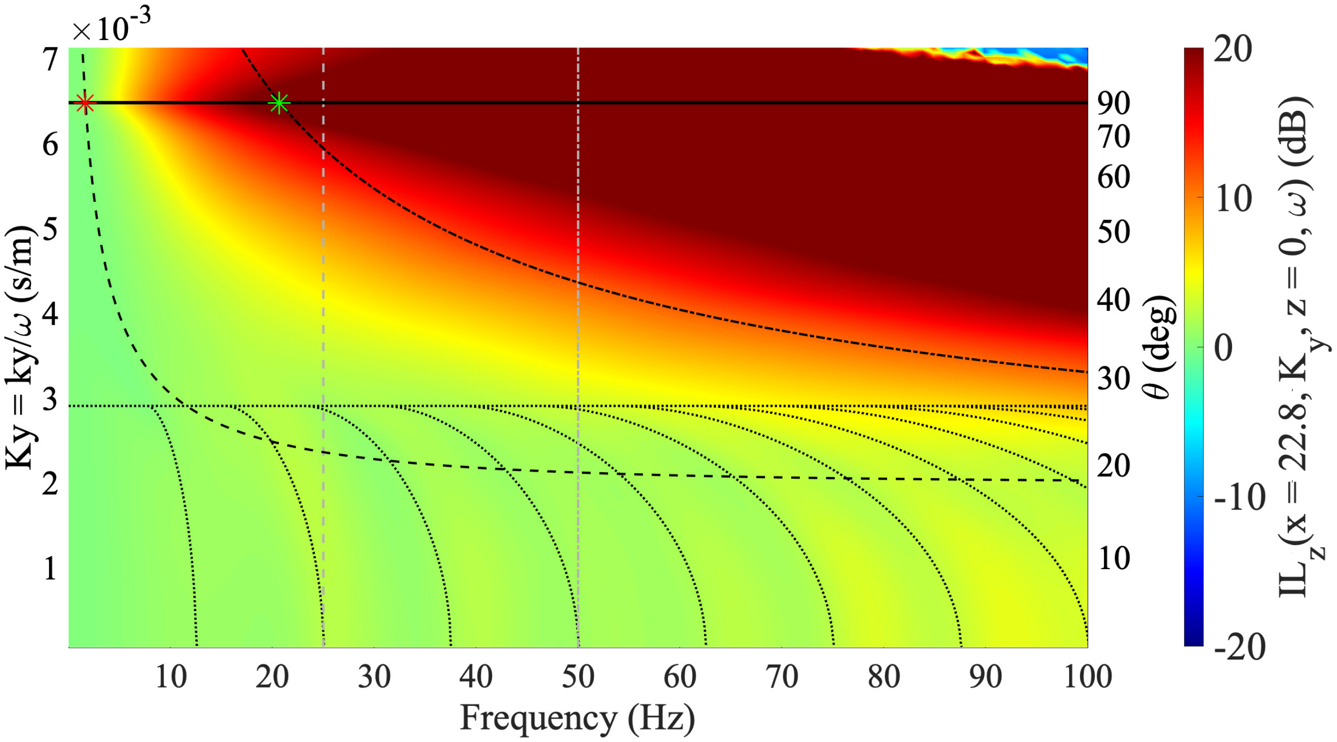

Figure 3.5: Vertical insertion loss $\mathrm{IL}_z(x = 22.8, K_y, z = 0, \omega)$ for the reference stiff in-filled trench embedded in homogeneous half-space. Superimposed are the dispersion curve for Timoshenko's beam bending mode around the $x$-axis (black dashed line) and $z$-axis (black dashed-dotted line), the dispersion curve Rayleigh wave (solid line) and the frequency-slowness curves that show the phase shift of compressional waves between wavefronts in the case with and without the trench (dotted line). The stars represent the critical frequency for bending mode around the $x$-axis (red) and $z$-axis (green). $f = 25\,\mathrm{Hz}$ (grey dashed line) and $f = 50\,\mathrm{Hz}$ (grey dashed-dotted line).

The thick horizontal black line in Fig. 3.5 is the dispersion curve of a Rayleigh wave propagating in the $y$ direction. Due to the non-dispersive nature of the homogeneous half-space, the associated slowness is constant and equal to $K_R = 1/c_R = 6.5\,s/\mathrm{m}$. This line delineates an important threshold because the lateral wavenumber $k_x = \sqrt{k_R^2 - k_y^2}$ becomes imaginary for $k_y > k_R$. This signifies that, above this line, the wave does not propagate in the $x$ direction because it becomes evanescent, resulting in a very limited response of the free field [28]. For this reason, that area of the plot does not play a significant role and can be disregarded.

Below the horizontal line, a clear portion of the plot shows significant insertion loss values. As already observed in different studies [8–10, 12, 28, 29], it occurs when the longitudinal slowness exceeds the dispersion curve corresponding to the bending mode around $x$-axis of an infinitely long Timoshenko's beam that models the trench. In other words, the bending stiffness of the mitigation measure hinders the transmission of waves when the longitudinal wavelength $\lambda_y$ is smaller than the free bending wavelength $\lambda_b = \frac{2\pi}{k_b}$, but not shorter than the Rayleigh wavelength $\lambda_R$ [17]. This means $k_b < k_y < k_R$, which is equivalent to $\lambda_R < \lambda_y < \lambda_b$.

The analytical model from the Timoshenko's theory well approximates the bending modes of the trench, as demonstrated for an in-filled trench in [8]. In the current work, attention is also paid to the bending mode around the $z$-axis. In some cases, it seems to better mark the high insertion loss zone. Its activation constructively contributes to the mitigation effect of the stiff trench.

The colour map in Fig. 3.5 could be misleading because the $\mathrm{IL}_z$ values are related to the imposed colour legend. The set limit of 20 dB expresses a ten times amplitude reduction, but all the values larger than 0 dB translate a favourable vibration decrease. To avoid this graphic limitation, the same outcome is plotted in Fig. 3.6 along three axes to provide a more objective result. This figure is not influenced by the colour interpretation since the $z$-axis displays the vertical insertion loss value. For simplicity, only the dispersion curves related to the bending modes are overlapped together with the horizontal line $1/c_R$. Values larger than $K_R$ are not reported on the horizontal axis $K_y$.

In accordance with the Timoshenko's beam theory [67], the dispersion relation for the bending waves in the wavenumber-frequency domain reads

$$EIk_y^4 - \rho I\left(1 + \frac{E}{\kappa\mu}\right)\omega^2 k_y^2 + \left[-\rho A\omega^2 + \frac{\rho^2 I}{\kappa\mu}\omega^4\right] = 0, \tag{3.1}$$

where $I$ is the moment of inertia, $E$ is the Young's modulus, $\mu$ is the shear modulus, $\kappa$ is the shear coefficient and $A$ is the cross sectional area of the beam. For the beams with a rectangular cross section, the shear coefficient can be computed as $\kappa = 10(1+\nu)/(12+11\nu)$ [68]. The expression in Eq. (3.1) provides the dispersion curve relation between the bending wavenumber $k_y = k_b$ and $\omega$. An analogous expression of the dispersion curve is available in [69].

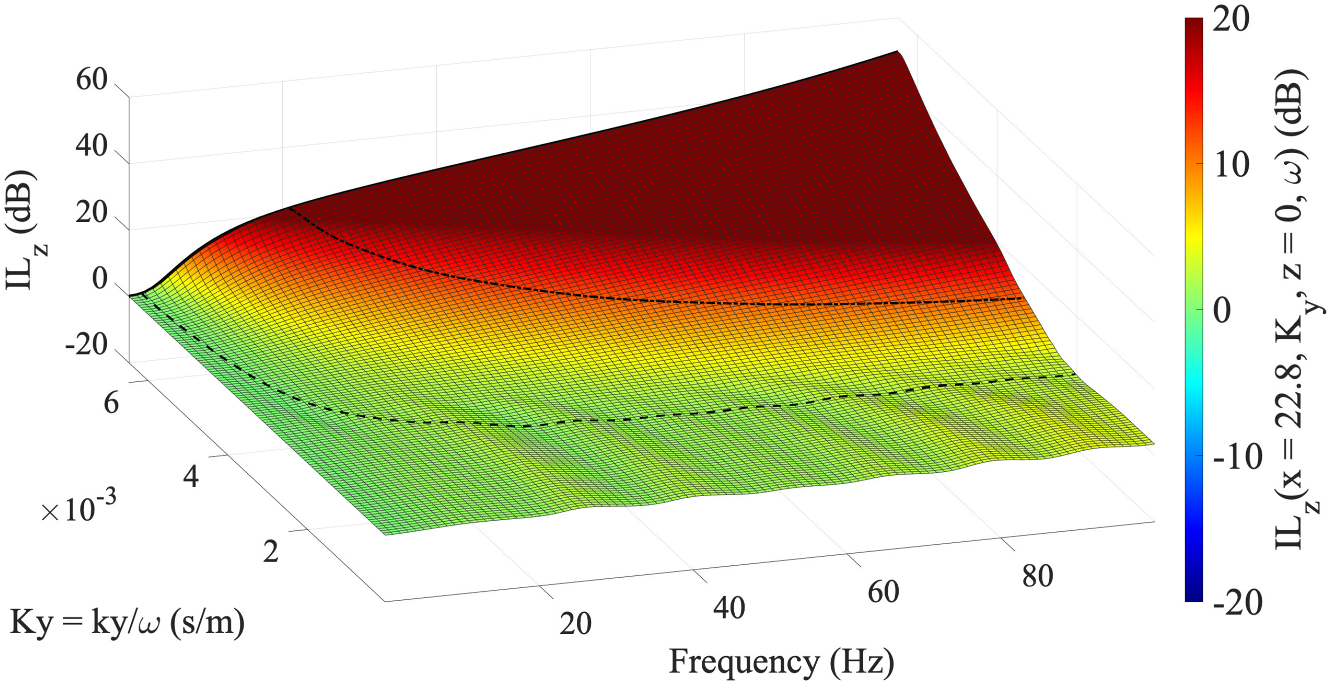

Figure 3.6: Vertical insertion loss $\mathrm{IL}_z(x = 22.8, K_y, z = 0, f)$ for the reference stiff in-filled trench embedded in homogeneous half-space. Superimposed are the dispersion curve for Timoshenko's beam bending mode around the $x$-axis (dashed line) and $z$-axis (dashed-dotted line), the dispersion curve Rayleigh wave (solid line).

A width $b$ and a height $h$ are assumed for the general beam cross section $A = bh$. The dispersion curve corresponding to the bending mode around the $x$-axis is found replacing in Eq. (3.1) the generic bending stiffness $EI$ with $EI_x$, where $I_x = bh^3/12$. Analogously, $EI_z$ is inserted in the equation to obtain the bending mode around the $z$-axis, where $I_z = hb^3/12$. The associated wave propagation modes are schematized in Fig. 3.7. Since the load is vertical, the bending mode around the $x$-axis is expected to primarily determine the mitigation mechanism of the in-filled trench [29].

If the rotatory inertia and the shear deformation are neglected, the Timoshenko's beam theory from [70] reduces to the Euler-Bernulli one. This simplification leads to the free bending wavenumber $k_b = \sqrt[4]{\frac{\rho A \omega^2}{EI}}$ [10]. This expression makes clear that increasing the bending stiffness of the beam $EI$ has a beneficial impact on the bending stiffness effect. Indeed, the dispersion curves corresponding to the bending modes are shifted down in Fig. 3.5, enlarging the area of high insertion loss. This effect is further examined in Section 3.2.5, where the effect of a stiffer trench characterized by larger $E_{Trench}$ is shown. The previous expression also explains why the dispersion curve of the bending mode around the $x$-axis is below the one related to the bending mode around the $z$-axis in Fig. 3.5. The analysed trench is characterized by $I_x > I_z$ because $b = 0.8\,\mathrm{m}$ and $h = 10\,\mathrm{m}$.

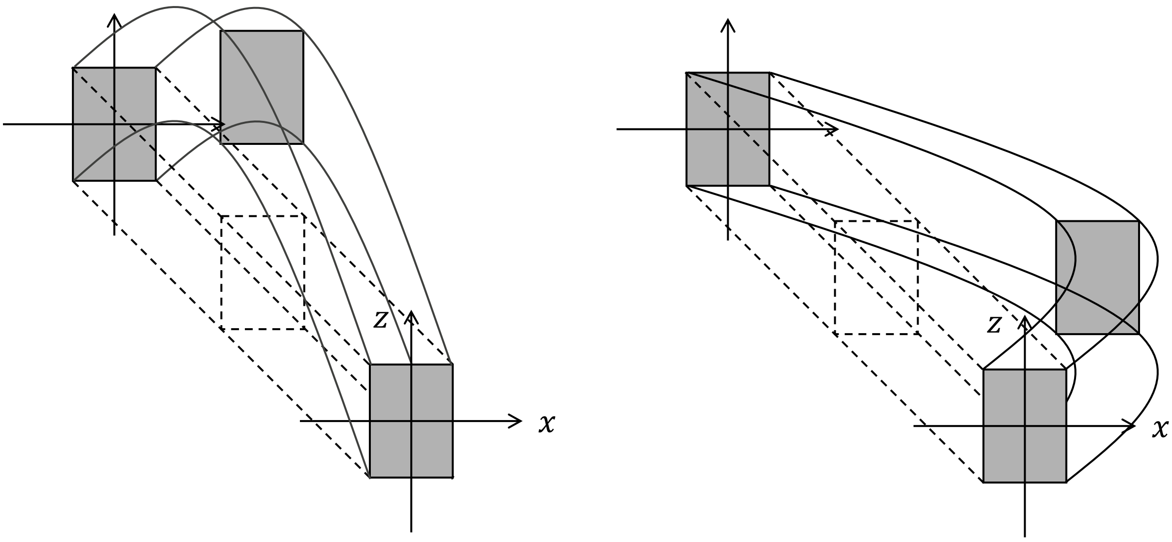

(a) Bending mode around the $x$-axis. (b) Bending mode around the $z$-axis.

Figure 3.7: Timoshenko's beam bending modes, the reference beam is drawn with dashed lines.

The previous discussion shows how the interpretation of Fig. 3.5 is based on the interaction of the bending waves in the stiff trench and the Rayleigh ones in the soil. At low frequencies, the bending slowness $K_b$ is larger than $K_R$ and the waves propagate through the trench. Above a certain frequency (i.e., critical frequency), the wave field contains longitudinal slowness values $K_y$ that are larger than $K_b$ but smaller than $K_R$. The transmission of these waves is prevented by the stiff trench that offers positive values of the insertion loss. The critical angular frequency is found by the intersection of the free bending wave dispersion curve and Rayleigh one. The analytical expression is provided in [9]:

$$\omega_{\mathrm{c}} = c_R^2 \sqrt{\frac{\rho A}{EI}} \sqrt{\frac{E \mu \kappa}{\left(E - \rho c_R^2\right)\left(\mu \kappa - \rho c_R^2\right)}}. \tag{3.2}$$

The above equation gives the values of the stars in Fig. 3.5. Concerning the bending mode around the $x$-axis, it results $\omega_{c,x} = 2\pi \times 1.6\,\mathrm{Hz}$, whereas the other critical frequency is $\omega_{c,z} = 2\pi \times 20.5\,\mathrm{Hz}$.

Eq. (3.2) reinforces the concept that the performance of a stiff trench mainly depends on the stiffness difference between the two materials. To obtain a small critical frequency and so a good performance at low frequency, having a softer soil and a stiffer in-filled trench is favourable. This leads to smaller $c_R$ and larger $E_{Trench}$. A beneficial effect is also achieved by increasing the moment of inertia $I$; if this is done through the depth $h$ the reflection effect (explained in Section 3.2.2) becomes more influential, too. From the previous considerations, the stiff trench is evidently not able to mitigate vibration below the $\omega_{c,x}$. In this region, its presence is completely negligible. Introducing the Euler-Bernulli theory simplification, the critical angular frequency is approximated by $\omega_c \simeq c_R^2 \sqrt{\frac{\rho A}{EI}}$.

The critical frequency parameter represents a simple and practical tool to understand the efficacy threshold of the stiff in-filled trench. It guarantees a smooth design guideline to estimate the range of ground vibration reduction.

The stiffness effect, investigated above, resembles the so-called coincidence in acoustics [10]. The sound wave incident on an infinite panel is freely transmitted at the coincidence frequency $f_{co}$, at this frequency value the panel bending wavenumber matches the trace wavenumber (i.e., the projection of the acoustic wavenumber along the partition) [71]. For $f < f_{co}$, the wave transmission follows the so-called mass being dominated by the panel mass, while it is controlled by the plate bending stiffness above this threshold ($f > f_{co}$). At the coincidence frequency, the maximum transmission occurs and a dip appears in the transmission loss value [71]. In the soil wave problem, the vibration mitigation arises above the coincidence frequency - here called critical frequency $\omega_c$ - thanks to the bending stiffness of the in-filled trench [9]. On the other hand, the inertia effect does not have any role in vibration attenuation for $\omega < \omega_c$.

On the right vertical axis of Fig. 3.5, the wave propagation angle $\theta$ is displayed. It can be computed as $\theta = \sin^{-1}(K_y/K_R)$ [9]. This angle links the insertion loss value to a point in the three-dimensional space that lies on the $x = 22.8\,\mathrm{m}$ line, for this specific case. In particular, $\theta = 0\,\mathrm{deg}$ corresponds to the frame $x$-axis, whereas $\theta = \pi/2$ is reached for $K_y = K_R$ independently of the frequency.

This angle can be employed to understand where the bending mode is activated in the space domain for the $K_b < K_y < K_R$ region. Taking the name of critical angle, it is computed as $\theta_c(\omega) = \sin^{-1}(K_b/K_R)$ for $K_y = K_b$. Note that $K_b$ depends on $\omega$. Depending on the specific case, it can be more or less pronounced but a significant reduction of the vibration level is generally experienced for $\theta > \theta_c(\omega)$. The critical angle $\theta_c(\omega)$ can be obtained as a function of the soil and stiff trench material properties from the following analytical expression [9]:

$$\sin\theta_c(\omega) = c_R \sqrt{\rho \frac{E + \mu\kappa + \sqrt{(E - \mu\kappa)^2 + \frac{4E(\mu\kappa)^2 A}{\rho I \omega^2}}}{2E\mu\kappa}}. \tag{3.3}$$

At high frequencies, the critical angle can be approximated through a constant frequency independent value as $\sin\theta_c = \sqrt{\frac{\rho}{\mu\kappa}}$ [10]. This simplification is valid when the dispersion curve for the beam bending mode asymptotically approaches a constant value. The simplified formula gives $\theta_{c,x} = 17.9\,\text{deg}$, finding a good agreement with the dashed line in Fig. 3.5.

In Eq. (3.2) and Eq. (3.3) the Rayleigh wave velocity $c_R$ is not a function of $\omega$. It is a constant value because the non-dispersive homogeneous half-space is studied. It becomes frequency dependent with a dispersive medium, such as the layered half-space analysed in Section 3.3.

The dotted curves in Fig. 3.5 express the phase shift of the wavefronts for the compressional waves. So, a faint regular pattern is visible for the small slowness values at higher frequencies. The compressional waves travel faster through the stiff trench than in the softer half-space, introducing into the system a phase delay between the two scenarios. This phenomenon is expressed through the relation between longitudinal slowness $K_y$ and $\omega$ that follows [8, 9]:

$$\left( \sqrt{\left(\frac{\omega}{c_R}\right)^2 - (K_y\omega)^2} - \sqrt{\left(\frac{\omega}{c_P}\right)^2 - (K_y\omega)^2} \right) x_R - \omega\frac{b}{\Delta c_P} = 2\pi n, \quad \text{with } n \in \mathbb{N}, \tag{3.4}$$

where $x_R$ is the receiver location that for this specific case is $x_R = 22.8\,\text{m}$ and $\Delta c_P$ is the difference between the compression wave velocity in trench and soil. The compressional wave velocity is computed for the trench and soil: $c_{P,Trench} = 497.4\,\text{m}/s$ and $c_{P,Soil} = 154.3\,\text{m}/s$.

The horizontal insertion loss plot $\text{IL}_x(x = 22.8, K_y, z = 0, \omega)$ is qualitatively similar to the vertical one. The colour map in Fig. 3.8 highlights how the presented concepts apply to the horizontal insertion loss plot, too. The biggest differences between $\text{IL}_x$ and $\text{IL}_z$ can be observed in the bottom part, where the insertion loss is dominated by the wavefront shift phenomenon.

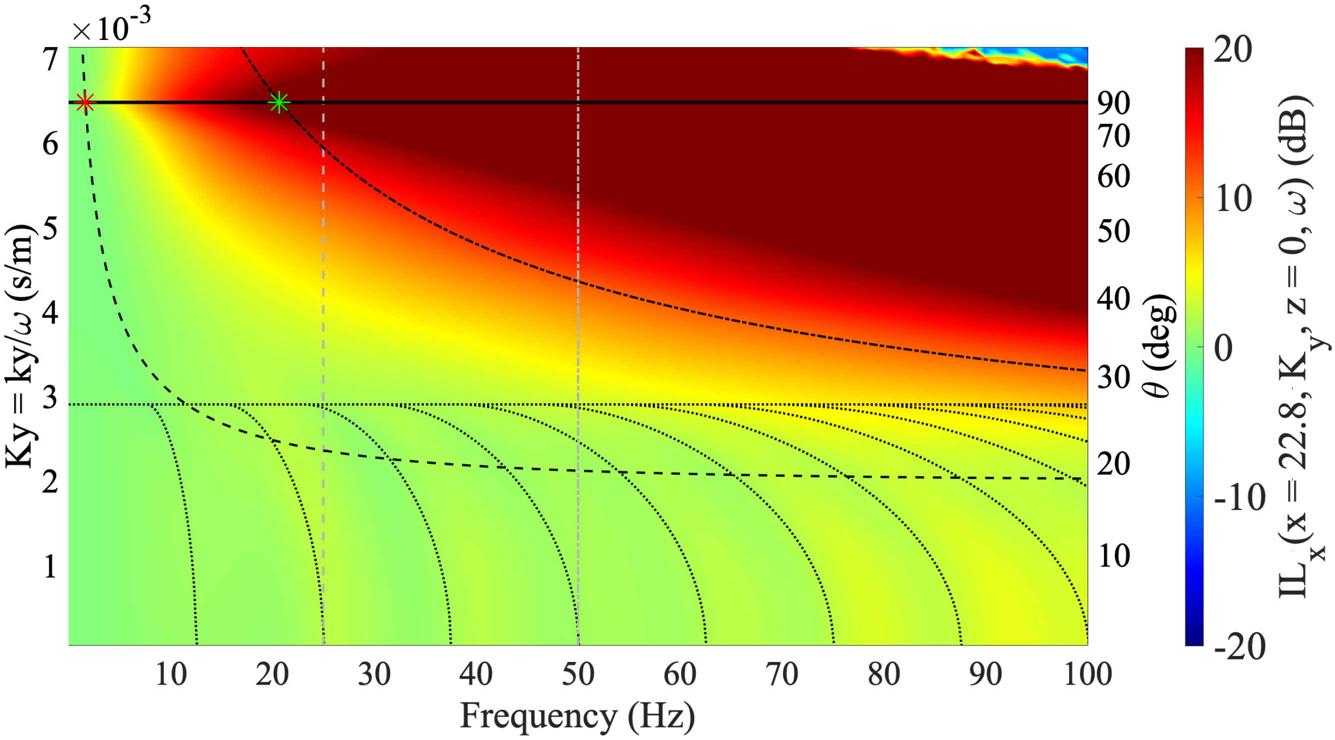

Figure 3.8: Horizontal insertion loss $\text{IL}_x(x = 22.8, K_y, z = 0, \omega)$ for the reference stiff in-filled trench embedded in homogeneous half-space. Refer to Fig. 3.5 for the description of the superimposed curves.

## Analysis in the space-frequency domain

The soil response is obtained in the space-frequency domain by numerically evaluating the inverse Fourier transform, which allows moving from the longitudinal wavenumber $k_y$ to the spatial coordinate $y$.

The left plot of Fig. 3.9 shows the real part of the vertical displacement component $\text{Re}(u_z)$ in the half-space without any type of vibration countermeasure, whereas in the right one the stiff trench is taken into account. The unit harmonic vertical point load excites the medium with $\Omega = 2\pi \times 25\,\text{Hz}$ at the origin of the coordinate system.

The horizontal components are not presented for brevity. The plots are collected in Appendix C. Due to symmetry, they display the wave field that is rotated 90 deg one with respect to the other. Independently from the frequency of excitation, along the axes the following holds $u_x(x, y = 0, z, \omega) = 0$ and $u_y(x = 0, y, z, \omega) = 0$. These aspects should be carefully contemplated if a field measurement setup is designed for a non-moving load.

Cylindrical wavefronts are exhibited at the surface level in Fig. 3.9a. Moving away from the source, the vibration amplitude decreases because of geometric attenuation and material damping. The contribution of body waves is more evident close to the origin, while the Rayleigh waves tend to travel farther and to remain closely attached to the free surface.

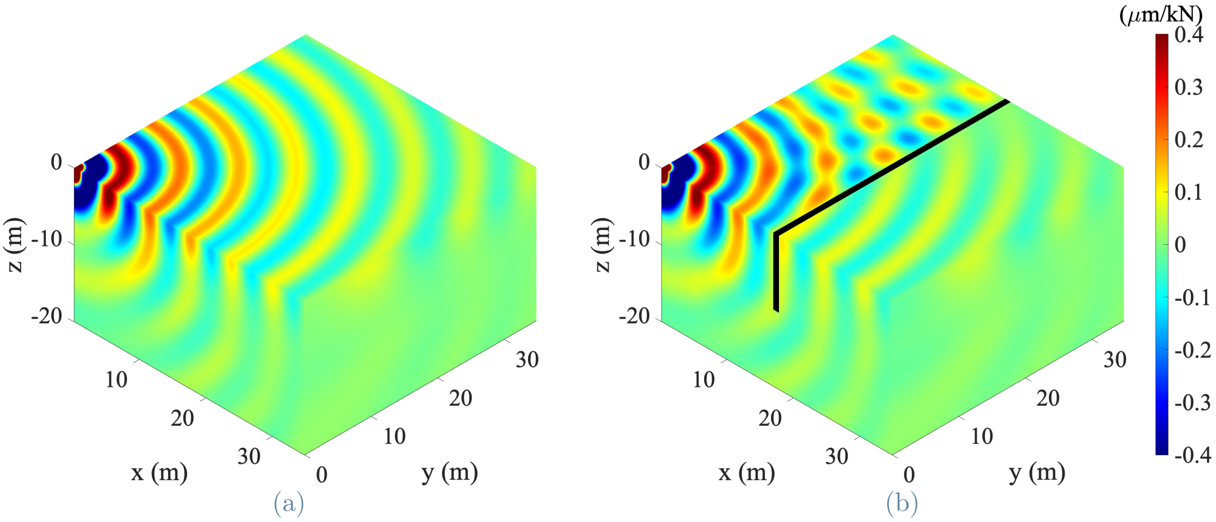

(a) (b)

Figure 3.9: Real part of the vertical displacement component $\mathrm{Re}(u_z(x, y, z, \Omega = 2\pi \times 25\,\mathrm{Hz}))$ generated by unit harmonic vertical point load. Homogeneous soil (a) and with in-filled trench (b).

If the stiff trench is introduced into the soil, the wave propagation is altered. The resulting wave field is presented in Fig. 3.9b. In these box-type plots, the mitigation measure is depicted with a black band. The symmetrical feature does not appear anymore. The incoming waves are partly reflected by the mitigation measure, giving constructive and destructive interference at the source side ($0\,\mathrm{m} < y < 17.4\,\mathrm{m}$). This phenomenon is particularly evident in the vertical component, which experiences the largest vibration amplitudes.

To underline the effect of the stiff trench, the insertion loss is computed from the displacement terms. The horizontal component $y$ is disregarded because the very low amplitudes located immediately behind the trench lower the interest for this direction. The $\mathrm{IL}_x(x, y, z, \Omega = 2\pi \times 25\,\mathrm{Hz})$ is presented in the left panel of Fig. 3.10, while the $\mathrm{IL}_z(x, y, z, \Omega = 2\pi \times 25\,\mathrm{Hz})$ is allocated to the right one. Note that a wider domain is now analysed. The smaller portion considered in Fig. 3.9 is underlined here by a thin black line.

As observed in the previous section, a direct link between the longitudinal slowness $K_y$ and the position in space is expressed by $\theta$. The insertion loss in the space-wavenumber-frequency domain provides information on the mitigation measure performance at the receiver position in the $xz$-plane and along its projection in the $y$ direction. The $x$

and $z$ coordinates are imposed, while the result in the $y$ direction is recovered by the angle relation $\theta = \sin^{-1}(K_y/K_R)$. The receiver position coincides with the geophone I location, implying $x = 22.8\,\text{m}$ and $z = 0\,\text{m}$ (cf. Fig. 2.3). Fixing the excitation frequency $\Omega = 2\pi \times 25\,\text{Hz}$ and increasing the $K_y$ value along the grey dashed line in Fig. 3.5 is equivalent to proceeding along the corresponding line in Fig. 3.10b. The same can be stated for Fig. 3.8 and Fig. 3.10a, respectively. The null angle value coincides with the point that lies on the $x$-axis, while increasing $\theta$ generates the rotation in the anti-clockwise direction (positive based on the $z$-axis direction).

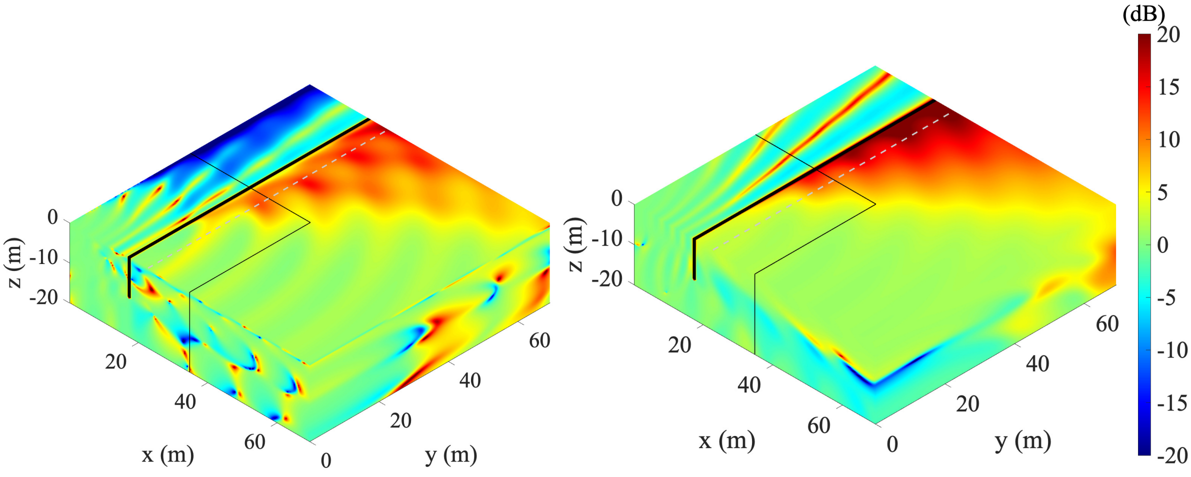

(a) (b)

Figure 3.10: Insertion loss in the space-frequency domain: $\text{IL}_x(x, y, z, \Omega = 2\pi \times 25\,\text{Hz})$ (a) $\text{IL}_z(x, y, z, \Omega = 2\pi \times 25\,\text{Hz})$ (b).

For small $\theta$ values, a poor shielding action of the stiff trench is generally presented for both the components in Fig. 3.10. The bending modes are not activated and the trench seems inefficient in mitigating vibration. The bending modes of the beam model are activated increasing the longitudinal slowness value along the dashed grey line in Fig. 3.5 and Fig. 3.8. They contribute to generating a greater insertion loss. This happens around the crossing points between the vertical line and the dispersion curves, which are analytically computed through Eq. (3.2). For this reference example, $\theta_{c,x} = 21.4\,\text{deg}$ and $\theta_{c,z} = 66.5\,\text{deg}$. For $x = 22.8\,\text{m}$, $\text{IL}_x$ reaches the 20 dB at a larger $\theta$ than $\text{IL}_z$. This appears clear from Fig. 3.10, but it can be observed by the plots in the wavenumber domain as well.

The insertion loss is similar behind the mitigation measure for the horizontal and vertical direction, as already observed in $K_y - f$ plots. This is not true for the zone in front of the trench for $0\,\text{m} < y < 17.4\,\text{m}$. At this side, the horizontal insertion loss appears negative close to the $y$-axis due to the reflection effect, while there is no vibration amplification for $\text{IL}_z$ there. In both directions, the constructive and destructive interference causes thin strips of high insertion loss (see Fig. 3.10). Some differences arise for $z < 0\,\text{m}$, too.

This analysis demonstrates an important consequence of the stiffness effect that is distinctly identified in the space domain. Behind the trench, a green cone where the countermeasure badly performs can be generated. The stiff trench solution reveals one of its weak points, being inefficient in this region. For certain parameters, a satisfactory mitigation is achieved even in that area thanks to the reflection effect, which is completely independent of $k_y$ [8].

For the chosen case, it seems that below a limit angle $\widetilde{\theta}$ the waves are transmitted through the trench almost undisturbed. If this threshold is exceeded, the incoming waves are redirected and they start to flow along the trench following the bending modes (i.e., the stiffness effect). This phenomenon causes nearly null IL inside the cone (green colour) and a good performance outside (red colour), as shown in Fig. 3.11.

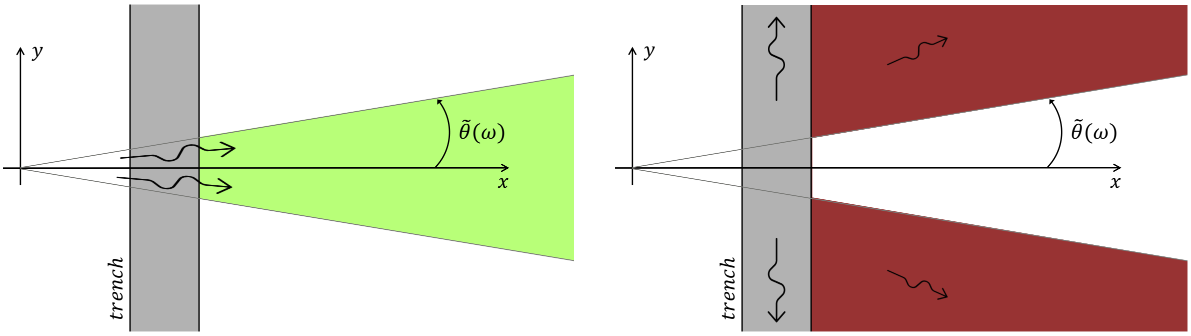

(a) IL $\simeq 0$ for $\theta(\omega) < \widetilde{\theta}(\omega)$ (green) (b) Large IL $> 0$ for $\theta(\omega) > \widetilde{\theta}(\omega)$ (red)

Figure 3.11: Wave redirection effect in the space domain, efficient (a) and inefficient (b) mitigation region. The reflected wave term is neglected.

The limit angle definition derives from the insertion loss value that is set to distinguish the two zones. The following relation holds: $\widetilde{\theta} \geq \theta(\omega_{c,x})$. It is possible to affirm that the stiffness effect leads to a wave redirection phenomenon in the three-dimensional space. Its nature - like the one of the stiffness effect - depends on the frequency of excitation. This aspect is further investigated in Section 3.2.4.

Recalling that the excitation induced by a passing train can be approximated by a series of dynamic axle loads, it is worth noting that the generated cone has significant practical relevance. Each axle point can develop the conical region where the stiff trench is almost ineffective. This reveals that the contribution to the vibration field of a large number of axle loads is significantly reduced if a receiver location closer to the track is considered

[9]. Moving away from the trench increases the possibility that the point is within various cones spawned by several axles. On the other hand, the geometric and material damping effects decrease the amplitude of the wave when the distance from the trench is increased. Moreover, the vibration in the near field is dominated by the closest axle loads, while all axle loads contribute almost equally to the response in the far field [10].

The above discussion combined with Fig. 3.5 proves that the stiff in-filled is typically unable to attenuate vibration when $\Omega < \omega_{c,x}$. In this case, no bending mode can be activated and the insertion loss parameter is almost null for $0 < K_y < K_R$. This is equivalent to a full cone, which extends from 0 deg to 90 deg. There, the only beneficial contribution comes from the reflection effect. In Appendix C, this possibility is exemplified through a simulation with $\Omega = 2\pi \times 1\,\text{Hz} < \omega_{c,x}$.

### 3.2.4. Influence of the excitation frequency

This section investigates how the stiff trench behaviour changes if the excitation frequency of the harmonic force is modified. The previous analysed value of omega $\Omega_1 = 2\pi \times 25\,\text{Hz}$ is doubled, exciting the medium at $\Omega_2 = 2\pi \times 50\,\text{Hz}$.

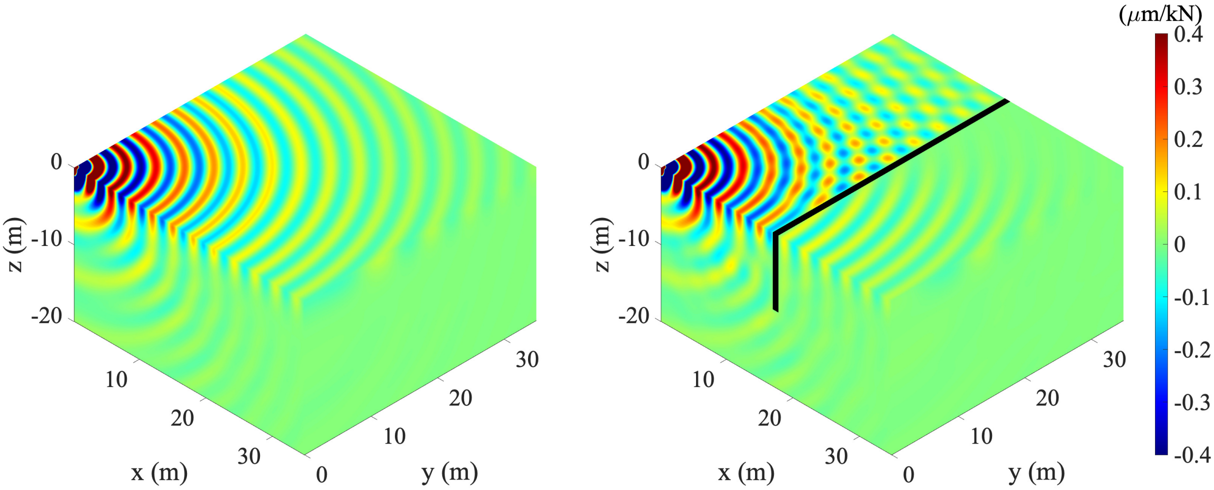

(a) (b)

Figure 3.12: Real part of the vertical displacement component $\mathrm{Re}(u_z(x, y, z, \Omega = 2\pi \times 50\,\text{Hz}))$ generated by unit harmonic vertical point load. Homogeneous soil (a) and with in-filled trench (b).

From the displacement point of view, the influence of the excitation frequency can be understood through the well-known relation $\omega = k\,c$. Due to the non-dispersive nature of the homogeneous soil, the velocity of the waves is constant and frequency independent. An increase of the angular frequency $\omega$ implies a linear increase of the wavenumber $k$.

This can be translated into a reduction of the wavelength $\lambda$.

The consequences in the space domain are displayed in Fig. 3.12, where the increased frequency makes the resulting circular wavefronts smaller than the ones in Fig. 3.9. This effect results in less penetration of the waves into the medium. The introduction of the mitigation measure into the ground gives a more evident constructive and destructive interference compared to Fig. 3.9b. The same strategy applies to the horizontal components of the displacement that are presented in Appendix C.

As suggested by Fig. 3.5 and Fig. 3.6, the excitation frequency represents an important parameter for the stiff in-filled trench performance. Choosing $\Omega > \omega_{c,x}$, a better mitigation is expected when the excitation frequency increases. This is deduced from the wider range of longitudinal slowness values characterized by high insertion loss (red colour). This occurs because the $K_b < K_y < K_R$ interval enlarges, given $K_b \sim 1/\sqrt{\omega}$. Fig. 3.5 and Fig. 3.8 show this trend for the two values of frequency through the two vertical grey lines at $\Omega_1$ and $\Omega_2$.

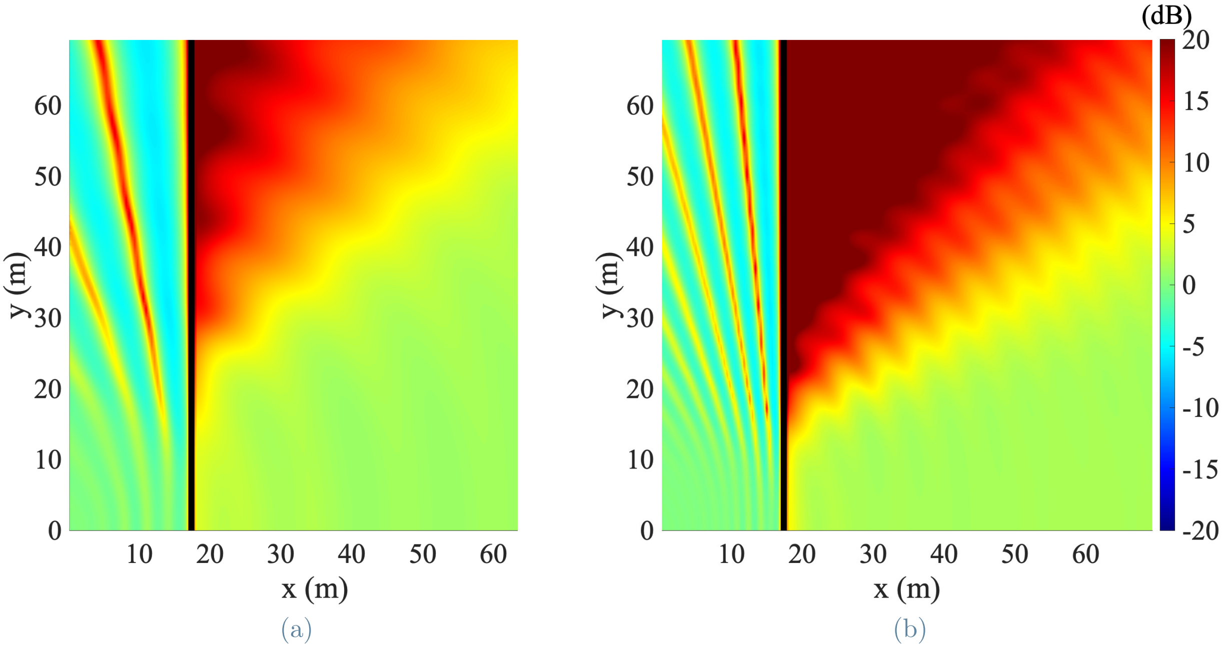

(a) (b)

Figure 3.13: Vertical insertion loss in the space-frequency domain: $\text{IL}_z(x, y, z = 0, \Omega = 2\pi \times 25\,\text{Hz})$ (a) $\text{IL}_z(x, y, z = 0, \Omega = 2\pi \times 50\,\text{Hz})$ (b).

Moving to the space-frequency domain, a narrower angle - characterized by low insertion loss - is expected behind the trench. Indeed, for $\Omega_2$ the high insertion loss range starts at smaller $\theta$ values than $\Omega_1$. The vertical insertion loss is depicted for the soil surface in Fig. 3.13, where the first plot (Fig. 3.13a) presents the results for $\Omega_1 = 2\pi \times 25\,\text{Hz}$ and the second one (Fig. 3.13b) for $\Omega_2 = 2\pi \times 50\,\text{Hz}$. From their comparison, the better performance of the stiff trench is obvious at the larger frequency. The shielded region broadens and the low insertion loss cone gets narrower. This is beneficial for the situation of the train passage excitation, too. This figure directly exhibits the difficulty of shielding waves at lower frequencies. The box-type figures are proposed in Appendix C.

### 3.2.5. Influence of the Young's modulus for the trench and soil material

The main mitigation mechanism of the stiff in-filled countermeasure is based on the stiffness contrast between its material and the surrounding medium. This section presents the consequences related to a soil softening and to a stiffening of the trench material.

For one case, the reference trench of the previous section is embedded in a homogeneous half-space characterized by a softer ground, which has the same properties as the top softest layer of the Tricht site (cf. Table 2.1). For the other analysis that examines the stiffer trench effect, the reference soil is kept unvaried (same properties as the last layer of Tricht ground) and the Young's modulus of the trench material is set ten times larger than the reference one (i.e., $E_{Trench} = 10\,000\,\mathrm{MPa}$).

The vertical insertion loss is displayed in Fig. 3.14 in the space-wavenumber-frequency domain. Fig. 3.14a refers to the softer soil case, while Fig. 3.14b show the outcome of the stiffer trench study. The results show wider areas characterized by large insertion loss ($K_b < K_y < K_R$). The increase in the stiffness difference between the two media provides a superior attenuation performance of the stiff trench.

In Fig. 3.14a the horizontal line $K_R = 1/c_R$ moves up because the softer soil gives a smaller Rayleigh wave velocity, as listed in Table 2.1. This shift beneficially lowers the critical frequencies, which become $\omega_{c,x} = 2\pi \times 0.2\,\mathrm{Hz}$ and $\omega_{c,z} = 2\pi \times 2.3\,\mathrm{Hz}$ from Eq. (3.2). Furthermore, the number of dotted curves that express the phase shift of compressional waves increases in the frequency range $0-100\,\mathrm{Hz}$ because the value of the wave velocities in soil changes in Eq. (3.4). Their contribution is strengthened in this case, which experiences high vertical insertion loss also for the smallest values of longitudinal slowness $K_y$. The curves representing the bending modes are the same as the reference case, because the trench is not subjected to any variation of the material properties.

A similar outcome is displayed in Fig. 3.14b, where the soil is kept unvaried and the in-filled trench is stiffer than the reference one. This time the $K_R$ line does not move and the Timoshenko's beam dispersion curves lower. This shift has the same effect as the previous one, leading to smaller critical frequencies $\omega_{c,x} = 2\pi \times 0.5\,\mathrm{Hz}$ and $\omega_{c,z} = 2\pi \times 6.2\,\mathrm{Hz}$. The effect of the wavefront phase shift on the bottom part of the figures becomes again more pronounced.

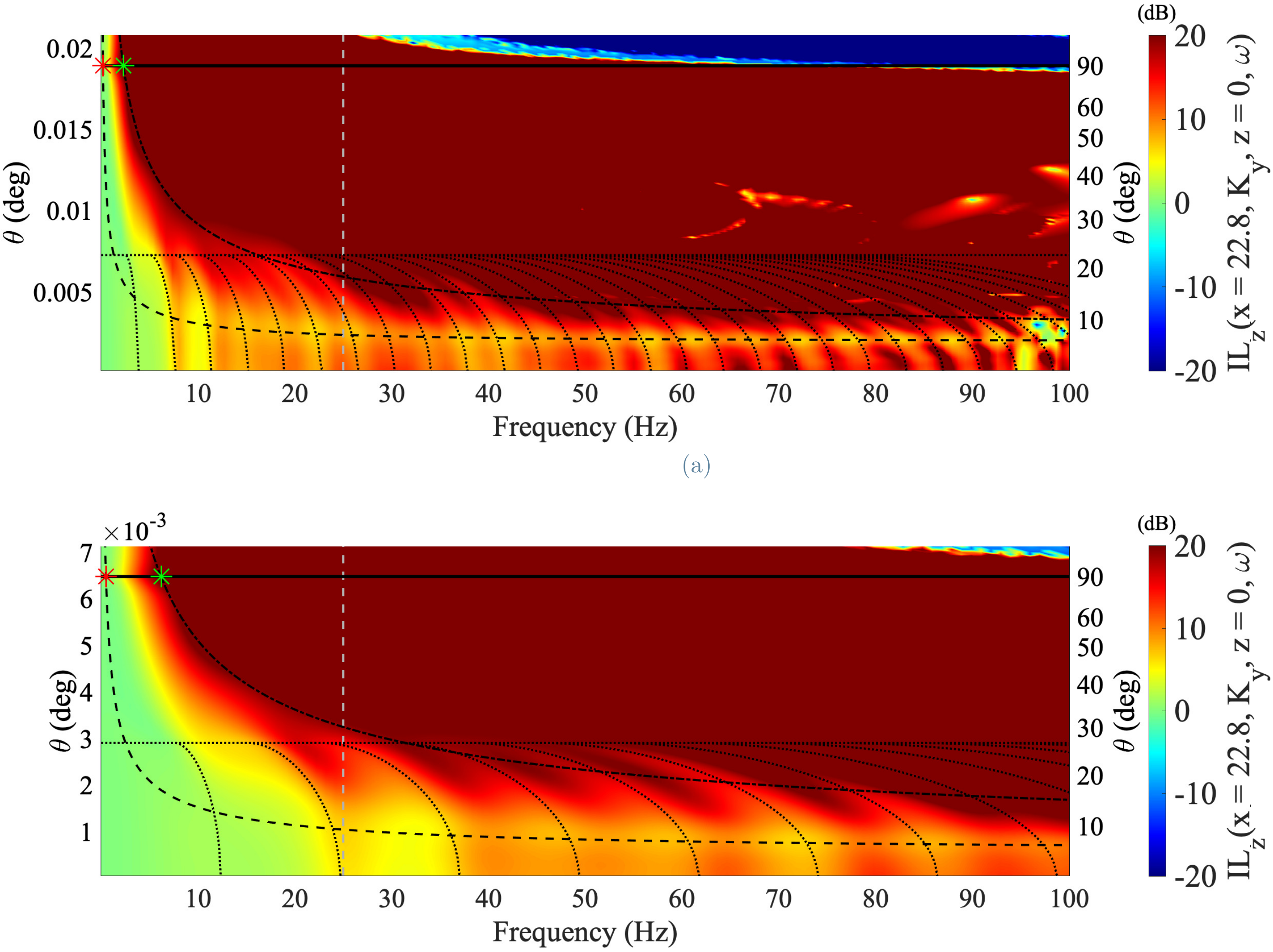

(a)

(b)

Figure 3.14: Vertical insertion loss $\mathrm{IL}_z(x = 22.8, K_y, z = 0, \omega)$ for softer soil and reference trench (a) and for reference soil and stiffer trench (b). Refer to Fig. 3.5 for the description of the superimposed curves.

The positive $\mathrm{IL}_z$ in correspondence to low slowness values suggests that the low insertion loss area behind the stiff trench is limited to small angles. It seems even to disappear for certain excitation frequencies. The vertical insertion loss in the space-frequency domain is presented for $\Omega = 2\pi \times 25\,\mathrm{Hz}$ in Fig. 3.15. At this excitation frequency, the light green cone ($\mathrm{IL}_z \simeq 0$) behind the stiff trench disappears and the zone shows a positive mitigation effect ($\mathrm{IL}_z > 5\,\mathrm{dB}$). An orange one remains visible, showing how the trench is still less prone to mitigate vibration there with respect to the other surface parts. Outside this region, the 20 dB threshold is reached and the large insertion loss is experienced not only at the surface level but also for the increasing soil depth ($z < 0\,\mathrm{m}$).

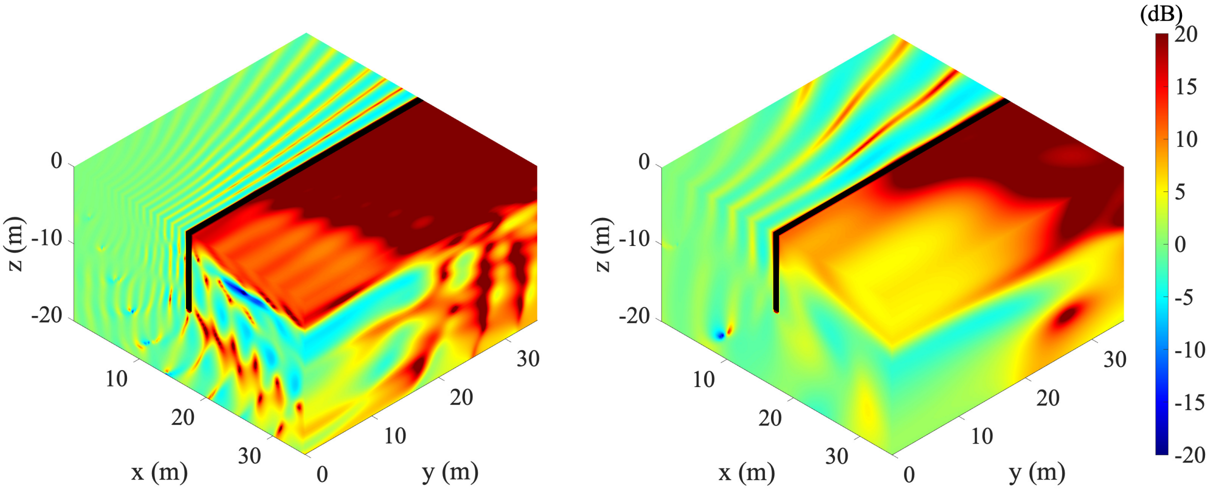

(a)

(b)

Figure 3.15: Vertical insertion loss $\mathrm{IL}_z(x, y, z, \Omega = 2\pi \times 25\,\mathrm{Hz})$ for softer soil and reference trench (a) and for reference soil and stiffer trench (b).

For the softer soil and reference trench case - Fig. 3.15a - the constructive and destructive interference phenomenon strongly arises at the surface on the source side. This pattern is similar to the one shown in Fig. 3.13b, where the excitation frequency is double with respect to the one imposed here. It happens because softening the soil and increasing the excitation frequency have the same consequence of reducing the wavelength $\lambda$. Indeed, if the excitation frequency is increased and the soil is equal to the reference one, the wave propagation velocity is kept constant and $\lambda$ decreases. On the other hand, the softer soil leads to a lower velocity that introduces the wavelength decrease, if the excitation frequency is fixed.

The horizontal insertion loss $\mathrm{IL}_x$ is not presented here because it qualitatively reminds the already discussed plots. Its representation in the space domain is available in Appendix C with the three-dimensional version of the plots in Fig. 3.14 and the displacement fields.

To conclude this section, the increase in stiffness difference between trench and soil leads to improved performance. The results show a better mitigation that appears clear in both the considered domains and analysed cases. The conical region characterized by nearly null insertion loss is replaced by $\mathrm{IL}_z > 5\,\mathrm{dB}$ values.

## 3.3. Simulation and assessment of vibration mitigation effect

The analysis approach of Section 3.2 is applied to the case of a stiff in-filled trench embedded in layered half-space. For a dispersive medium, the feasibility of the previously presented mitigation mechanisms is verified. The numerical model of the stiff trench embedded in the Tricht site is presented. The numerical and in-situ test results are also compared.

### 3.3.1. Case study: stiff trench embedded in a layered half-space

The stiff in-filled trench installed in the Tricht site is modelled with the 2.5D procedure in FEMIX. The layered soil presents four layers characterized by the properties listed in Table 2.1. Table 2.2 summarises the geometry and the material properties of the mitigation measure. The trench model and the excitation type are identical to the reference ones already set in Section 3.2. The receivers are placed at the same positions as the measurement instruments during the dropping load test because the final aim of this chapter is the comparison of the numerical results with the ones computed with the geophones data. The dropping load test and measurement setup data are available in Chapter 2. The cross section in the $xz$-plane - assumed invariant along the $y$ direction - is outlined in Fig. 3.16.

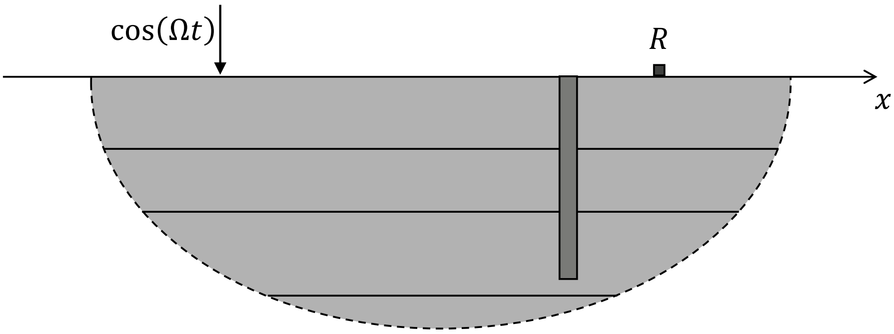

Figure 3.16: Lateral view of the wave propagation problem in the layered half-space, the grey cube with the $R$ letter indicates the first receiver location.

In a layered half-space the phase velocity depends on the frequency due to the dispersive properties of the medium, as already highlighted in Chapter 1. Due to the variation of the soil properties with depth, the dispersion curve of the Rayleigh wave is not anymore a horizontal line in the slowness-frequency plot. Indeed, infinitely many modes exist.

The propagation of Rayleigh waves becomes dispersive and the procedure to compute the dispersion curves is described in detail in [72]. Note that the maximum phase velocity coincides with the shear wave speed of the lower half-space that is the stiffest layer, while the minimum one corresponds to the Rayleigh wave speed of the top layer that is the softest one [17]. The dispersive medium implies that the critical frequency $\omega_c$ must be determined by an iterative solving procedure because the Rayleigh wave velocity is frequency dependent in Eq. (3.2). For this work, this step is implemented in MATLAB.

### 3.3.2. Simulation results

Following the same approach adopted for the homogeneous soil case, the vertical insertion loss $\mathrm{IL}_z$ is computed at the first geophone position. The result is plotted in the space-wavenumber-frequency domain for the $0-30\,\mathrm{Hz}$ frequency range in Fig. 3.17. Attention is paid to the frequency values affected by the cargo train excitation.

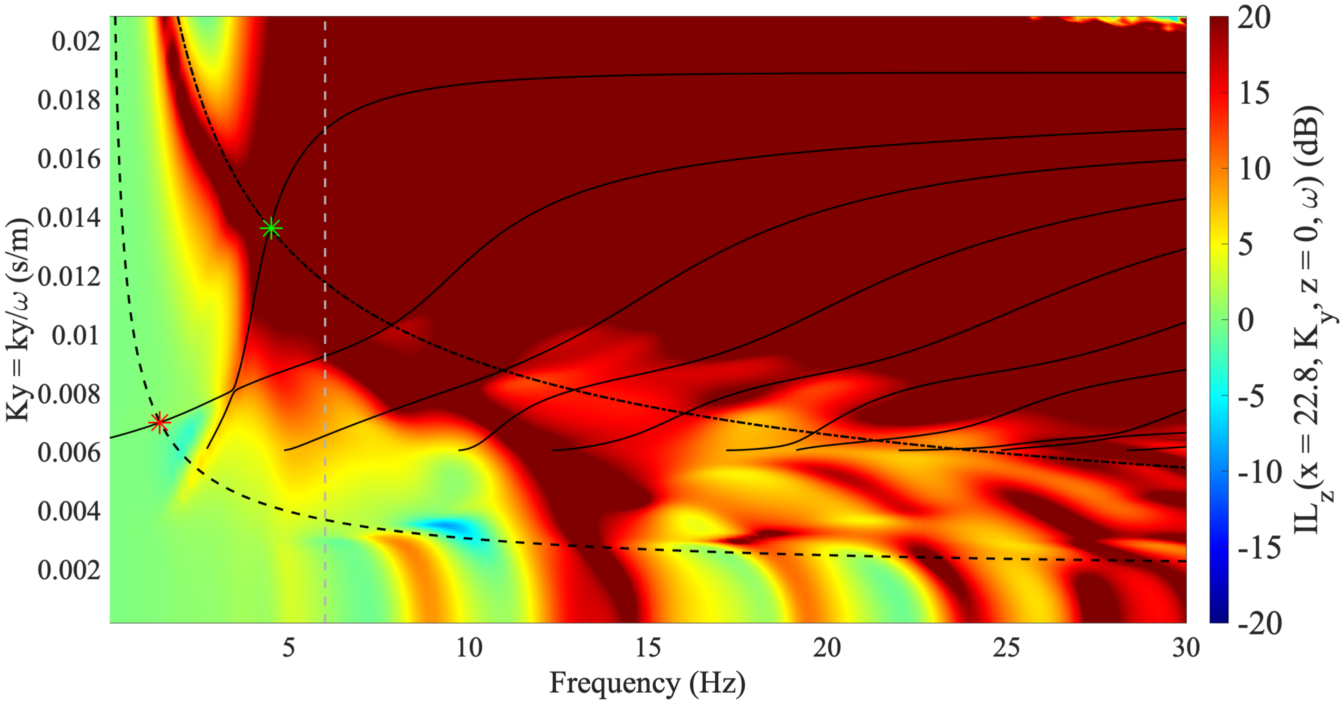

Figure 3.17: Vertical insertion loss $\mathrm{IL}_z(x = 22.8, K_y, z = 0, \omega)$ for the reference stiff in-filled trench embedded in layered half-space. Superimposed are the dispersion curve for Timoshenko's beam bending mode around the $x$-axis (black dashed line) and $z$-axis (black dashed-dotted line), the dispersion curves Rayleigh wave (solid line). The stars represent the critical frequency for bending mode around the $x$-axis (red) and $z$-axis (green). $f = 6\,\mathrm{Hz}$ (grey dashed line).

Note that above the top Rayleigh wave dispersion curve the wavenumber $k_x$ becomes imaginary [9]. That region loses practical relevance because it describes evanescent waves in the $x$ direction, as already stated in Section 3.2.3. Moreover, the dotted curves that express the phase shift of the wavefronts are not presented because an adequate match between the insertion loss pattern and those curves obtained with Eq. (3.4) is not observed.

Fig. 3.17 reveals that the physical mitigation mechanism described in the previous sections is also valid for the layered soil case. Indeed, the stiffness effect plays an important role in vibration attenuation. The highest values of insertion loss are reached when both the bending modes of the trench are activated. Especially below 15 Hz, the activation of the bending mode around the $z$-axis seems crucial to reaching large values of insertion loss. The first critical frequency related to the bending mode around the $x$-axis (red star) does not well indicate where the stiff trench starts to prevent the transmission of waves. The other critical frequency - $\omega_{c,z} = 2\pi \times 4.5\,\mathrm{Hz}$ - appears more reliable from this point of view.

An interference pattern is observed at the highest frequencies and smallest slowness values in Fig. 3.17. This pattern of the results is more complex than the homogeneous half-space soil case due to the multiple reflections and refractions among the layer interfaces [9]. As already mentioned, neither the trends described by Eq. (3.4) seem able to describe the complex nature of this phenomenon. Due to this effect, some regions show negative insertion loss that expresses the amplification of vibration amplitude. For the horizontal insertion loss, a wider region is characterized by negative values (below the 4 Hz). The trench presence would generate a vibration amplification at that point if the soil is excited with that frequency value. See Appendix C for the $\mathrm{IL}_x$ plot.

Applying the inverse Fourier transform, the insertion loss is computed in the space-frequency for $\Omega = 2\pi \times 6\,\mathrm{Hz}$, which is the dominant frequency excited by the cargo train passages. The related real part of the vertical displacement component (without and with the trench) is shown with the vertical insertion loss in Fig. 3.18. The different layers are graphically separated by thin horizontal black lines. The corresponding plot for the component in the horizontal directions and the three-dimensional version of Fig. 3.17 are depicted in Appendix C.

The wave field generated by the unit vertical point load is concentrated in the first layer of soil, as shown in Fig. 3.18. This observation gives the opportunity to underline an important concept: the insertion loss parameter effectively translates the performance of the mitigation measure in the spatial zones affected by considerable displacement amplitude. It is not interesting to analyse the insertion loss evolution in the areas where the displacement magnitude is small before and after the vibration countermeasure installation. Neglecting this consideration could lead to a wrong assessment and misleading conclusions.

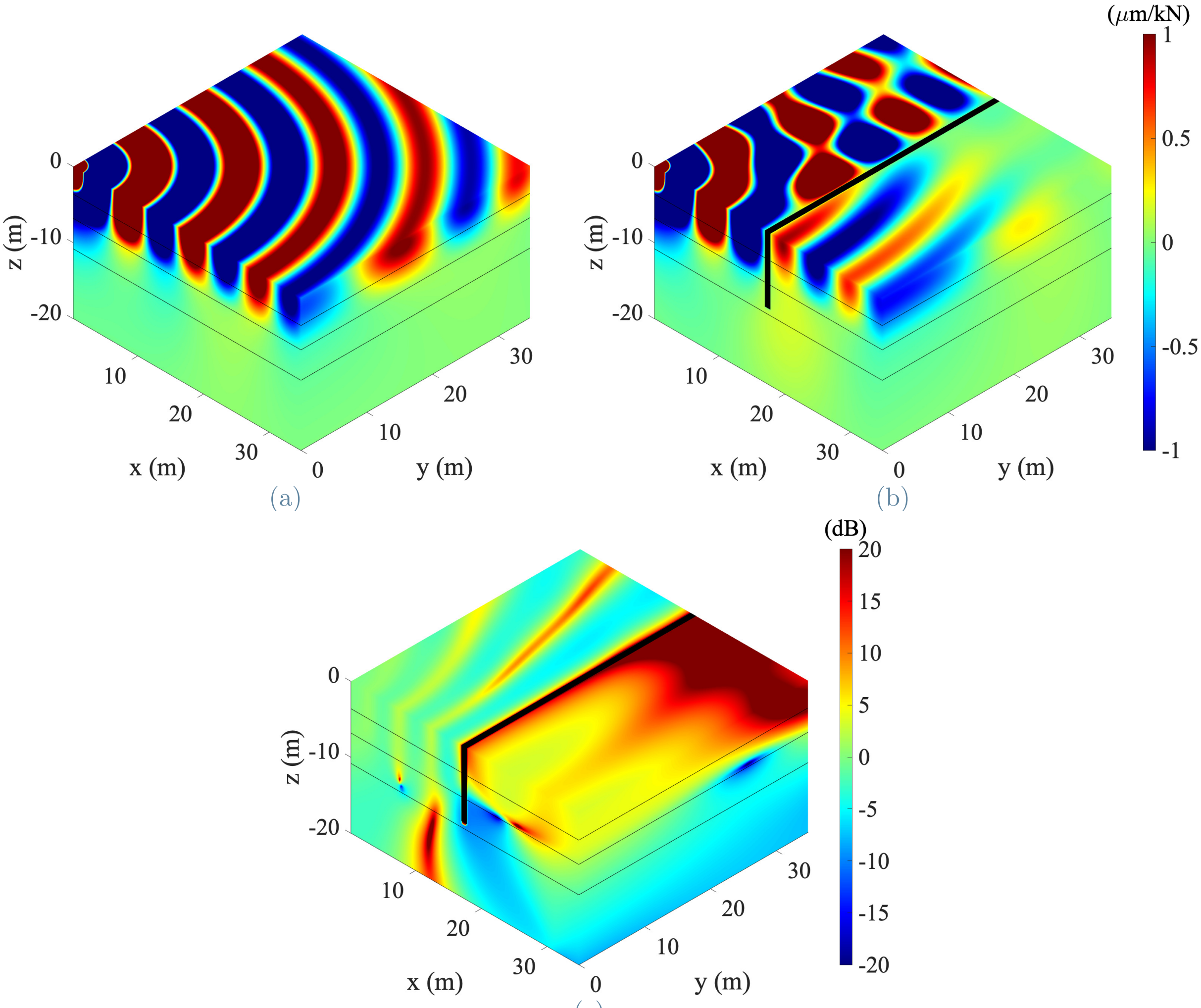

(a) (b)

(c)

Figure 3.18: Real part of the vertical displacement component for the layered half-space (a), stiff in-filled trench (b) and vertical insertion loss (c) in the space domain for $\Omega = 2\pi \times 6\,\mathrm{Hz}$.

The cone effect (see Section 3.2.3) appears also in the layered soil case for $\Omega = 2\pi \times 6\,\mathrm{Hz}$ in Fig. 3.18c, even though inside this cone the insertion loss is not as small as in the case of reference homogeneous soil. This feature proves that placing devices outside the conical region is advantageous during a measurement campaign with a non-moving load. At locations where the insertion loss is higher, assessing the mitigation measure efficiency is simpler and more effective. If the devices are placed both inside and outside the cone the redirection effect can be experimentally presented. This shows that arranging devices only in line with the loading point is not a good choice. The $y$ component of the vibration is also theoretically null along that line.

The effect of the stiff trench and its shielding ability can be evaluated through the Power Spectral Density, as already demonstrated in Section 2.3 with the in-situ tests data. The PSD is computed numerically for the five geophones positions with the outputs of the simulations. The averaging step of Eq. (2.2) cannot be accomplished because there is no variability related to the results. Fig. 3.19 shows the outcomes for the first three measurement instruments locations for the $x$ and $z$ components.

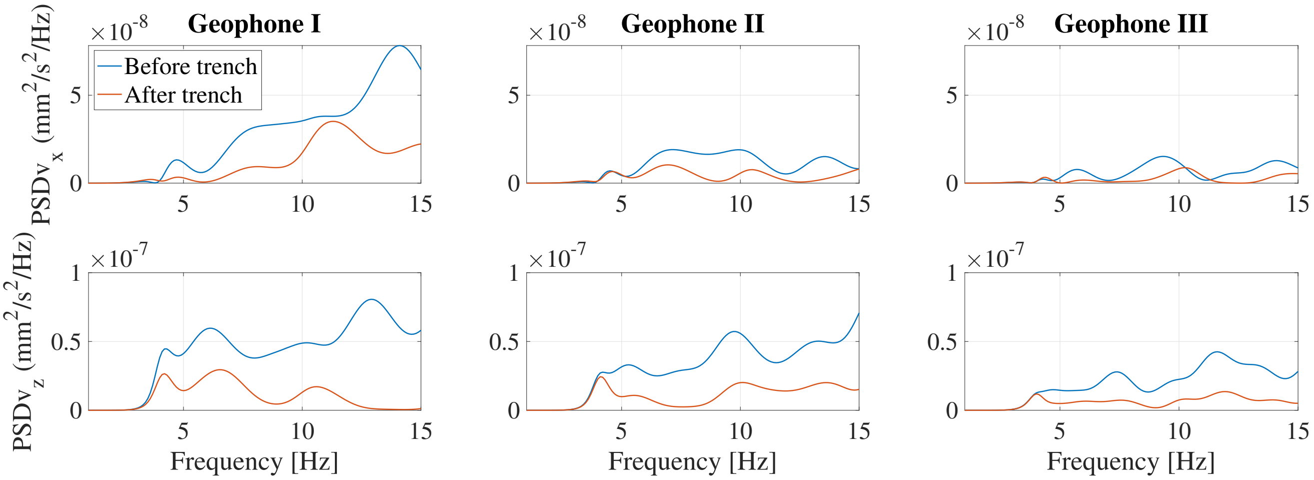

Figure 3.19: PSD obtained from numerical simulations for the first three geophones locations associated with the vertical harmonic load simulation in layered half-space (blue) and with stiff in-filled trench (orange).

The vertical component of the vibration shows larger energy content than the horizontal direction. Note the different scales on the vertical axis. The stiff in-filled trench is undoubtedly efficient in attenuating the vibration for the considered frequency range ($0-15$ Hz). The power distribution with the trench is always smaller than the one without the trench and very limited exceptions occur. Nevertheless, the two lines appear almost overlapped for the very first frequencies ($f < 4$ Hz). This range is the one characterized by the lowest power content, too. Especially for the component in the vertical direction, this phenomenon has been already observed in Fig. 2.8 with the results of the dropping load test. There the activation threshold occurs slightly above 5 Hz. These values correspond to the critical frequency $\omega_{c,z} = 2\pi \times 4.5$ Hz, which is underlined by the green star in Fig. 3.17. Moving away from the source the power content of the perturbation decreases - as expected - due to geometric and material damping.

Concerning the field measurement data, the numerical results generate smoother trends without narrow peaks. The beneficial contribution of the stiff trench is shown also for the horizontal direction. The numerical results do not show contradictory trends, differently from the geophones data. An evident power content reduction for the component in the $x$ direction is shown in Fig. 3.19, contrary to Fig. 2.8. This discrepancy suggests to carefully comment the experimental results in that direction. The experienced energy content could be given by external factors that are not related to the dropping load test and trench performance.

The outcomes at the last two device locations are in agreement with the formerly discussed points. For brevity, they are given in Appendix C.

### 3.3.3. Mitigation effect assessment and comparison with in-situ test result

The efficiency of the stiff trench is numerically assessed through the computation of $\mathrm{IL}_x$ and $\mathrm{IL}_z$ with Eq. (2.4). The vertical point harmonic load scenario is adopted for the model. Both numerical and dropping load test results are expressed in one-third-octave bands in Fig. 3.20. The first row refers to the insertion loss evolution in the horizontal direction $x$, while the second one presents the component along the $z$-axis. The results for the other two devices locations are available in Appendix C.

The numerical insertion loss trend resembles the one in the PSD results of Fig. 3.19. For the first two one-third-octave bands at lower frequencies, the smallest values are experienced. For the horizontal direction even negative values are reached. This aspect is originated from the inefficient performance of the mitigation measure in that frequency range, as seen in Fig. 3.19. Above 5 Hz, the insertion loss presents only positive values that are translated into an effective mitigation effect of the stiff trench. Generally, the curves grow until a local maximum with an increasing tendency. After that, a decrease is typically observed.

Comparing the numerical and experimental results, the insertion loss for the two components $x$ and $z$ is commented separately. Concerning the horizontal direction, the conflicting trends of the experimental results do not show a satisfactory agreement with the numerical ones. This difference is evident from the PSD plots, too. A general beneficial effect is shown by the numerical data, whereas contradictory information arises from the experimental outcomes as commented in Section 2.4.2. A better matching occurs for the insertion loss in the vertical direction, at least from the overall shape point of view. The curves computed with numerical and experimental results show increasing trends that generally reach the local maxima at close one-third-octave band values. The same comments can be applied to the plots of the other two receiver locations.

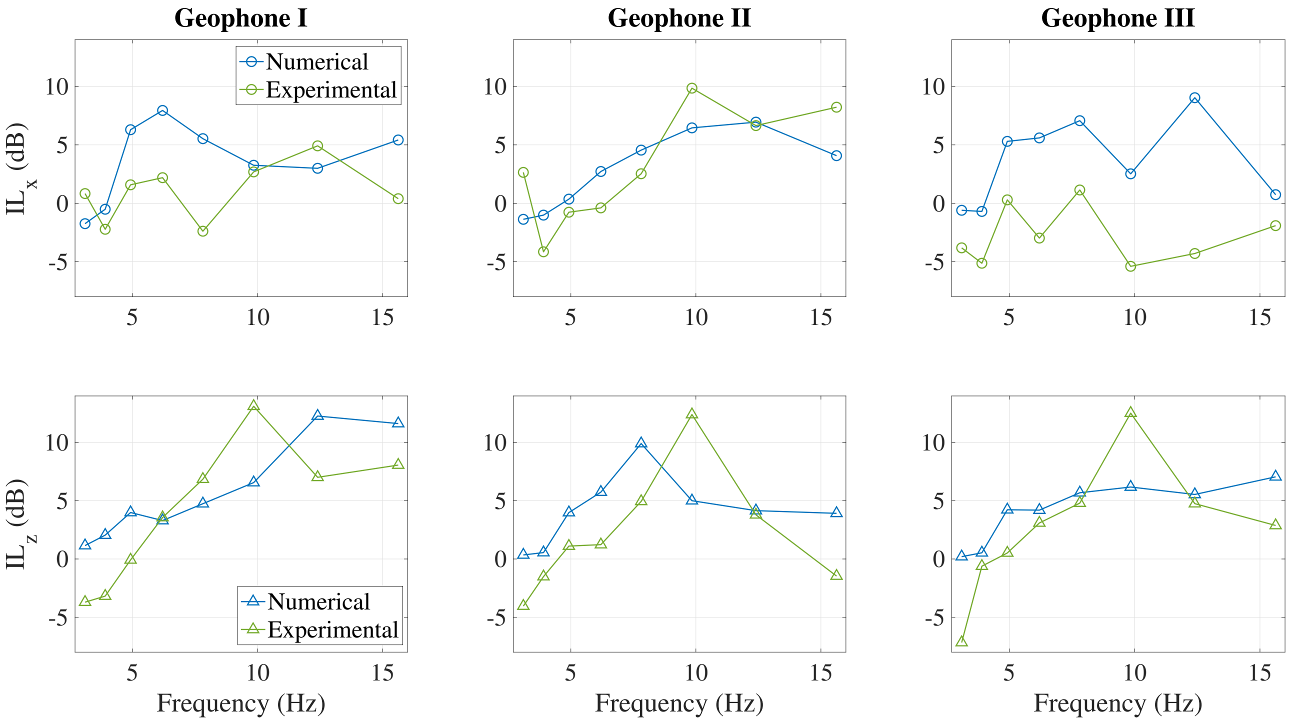

Figure 3.20: Comparison numerical (blue) and experimental (green) insertion loss for the first three geophones locations in $x$ (circle) and $z$ (triangle) direction.

Overall, the comparison of the experimental assessment with the numerical one is not satisfactory, especially for the $x$ direction. Although the numerical outcomes are coherent with the theoretical stiff trench performance and behaviour, the experimental ones generally do not show a good match. As already stressed, this kind of field measurement campaign is affected by a certain uncertainty produced by several uncontrolled and unknown variables. Furthermore, the numerical simulation does not perfectly model the real test conditions, for example the track and the asphalt layers are disregarded. An additional potential cause of the discrepancy between the predictions and the measurements might be a non-isotropic soil behaviour or a local alteration of the horizontally layered medium profile [20]. The induced wave field could also be altered by the energy scattering originated by local heterogeneities, such as embedded stone or piping that are commonly found in populated areas.

### 3.3.4. Summary

The layered half-space model is presented in this chapter. The validity of the mitigation mechanisms is evaluated in the dispersive medium and the numerical trench performance is assessed. The comparison with the dropping load test results also occurs.

The insertion loss plot in Fig. 3.17 proves the more complex physical interpretation of the trench behaviour in a layered half-space. The wave reflection among the different ground layers generates a complex pattern at small slowness values. Infinitely many Rayleigh wave modes appear, too. The activation of the beam model bending mode around the $z$-axis results more effective to achieve the largest insertion loss values. The corresponding critical frequency is a good approximation for the trench effectiveness starting point. Moving to the space-frequency domain, the wave propagation and insertion loss seem similar to the ones of the homogeneous half-space case. The wave energy content remains limited to the first and softest soil layer and the conical region behind the countermeasure is still present but with insertion loss values larger than one. These aspects confirm that the stiffness effect and the related wave redirection one still represent the key mitigation mechanisms to explain and evaluate the stiff trench performance in a layered soil.

The stiff trench performance is assessed through the insertion loss parameter, which is computed at different distances from the source. An effective vibration mitigation is experienced, especially for frequencies above 5 Hz. However, the comparison of the numerical and field measurement results does not produce a satisfactory outcome (see Fig. 3.20). Not a good agreement is achieved by the horizontal insertion loss $\mathrm{IL}_x$ at all. More similar trends are experienced with the comparison of the vertical insertion loss $\mathrm{IL}_z$. This discrepancy could be generated by relevant differences between the considered model and the in-situ test. Furthermore, placing the geophones inside the conical region behind the trench does not support the detection of its mitigation effect. The adopted measurement setup with all the devices aligned with the load point is not recommended for measurement campaigns with a non-moving load. Other non-aligned devices are necessary to record the soil response outside the conical region, which is affected by a less evident vibration attenuation.

# Part B

# Assessment of a metawedge: a railway application

# 4 | Mitigation mechanism, model validation and simulation

*The metawedge is introduced as a mitigation measure for surface induced ground vibration. In Section 4.1, its effect based on metamaterial and resonant unit cells is explained and the key wave-mode conversion mechanism is discussed. Thanks to this mitigation mechanism, the vibration countermeasure can convert the incoming Rayleigh waves into body ones, redirecting the energy content deep into the ground. The unit cell of the metawedge and the related theoretical concepts are presented in Section 4.2. In Section 4.3, the model and the solution approach are validated through a literature case. Once correct implementation is demonstrated, the development of a metawedge for the railway application is proposed in Section 4.4. For this system, the influence of the material properties and resonator dimensions on its dispersion properties and attenuation performance is also investigated.*

## 4.1. Wave-mode conversion mechanism

In the past two decades, metamaterials in elastic media have become an active research field for the study of wave propagation, solving complex vibration related engineering problems [38]. The application of metamaterials allows guiding and controlling the wave propagation direction through the wave-mode conversion mechanism. This concept - derived from photonic and phononic crystals - leads to new possibilities for developing innovative mitigation measures to attenuate the vibration level generated by the surface waves in the far-field [31].

A metamaterial is constituted by a periodic arrangement of an infinite number of elementary units with a sub-wavelength spacing [30]. This elementary unit is commonly called unit cell. A typical example is proposed in Fig. 4.1a, where the unit cell consists of a rectangular cross section resonator partially embedded in a homogeneous medium. In other words, the resonator is defined as an inclusion of another material in the main homogeneous half-space. The unit cells, with the possibility of different design criteria, are intended to collectively induce non-conventional dispersion properties to the system. For a non-dispersive homogeneous half-space without any resonators, the dispersion curve for the surface wave is depicted in Fig. 4.1b. The slope of the straight line depends on the material properties through the Rayleigh wave velocity $c_R$. As shown in Fig. 4.1b, the non-dispersive nature of the system guarantees the propagation of surface waves for any excitation frequency. Introducing the infinite periodic array of resonators, the dispersion curves displayed in Fig. 4.1c are obtained. The non-conventional dispersion properties are expressed by the presence of the two horizontal grey bands, which indicate band gaps (BG) of the system in Fig. 4.1c. In these frequency ranges, surface wave propagation is not possible; the wavenumbers are imaginary-valued making the waves evanescent [33]. Indeed, the excitation of the system for a frequency inside a band gap does not produce any propagating surface wave, as shown by the absence of corresponding real wavenumbers. Each band gap is opened by a natural frequency of the resonator. This alteration of the dispersion curve is called mode hybridization phenomenon, which represents a crucial aspect of locally-resonant metamaterials [36, 73].

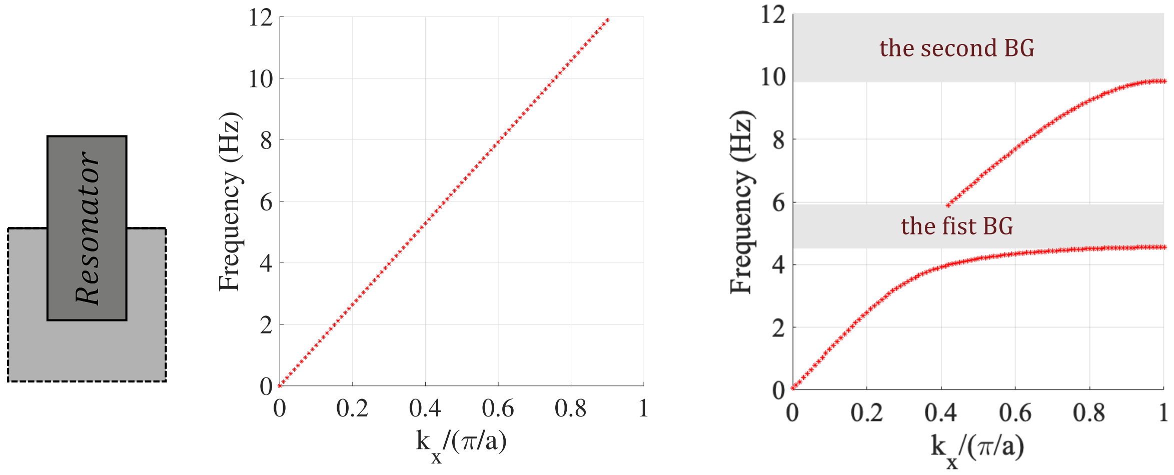

(a) Generic unit cell.

(b) Homogeneous half-space.

(c) Introducing the resonators.

Figure 4.1: Example of a generic unit cell (a) and dispersion curves for the surface wave with a homogeneous half-space (b) and introducing the infinite array of partially embedded resonators (c).

The metawedge is defined as a spatially graded arrangement of resonators applied on the surface of an elastic half-space that appears effective in converting incoming Rayleigh waves into body ones [32]. This solution is studied to investigate other mitigation mechanisms that can ensure a good vibration mitigation inside the conical region where the stiff trench gives a bad attenuation performance (see Section 3.2.3). For the metawedge technology, the wave-mode conversion mechanism proves to be the dominant one [37]. It allows redirecting part of the approaching energy deep into the ground, attenuating the induced ground motion at the surface. The wave-mode conversion mechanism has a strong potential for vibration isolation purposes in different engineering fields. The metawedge can be adopted for civil engineering applications to mitigate ground vibration.

The resonator can be generally modelled in the $xz$-plane with a rectangular cross section, as illustrated in Fig. 4.1a. To obtain the metawedge, the height of the resonators is gradually changed and the wedge shape appears [31, 32, 37, 74]. Another solution is suggested in [34], where only the embedded part of the resonators varies along the metawedge. In this case, the metawedge can also be called partially embedded gradient metabarrier, where the word metabarrier expresses the fact that it is a wave barrier based on metamaterials theory. Its schematic representation is depicted in Fig. 4.2. This solution has inspired the design suggested for the railway application in Section 4.4. The track represents the excitation source, the building describes the receiver, while the metawedge is installed on the transmission path. The coloured zones represent the propagating waves, of which flow is diverted deep into the ground (becoming body waves from surface ones). The name metawedge combines its theoretical root based on metamaterials and the wedge shape obtained with the arrangement of resonators.

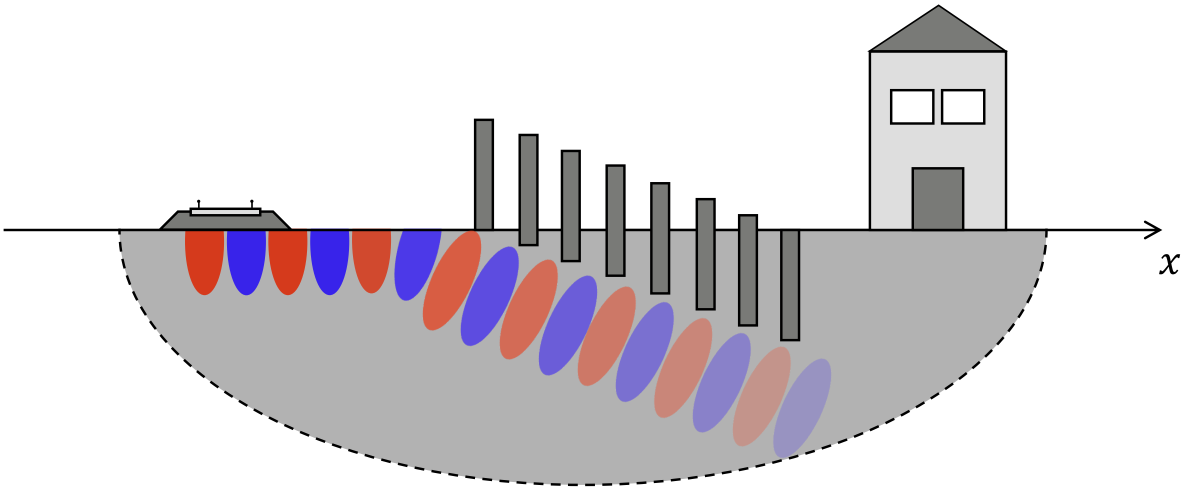

Figure 4.2: Schematic representation of the wave-mode conversion mechanism.

Different resonators have been proposed to achieve the desired vibration attenuation for a receiver at the surface. The concept of a resonant metawedge and a forest of trees as seismic metamaterial is reported in [30, 31]. Similar systems based on resonant trees - properly placed in the space - are proposed in [32, 33]. The wave-mode conversion effect can also be obtained by more complex metabarriers, these are made of single or multi mass-spring resonators [35–37].

For most cases in literature, 2D models are adopted to investigate the efficiency of a metawedge under the plane strain assumption. This work includes both 2D and 2.5D models developed in FEMIX software (see Section 3.1.1). Following the same strategy as described in Chapter 3; the resonators are modelled with finite elements, while the soil is modelled through the boundary element method. Obtaining the three-dimensional displacement field for the point load case, the effect of the metawedge can be investigated for incoming waves with different incident angles. Its performance can be examined inside the conical region where the stiff trench effect shows a less efficient vibration mitigation.

## 4.2. Unit cell and design principles

The first step in the design of a metawedge is the analysis and tuning of the unit cell dynamics inside a structure composed of an infinite number of identical cells to predict its behaviour at diverse excitation frequencies. Therefore, a periodic metabarrier made of partially embedded resonators in a homogeneous semi-infinite soil is studied. Designing the band gaps in the spectrum is the biggest challenge. It is also the most important step for developing an effective mitigation measure for the target frequency range.

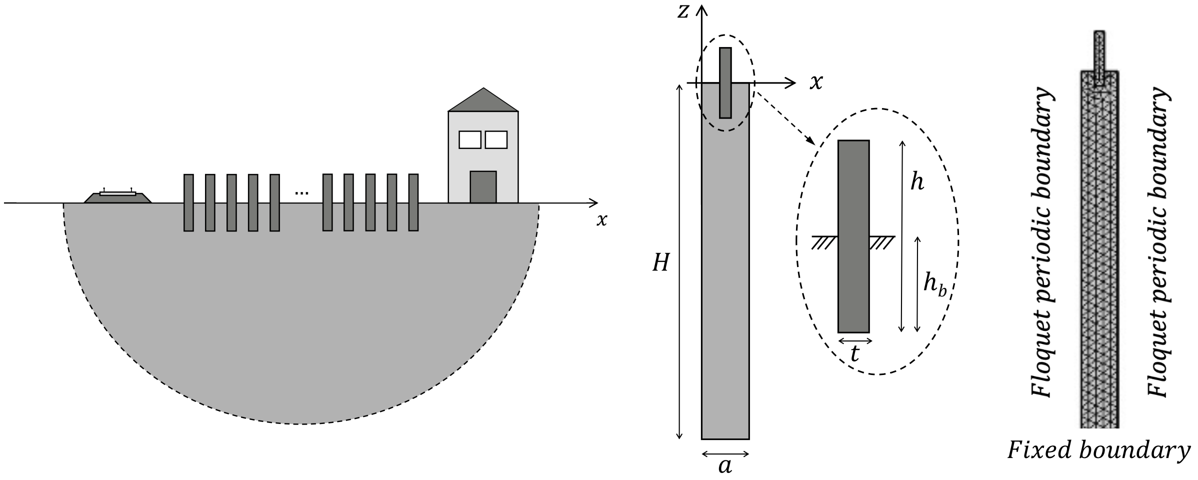

(a) Overall view. (b) Unit cell. (c) FEM model.

Figure 4.3: Schematic representation of a generic periodic metabarrier with partially embedded resonators (a), unit cell (b) and FEM model of the unit cell (c).

Fig. 4.3a displays the generic periodic array of rectangular cross section boards along the $x$ direction. In this figure, the three dots express the theoretically infinite number of unit cells. This infinite periodic system takes the name of partially embedded periodic metabarrier [34].

The unit cell of the system is shown in Fig. 4.3b. The soil column is characterized by a width $a$ and a depth $H$. Although this is not the only possible option, the soil column is considered as part of the metamaterial following the approach adopted in [34]. A different strategy is pursued in [75], where the authors propose focusing only on the resonator dynamics because this is the only well controlled part. The resonator is characterized by a width $t$ and a height $h$, of which $h_b$ part is embedded in the soil. If the system does not have any embedded part, $h_b = 0$. On the other hand, if $h = h_b$, the resonator is fully embedded in the ground and it becomes an in-filled trench.

The governing equations of elastic waves for a heterogeneous medium with isotropic material properties are taken from [34]. They can be written as

$$\rho(\mathbf{x})\ddot{\mathbf{u}}(\mathbf{x},t) = \nabla\{[\lambda(\mathbf{x}) + 2\mu(\mathbf{x})](\nabla \cdot \mathbf{u}(\mathbf{x},t))\} - \nabla \times [\mu(\mathbf{x})\nabla \times \mathbf{u}(\mathbf{x},t)]. \tag{4.1}$$

For an inhomogeneous continuum, the Lamé constants are given as a function of the coordinate vector $\mathbf{x} = [x, y, z]$. The explanation of the other terms in Eq. (4.1) is available in Chapter 1.

The system periodicity is introduced through the Floquet theorem [76, 77]. According to this theory, the displacement in a periodic structure can be expressed as

$$\mathbf{u}(\mathbf{x},t) = \mathrm{e}^{\mathrm{i}(\mathbf{kx}-\omega t)}\mathbf{u_k}(\mathbf{x}), \tag{4.2}$$

where $\mathbf{k}$ is the Bloch wave vector in the first Brillouin zone and $\mathbf{u_k}(\mathbf{x})$ is the displacement modulation function. This function is characterized by the same spatial periodicity of the structure, that means

$$\mathbf{u_k}(\mathbf{x} + a) = \mathbf{u_k}(\mathbf{x}), \tag{4.3}$$

where $a$ is the is the unit cell horizontal periodic constant (see Fig. 4.3b). From Eq. (4.2) and Eq. (4.3), it is possible to write

$$\mathbf{u}(\mathbf{x} + a, t) = \mathrm{e}^{\mathrm{i}\mathbf{k}a}\mathbf{u}(\mathbf{x},t). \tag{4.4}$$

Combining Eq. (4.4) and Eq. (4.1), the dispersion relation problem of an infinite periodic system can be transferred into an eigenvalue problem of a typical unit cell [78]. It can be expressed in the following matrix form:

$$(\mathbf{K}(\mathbf{k}) - \omega^2\mathbf{M})\mathbf{u} = \mathbf{0}, \tag{4.5}$$

where $\mathbf{M}$ is the mass matrix and $\mathbf{K}$ is the stiffness matrix, which is a function of the wavenumber vector $\mathbf{k}$. The dispersion curve of the periodic structure is determined by the wave vector in the first Brillouin zone. Due to its symmetry, examining the wave vector just along the boundary of the first irreducible Brillouin zone $(0-\pi/a)$ is sufficient [79].

In this work, the eigenvalue problem is solved numerically through a two-dimensional FEM model of the unit cell. This is developed with COMSOL Multiphysics version 5.4. An example is presented in Fig. 4.3c. The finite depth $H$ of the soil column must be large enough to accurately model the semi-infinite layer, assuring the convergence of the numerical solutions. For Rayleigh waves the motion is localized near the surface in a thin layer, which is about twice the wavelength of the surface waves [41]. Therefore, the $H$ value is taken larger than three maximum Rayleigh wavelengths ($H > 3\lambda_{R,max}$), as imposed in [34]. The term $\lambda_{R,max}$ corresponds to the minimum frequency value $f_{min}$, which is set to 1 Hz for all the presented simulations. Recalling the exponential decay of surface waves with depth, the fixed boundary condition at the bottom of the unit cell is acceptable [80]. This means $\mathbf{u} = \mathbf{0}$ at $z = -H$. Stress-free boundary conditions are used at the top free surface ($z = 0$), while the Floquet periodicity is imposed at the vertical boundaries of the unit cell (see Fig. 4.3c). A detailed explanation of the corresponding functions implemented in COMSOL Multiphysics is available in [81]. The triangular mesh is exploited in this study, as depicted in Fig. 4.3c.

Once the dispersion relations are found for the elementary cell, the surface modes must be distinguished from the bulk ones. COMSOL Multiphysics cannot detect this difference. The distinction is performed with the energy distribution parameter $\xi$, which is proposed in [82]. It reflects the energy distribution of a mode through the computation of the ratio expressed by Eq. (4.6).

$$\xi = \frac{\int_{-2\lambda}^{0}\int_{0}^{a} W_\varepsilon \, dx \, dz}{\int_{-H}^{0}\int_{0}^{a} W_\varepsilon \, dx \, dz}, \tag{4.6}$$

where $W_\varepsilon$ represents the elastic strain energy density (ESED). The surface integrals are computed for the soil column of the unit cell for its width $a$ along the $x$-axis and for the depth values $2\lambda$ and $H$ along the $z$-axis, as shown in Fig. 4.3b. This parameter - expressed by Eq. (4.6) - has a clear physical meaning, since it represents the specific energy content located within two wavelengths for the examined wave mode. The surface modes are identified for $\xi > 90\,\%$ [82]. Once the surface modes are found, the corresponding band gaps can be obtained in the frequency domain by plotting the surface mode along the first Brillouin zone (for an example case see Fig. 4.1c).

## 4.3. Model validation

Comparing the results with a literature case, the implemented model and solution technique are validated. The same strategy of Section 3.1.2 is adopted for this section. As reference case, the study presented in [34] is chosen. The effect of a concrete metawedge in a homogeneous half-space subjected to a vertical harmonic load is investigated. For brevity, the properties of the materials are listed in Appendix C. The unit cell is characterized by $t = 0.5\,\mathrm{m}$, $h = 3\,\mathrm{m}$ and $h_b = 0.8\,\mathrm{m}$; while the soil column part has $a = 2\,\mathrm{m}$ and $H = 240\,\mathrm{m}$.

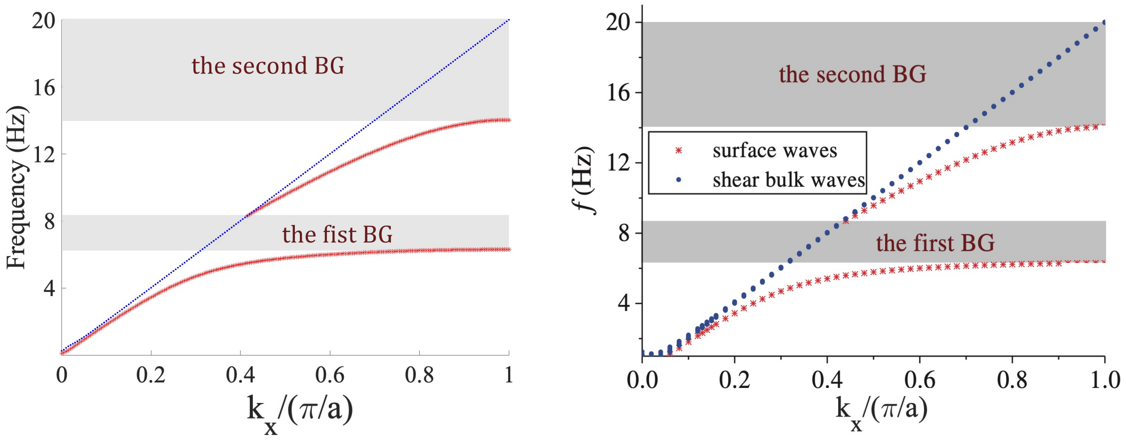

(a) Current results.

(b) Results from [34].

Figure 4.4: Model validation through dispersion curves comparison with [34].

Fig. 4.4 shows a good agreement of the dispersion curves. The first two surface wave modes are plotted, while only the first bulk mode is reported. The other bulk modes appear to be almost overlapped with the first one, so plotting only the first one is enough. The first band gap is opened by the flexural mode shape of the resonator at its first natural frequency $\omega_{n,1} = 2\pi \times 6.3\,\mathrm{Hz}$. The longitudinal mode shape initiates the second band gap at $\omega_{n,2} = 2\pi \times 14.1\,\mathrm{Hz}$. Exactly the same values are reported in [34]. The band gap terminates when the successive surface mode appears. From this agreement, the procedures to identify the different modes and to recognise the band gaps are validated.

The displacement field - computed with the 2D model for $k_y = 0$ - is compared to validate the FEMIX input file and the processing phase of its outputs. The embedded depth of the boards linearly changes with a constant gradient $\zeta = \tan(\frac{h}{na})$, where $n$ is the number of elementary cells. The model proposed in literature considers $n = 30$ sloped boards with a thickness $t = 0.8\,\mathrm{m}$. All the other parameters are maintained equal to the previously presented ones. The first resonator met by the incoming wave does not have embedded part ($h_b = 0\,\mathrm{m}$). Due to the imposed gradient, the structure ends with a completely embedded board that assumes the shape of an in-filled trench ($h_b = h$). Note that the originally published plot is cropped to help the comparison in Fig. 4.5a.

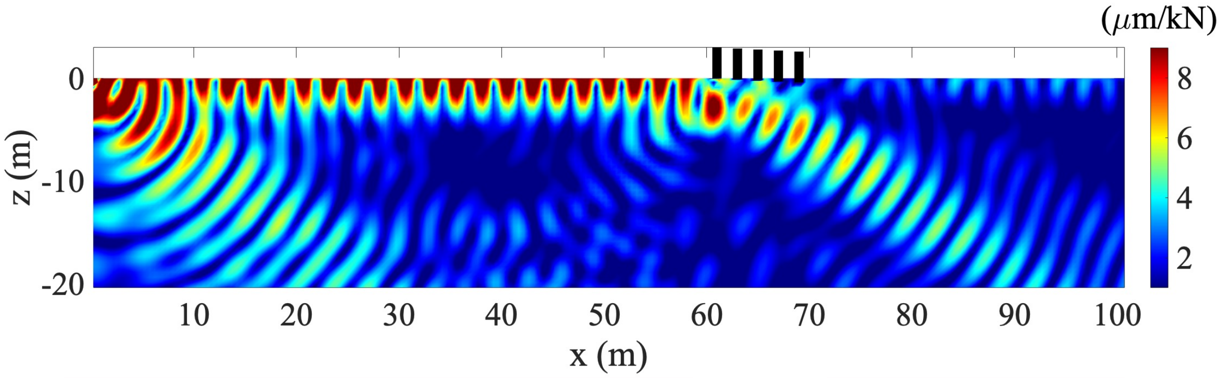

(a) Results from author's work with FEMIX.

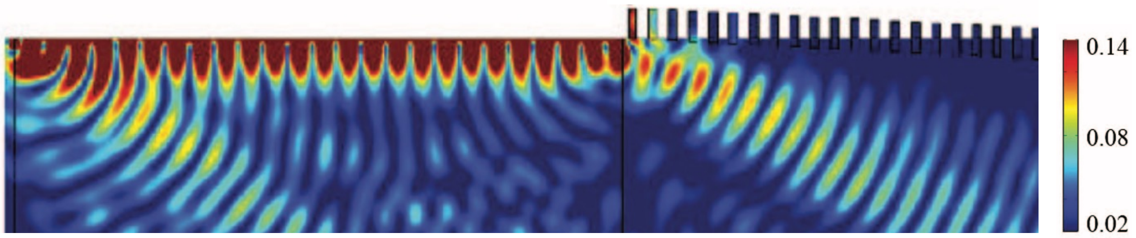

(b) Results from [34].

Figure 4.5: Model validation through displacement field comparison with [34].

The vertical harmonic excitation is applied 60 m far from the first unit cell, and is characterized by a unit displacement amplitude. The excitation frequency is set equal to 15 Hz. Modelling in FEMIX all the 30 resonators with finite elements is practically difficult due to an excessive request for memory allocation. Nevertheless, a similar outcome is achieved with just the first five unit cells, as displayed in Fig. 4.5. The depicted displacement is generally computed with the real parts of the three components as $u_{\mathrm{Re}} = \sqrt{(\mathrm{Re}(u_x)^2 + \mathrm{Re}(u_y)^2 + \mathrm{Re}(u_z)^2)}$. Another difference between the models lies in the excitation form because a unit force is applied in FEMIX, instead of a unit displacement. This incongruity generates different amplitudes in Fig. 4.5a and Fig. 4.5b. The damping coefficient values are also different. To obtain Fig. 4.5b, null damping is imposed. This is not possible in FEMIX due to numerical problems, so a small damping coefficient ($\xi_d = 0.5\,\%$) is set to achieve a good match of the results.

From Fig. 4.4 and Fig. 4.5, the qualitative good agreement of the outcomes allows the validation of the adopted model. Therefore, the model is used in the next sections to further analyse the performance of the metawedge for a railway application.

## 4.4. Simulation and effect of modelling parameters

Inspired by metawedges for seismic application, the wave-mode conversion mechanism is adopted for the attenuation of railway traffic-induced ground vibration. In the following, the possibility to design the metawedge for a specific railway application is presented. Developing a possible alternative to the stiff in-filled trench represents the main goal of this section. Based on the cargo train induced vibration problem for the Tricht site (see Chapter 2), a metawedge system with promising mitigation performances is proposed. The step-by-step design is presented and the influence of different materials is investigated together with the effect of the unit cell dimension.

### 4.4.1. Case study: metawedge in a homogeneous half-space

To present an innovative countermeasure as a practically feasible solution, some realistic design constraints must be set. The current study treats the vibration problem generated by the passages of cargo trains from Chapter 2. The primary objective of this section is to propose a viable alternative to the usual mitigation measures, which has improved performance, especially inside the conical region where the stiff trench shows a poorer vibration mitigation (see Section 3.2.3). The metawedge must be able to shield the surrounding buildings from the railway induced ground vibration.

The metawedge is embedded in a homogeneous half-space to support the physical interpretation of the results, as similarly done for the stiff trench in Section 3.2. A unit vertical point harmonic force - applied 60 m far from the first unit cell - represents the input excitation. The convention of the right-hand Cartesian coordinate system is the same as Section 3.3.1. Fig. 4.6 displays the problem invariant geometry in the $xz$-plane. The receiver points is located at the surface level for $120\,\text{m} < x < 160\,\text{m}$.

The soil properties are chosen from the Tricht site and they are taken equal to those of its first ground layer, they are listed in Table 2.1. For the ground, this means density $\rho = 1700\,\text{kg/m}^3$, Young's modulus $E = 15\,\text{MPa}$ and Poisson's ratio $\nu = 0.40$ (cf. Table 2.1). The damping coefficient is set equal to $0.5\,\%$, focusing the reader's attention on the metawedge performance and not on the material damping effect. Similarly, large distances between the entities are imposed to guarantee a marginal role of the body waves at the metawedge position.

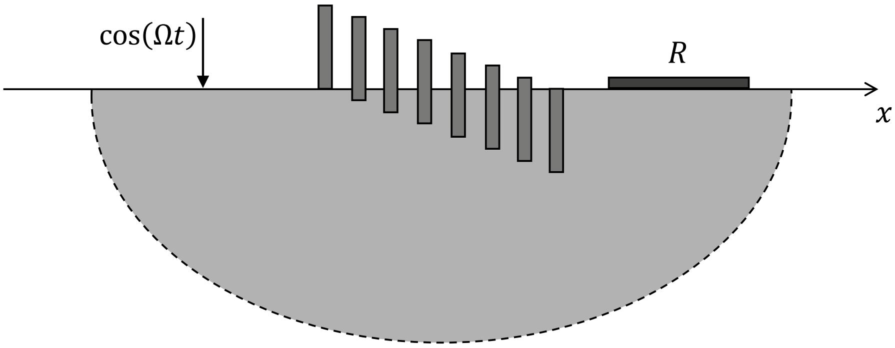

Figure 4.6: Lateral view of the wave propagation problem in the homogeneous half-space with metawedge, the grey rectangle with the $R$ letter indicates the receiver points location (figure not to scale).

The metawedge should ideally be able to redirect the surface waves for the frequency interval that is mostly excited by the passage of cargo trains. From the field measurements presented in Chapter 2, it is found in $5-10\,\mathrm{Hz}$ range. Particular attention is paid to $6\,\mathrm{Hz}$ because it is the most excited frequency by the running vehicle [39].

The designed solution should be as small as possible, in the ideal case the system should be compact. The main idea consists in developing a practically feasible structure that is not strongly intrusive in an urbanized area [35].

## 4.4.2. Proposed metawedge solution

The imposed constraints of the previous section guide the design of the metawedge. The proposed solution shows partially embedded resonators. The system showing the best achieved mitigation performance is presented. Starting from the unit cell, the selected resonator board is characterized by a thickness $t = 0.2\,\mathrm{m}$ and a total height $h = 3\,\mathrm{m}$. The soil part of the unit cell has thickness $a = 2\,\mathrm{m}$ and total depth $H = 240\,\mathrm{m}$. Steel has been chosen for the resonator material. Steel has a density $\rho = 7830\,\mathrm{kg/m^3}$, a Young's modulus $E = 200\,\mathrm{GPa}$ and a Poisson's ratio $\nu = 0.26$ [34]. Table 4.1 summarizes the properties.

Table 4.1: Metawedge properties.

| Material | $\rho\,(\mathrm{kg/m^3})$ | $E\,(\mathrm{GPa})$ | $\nu$ | Height (m) | Thickness (m) |
|---|---|---|---|---|---|
| Steel | 7830 | 200 | 0.26 | 3 | 0.2 |

Following the design procedure described in Section 4.2, the dispersion curves of the surface waves can be calculated. They are depicted in Fig. 4.7 for the $h_b = 0.4\,\mathrm{m}$ unit cell. The flexural and longitudinal modes also given in the right side of the figure. They are associated with the eigenfrequencies at the lower edge of the band gaps. The related colour bar indicates the displacement amplitude.

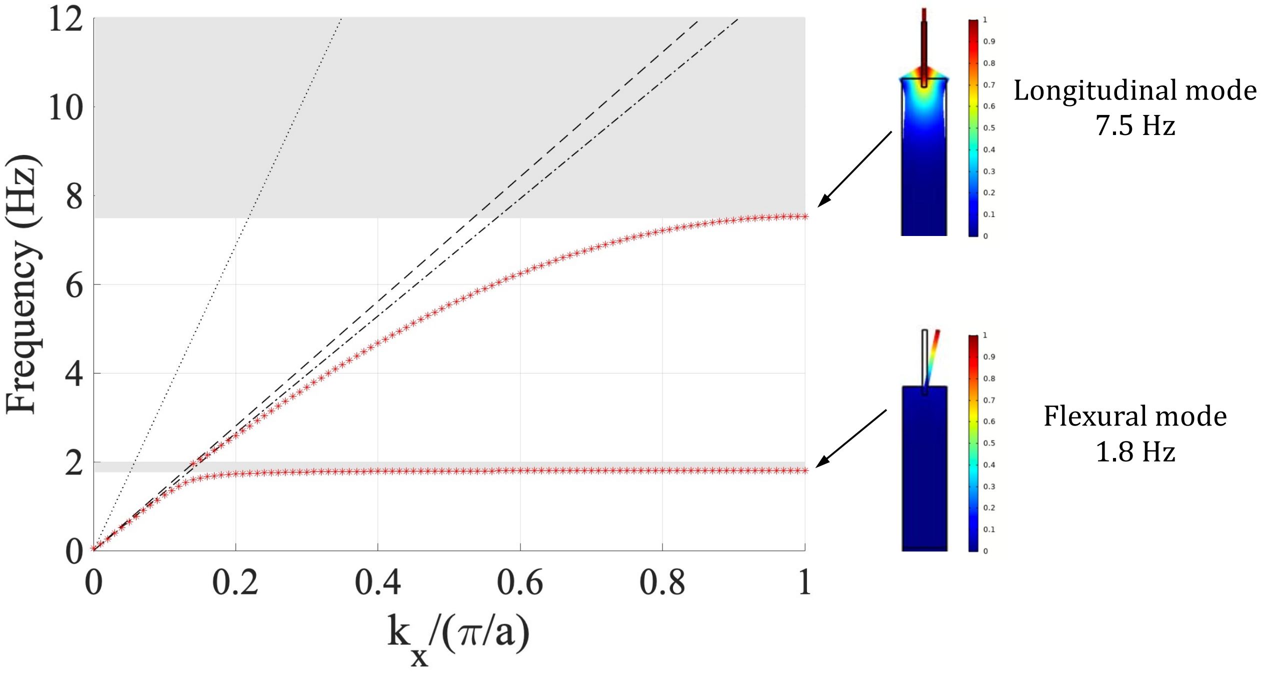

Figure 4.7: Dispersion curves of the surface wave (red star) for the $h_b = 0.4\,\mathrm{m}$ unit cell. Superimposed are the dispersion curves of compressional (dotted line), shear (dashed line) and Rayleigh (dashed-dotted line) waves for the homogeneous soil.

The vibration mode of the unit cell manipulates the wave propagation in the medium through the Rayleigh mode hybridization with the surface resonances [83]. Without the boards, the dispersion curves are just those of bulk and surface Rayleigh waves, which are described by the straight black lines in Fig. 4.7. Above the two natural frequencies corresponding to the flexural and longitudinal modes, two distinct band gaps appear. In these ranges, the Rayleigh wave cannot propagate. The solution becomes strongly dispersive around the flexural and longitudinal natural frequencies. Outside the $\frac{\omega}{k} < c_{S,Soil}$ cone, all the arising modes are guaranteed to be surface ones [84]. As observed, no surface modes appear inside the cone or in the band gaps because the surface solutions become radiation modes. The energy travelling at the surface with Rayleigh waves is diverted into the bulk in the form of body waves [35]. This phenomenon generates the two separate branches of "hybrid" Rayleigh waves that asymptotically approach the band gaps from the bottom with a phase velocity lower than $c_R$ [36]. The band gap closes when the upper branch shows the phase velocity equal to $c_{S,Soil}$. Surface modes with phase velocity larger than $c_{S,Soil}$ cannot exist in the elastic medium. Although the elliptically Rayleigh wave excites both modes of the metabarrier, only the longitudinal one is able to activate a considerable band gap. Depending on the unit cell geometry and properties, the flexural mode plays a more or less marginal role. It appears extremely narrow for this specific case (about $1.8 - 2\,\text{Hz}$). Some authors directly neglect the contribution of the first resonance [30, 32]. Above the longitudinal mode, the second band gap appears wider due to the better wave and mode coupling with the vertical component of the Rayleigh wave [33].

The band gaps are tuned by adjusting the embedded depth of the board with the metawedge along the $x$-axis. This layout guarantees that the mitigation mechanism of the countermeasure is dominated by the wave-mode conversion of Rayleigh waves into bulk ones, as demonstrated in [32]. In particular, the second band gap should be shifted to lower frequencies to reach at least the target value of 6 Hz. Surface waves should experience a clear conversion when this excitation frequency is imposed at the surface.

The dispersion curves are computed for several unit cells with different embedded depth values ($0\,\text{m} \leq h_b \leq 1.8\,\text{m}$). The evolution of the first two band gaps is plotted as a function of $h_b$ in Fig. 4.8. As indicated, the regions between the two equal curves express the interval of the band gaps. With this metawedge setup, the Rayleigh waves travelling from left to right experience an increasing $h_b$ trend.

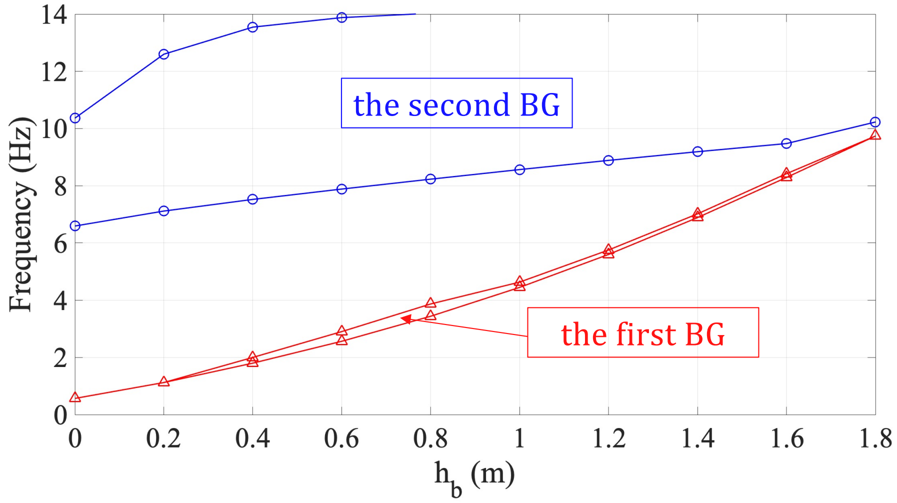

Figure 4.8: Relations first band gap (red triangle) and second one (blue circle) with embedded depth $h_b$.

The figure suggests that the second band gap can reach smaller frequencies if $h_b$ is decreased. Beginning with the first board with $h_b = 0$, the first five barriers with the embedded depth difference $\Delta h_b = 0.1\,\mathrm{m}$ are selected. This implies that the fifth barrier has $h_b = 0.4\,\mathrm{m}$ with the imposed slope $\zeta = 0.05$. Fig. 4.9 offers a qualitative illustration of the designed solution. The heavy resonators would need some foundations to keep them straight and to prevent settling. In the models used for this study, their presence is neglected for simplicity but note that they could affect the resulting mitigation effect.

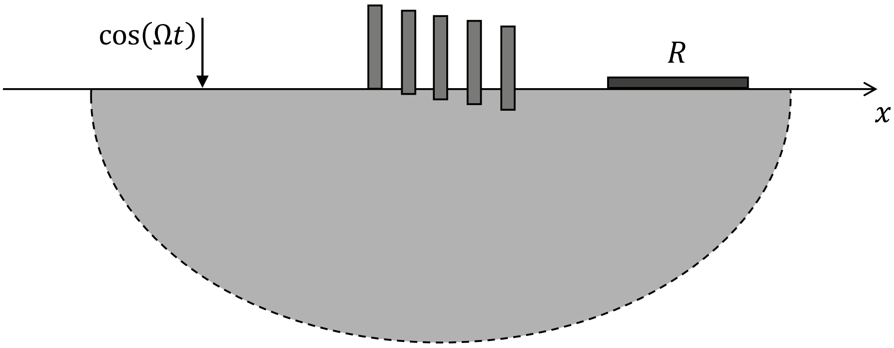

Figure 4.9: Lateral view of the designed metawedge for the railway application, the grey rectangle with the $R$ letter indicates the receiver points location (figure not to scale).

The mitigation performance of the designed system is firstly assessed with a 2D model in the space-frequency domain under the plane strain assumption ($k_y = 0$). The resonators are modelled with finite elements, while boundary elements are used for the soil domain. The vertical harmonic force represents the excitation input and the displacement output at the receiver points is computed.

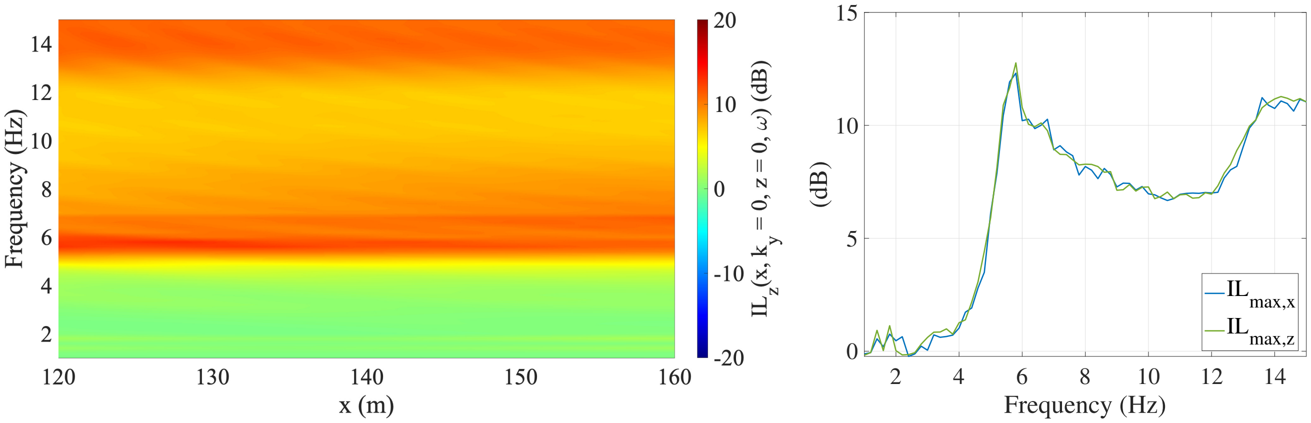

(a) $\mathrm{IL}_z(x, k_y = 0, z = 0, \omega)$.

(b) $\mathrm{IL}_{max,x}$ and $\mathrm{IL}_{max,z}$.

Figure 4.10: Assessment of the proposed metawedge solution.

Fig. 4.10a shows the vertical insertion loss value - calculated with Eq. (2.4) - at the surface level for different excitation frequencies and horizontal positions. The system appears clearly effective in mitigating the vibration for $\omega > \Omega = 2\pi \times 5\,\text{Hz}$. Fig. 4.10b shows the insertion loss computed with the maximum real part of the displacements occurring in the receiver points. This is defined as $\text{IL}_{max}$. It depicts how the peak performance of the metawedge is achieved around 6 Hz, after a steep increase. A similar outcome is obtained for the horizontal component of the soil response, it is available in Appendix C.

The outputs presented in Fig. 4.10 prove that the designed solution is able to mitigate vibration following the design constraints previously recommended. To check that the beneficial effect is realized through the wave-mode conversion mechanism, the displacement distribution in space $u_{\text{Re}}(x, k_y = 0, z, \Omega)$ is computed using FEMIX for the target excitation frequency $\Omega = 2\pi \times 6\,\text{Hz}$ and presented at the bottom part of Fig. 4.11.

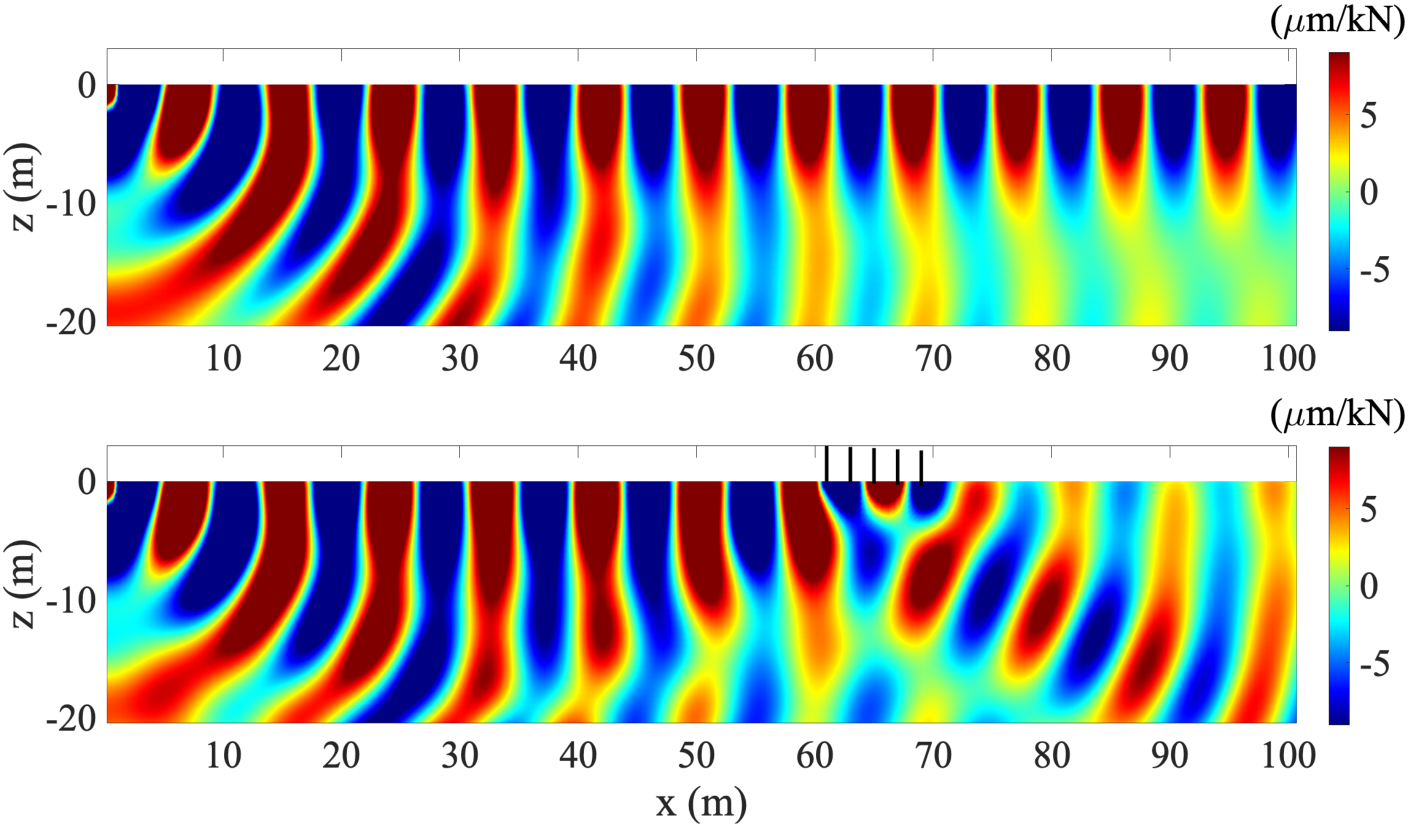

Figure 4.11: Real part of the vertical displacement component $\text{Re}(u_z(x, k_y = 0, z, \Omega = 2\pi \times 6\,\text{Hz}))$ generated by vertical harmonic load in homogeneous soil (first row) and with metawedge (second row).

The wave-mode conversion mechanism is visible in Fig. 4.11. The surface wave is clearly redirected into the deep soil when it passes the metawedge. This process attenuates the motion amplitude at the surface level behind the barrier, as already indicated by Fig. 4.10. The advantageous effect of the mitigation measure is even more evident when comparing the two plots in Fig. 4.11. The top plot represents the homogeneous soil case without the metawedge. Similar results appear for the $u_{\mathrm{Re}}$ and the real part of the horizontal component $\mathrm{Re}(u_x)$, the corresponding figures are collected in Appendix C.

The mitigation performance of the designed metawedge is evaluated with the 2.5D model in the three-dimensional space. As already done for the stiff in-filled trench analysis, the insertion loss is computed in the space-wavenumber-frequency domain. Fig. 4.12 represents the vertical insertion loss for a receiver point that is located at the surface level with $x = 120\,\mathrm{m}$.

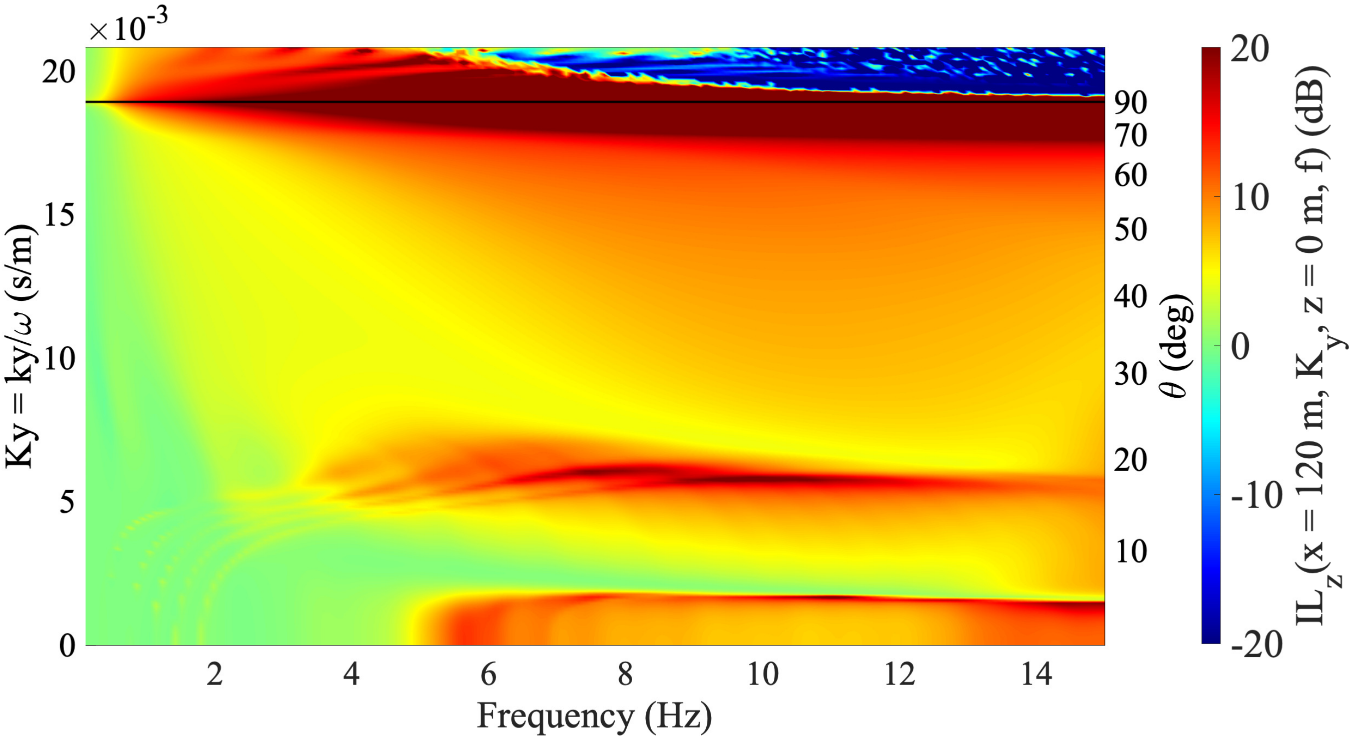

Figure 4.12: Vertical insertion loss $\mathrm{IL}_z(x = 120, K_y, z = 0, \omega)$ for the designed metawedge embedded in homogeneous half-space. Superimposed is the dispersion curve Rayleigh wave (solid line).

In Fig. 4.12, the designed metawedge shows positive insertion loss values for a wide region. The metawedge is ineffective below a certain frequency (1 Hz). This feature recalls the critical frequency that is generated by the stiffness effect, the key mitigation mechanism of a stiff in-filled trench (Section 3.2.3). The metawedge is particularly effective at low propagation angle $\theta$. This means that the conical region characterized by nearly zero insertion loss (see Section 3.2.3) is not present for frequency above 5 Hz. The corresponding plot for the insertion loss in the horizontal direction $\mathrm{IL}_x$ is displayed in Appendix C.

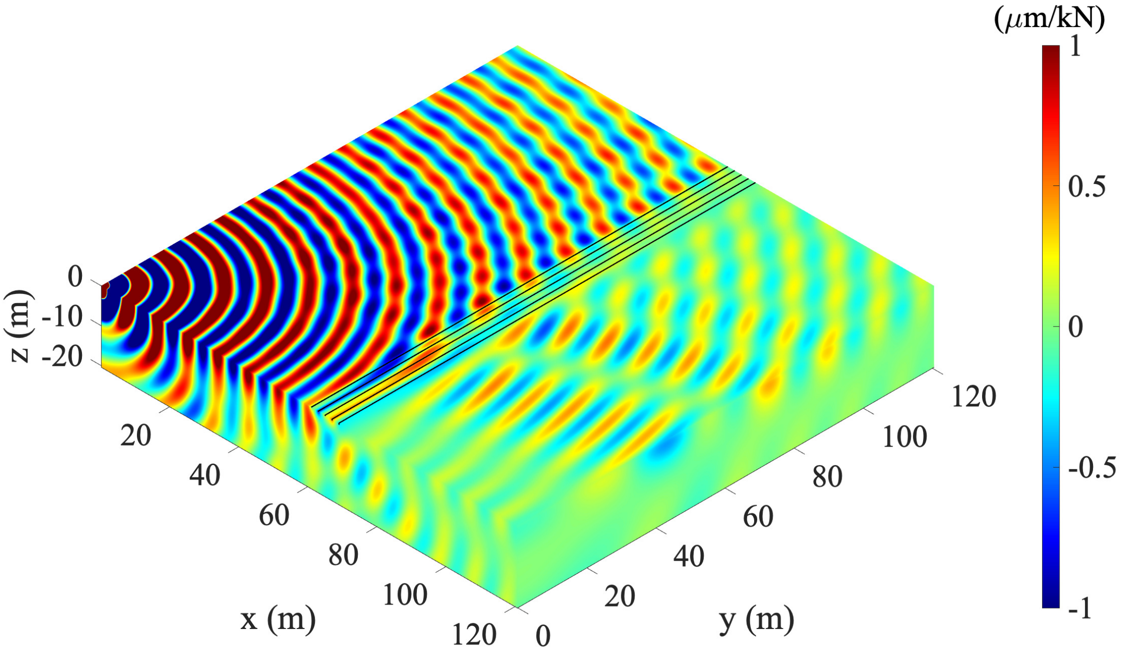

(a) $\mathrm{Re}(u_z(x, y, z, \Omega = 2\pi \times 6\,\mathrm{Hz}))$.

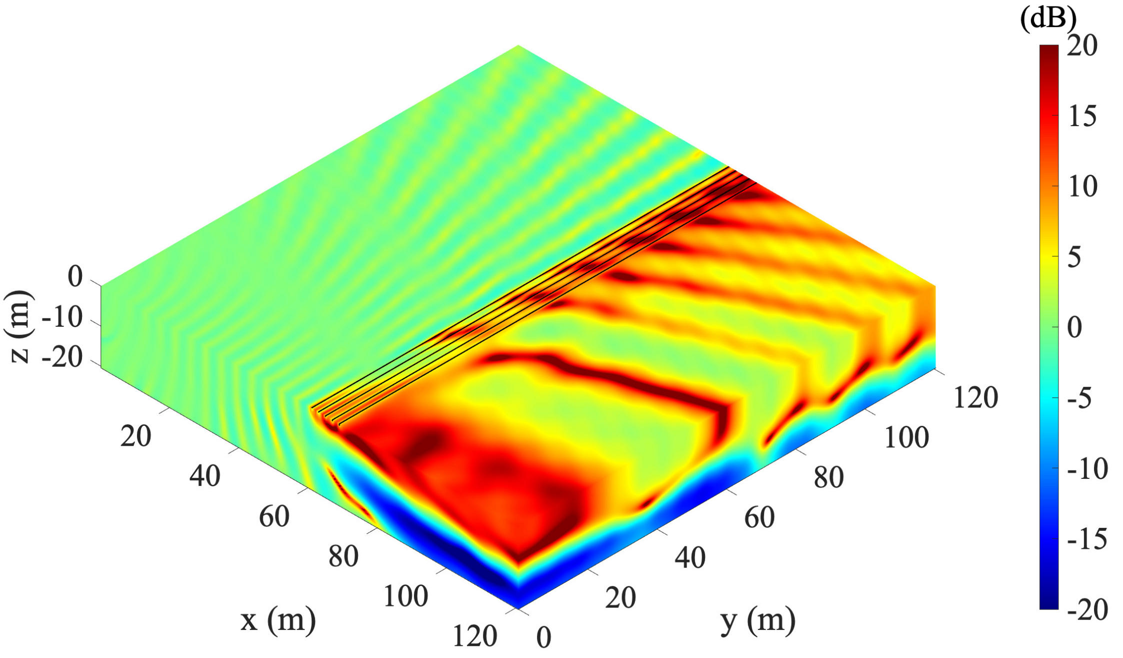

(b) $\mathrm{IL}_z(x, y, z, \Omega = 2\pi \times 6\,\mathrm{Hz})$.

Figure 4.13: Real part of the vertical displacement component (a) and vertical insertion loss (b) generated by unit harmonic vertical point load.

Applying the inverse Fourier transform, the soil response is found in the space-frequency domain. The displacement field of the vertical component and the vertical insertion loss are plotted for $\Omega = 2\pi \times 6\,\mathrm{Hz}$ in Fig. 4.13a and Fig. 4.13b, respectively. To avoid hidden zones in the box-type plots, only the embedded parts of the resonators are shown in Fig. 4.13b, they are indicated by black bands.

The metawedge appears particularly effective in mitigating the vibration along the $x$-axis in the above-mentioned conical region behind the resonators. This aspect marks an important difference from the stiff trench countermeasure, which generally shows poor performance in that cone (cf. Section 3.2.3). For some specific $\theta$ values, the metawedge seems unable to redirect the incoming wave deep into the ground. This is probably given by the different resonator properties that the incoming waves experience reaching the metawedge at $\theta > 0$. On the other hand, the wave-mode conversion phenomenon is clearly depicted in the $xy$-plane, where negative insertion loss zones appear for $z < -10\,\mathrm{m}$. These figures confirm that the metawedge is complementary to the stiff in-filled trench, showing the potential of the metawedge mitigation measure. If properly designed, it can represent a valid alternative to the stiff trench. Moreover, a very good attenuation could be achieved through a combined system, which could be basically produced by a metawedge ending with the last resonator that is a stiff trench, i.e., an entirely embedded resonator.

### 4.4.3. Influence of the resonator dimension

Changing the dimension of the resonator modifies the band gap range in the frequency spectrum and the dispersion relations.

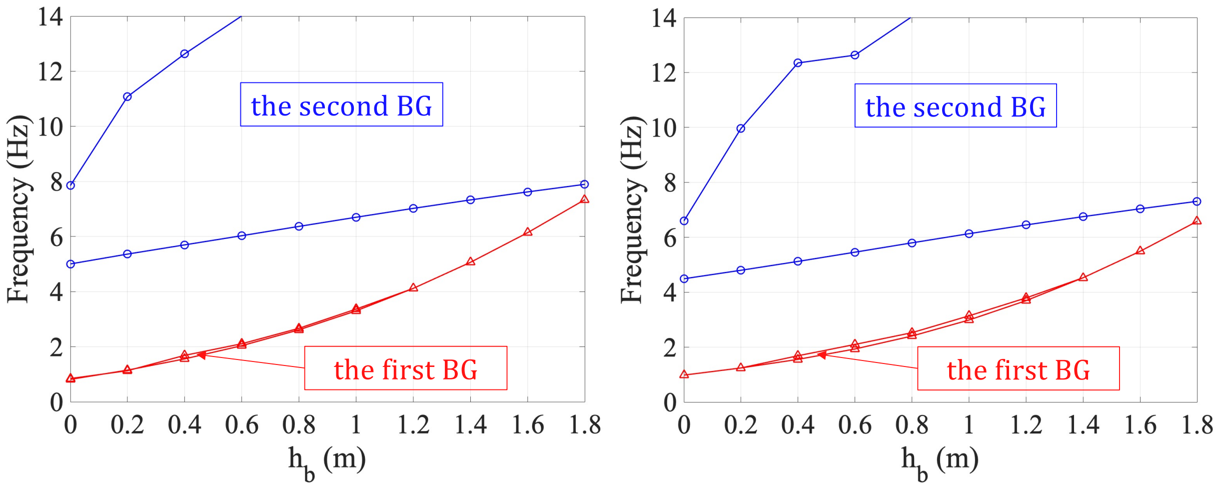

(a) $t = 0.5\,\mathrm{m}$ and $h = 3\,\mathrm{m}$.

(b) $t = 0.8\,\mathrm{m}$ and $h = 3\,\mathrm{m}$.

Figure 4.14: Relations first band gap (red triangle) and second one (blue circle) with embedded depth $h_b$.

The dimension variation is proportionally related to the resonator mass, which modifies the natural frequencies of the unit cell. The relations of the first two band gaps with the embedded depth $h_b$ are offered in Fig. 4.14 for resonators with a larger width. The resonator thickness $t$ increases to $0.5\,\mathrm{m}$ and $0.8\,\mathrm{m}$. The other parameters are maintained equal to the ones described in Section 4.4.2. The computed outcomes are presented in Fig. 4.14a and Fig. 4.14b.

The overall shape of the plot remains almost unaltered (cf. Fig. 4.8). The flexural mode effect is still too weak to open an effective band gap, it even disappears for some $h_b$ values. Generally, the longitudinal natural frequency of the unit cell opens the second band gap at lower frequencies. This trend implicates the activation of the wave-mode conversion mechanism at a lower frequency in the spectrum. The drawback corresponding to a thickness increment lies in a bigger system. More material is required and the structural aspects can become critical due to the bigger mass involved.

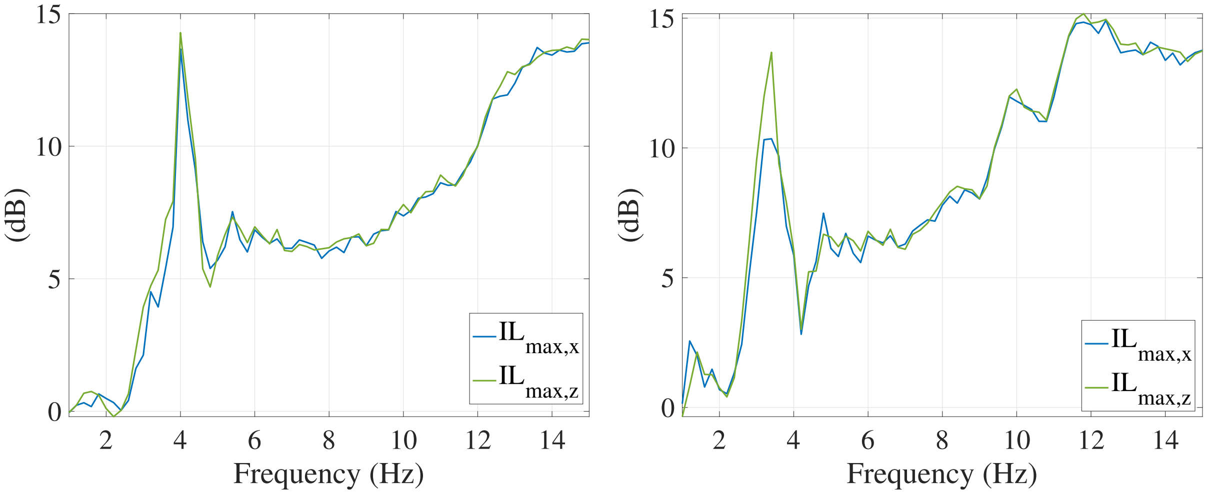

(a) $t = 0.5\,\mathrm{m}$ and $h = 3\,\mathrm{m}$.

(b) $t = 0.8\,\mathrm{m}$ and $h = 3\,\mathrm{m}$.

Figure 4.15: $\mathrm{IL}_{max}$ with resonator thickness $t$ increase.

Fig. 4.15 confirms the above-mentioned behaviour. The attenuation effect begins at lower frequencies if the longitudinal resonance lowers due to a board thickness increase. After the thickness, also the height effect is examined. Shorter resonators with $h = 2\,\mathrm{m}$ and different widths are selected for the metawedge. Their vibration attenuation performance is visible in Fig. 4.16. The resonator mass is diminished in this manner, inducing the opposite effect of the already commented width growth. As expected, the resonator height reduction leads to a delayed activation of the second band gap, which occurs at higher frequency values. For the resonator with $h_b = 0.4\,\mathrm{m}$, the second eigenfrequency

$\omega_{n,2}$ results larger than the corresponding cases with $h = 3\,\mathrm{m}$. In particular, they result in 8.7 Hz for $t = 0.2\,\mathrm{m}$ and in 6.7 Hz for $t = 0.5\,\mathrm{m}$. Vice versa, $\omega_{n,2}$ becomes smaller when the resonator mass is increased through a bigger resonator (see Fig. 4.14).

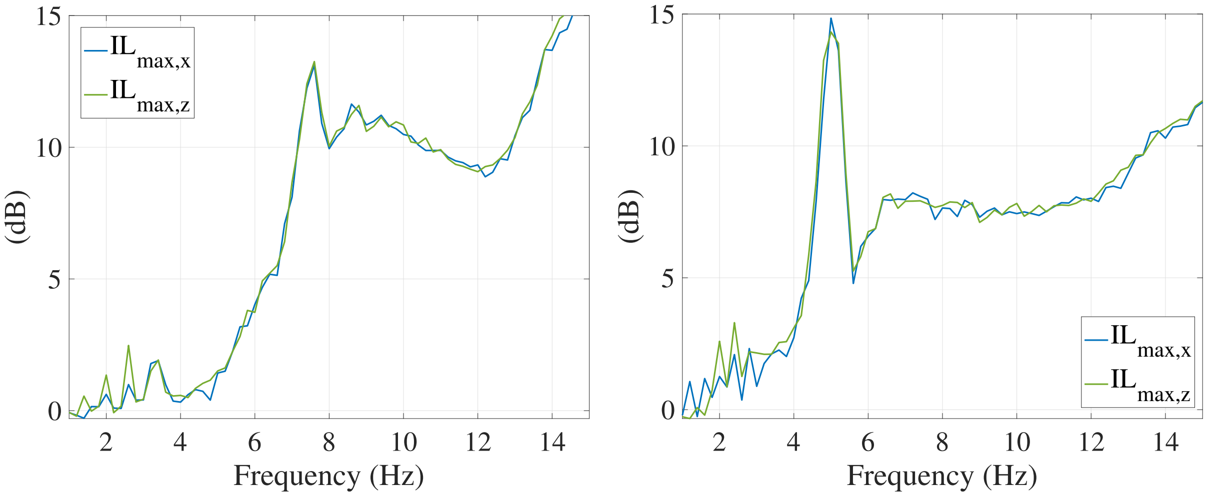

(a) $t = 0.2\,\mathrm{m}$ and $h = 2\,\mathrm{m}$.

(b) $t = 0.5\,\mathrm{m}$ and $h = 2\,\mathrm{m}$.

Figure 4.16: $\mathrm{IL}_{max}$ with resonator height $h$ decrease.

The achieved results demonstrate how different dimensions can be tested to achieve the mitigation of the target excitation frequencies. Indeed, changing the dimension of the resonator modifies its mass, which allows adapting the longitudinal natural frequency to the specific needs. However, these changes could involve critical aspects that must be carefully considered to propose a plausible solution. Especially for the mitigation of small excitation frequencies, a need for excessive mass could generate a practically unfeasible solution.

### 4.4.4. Influence of the material properties for the resonator and soil

This section investigates the effect of the material properties on the metawedge mitigation performance. The initial Young's modulus of the resonator steel and soil are decreased to evaluate the importance of this variable on the two media. In particular, $E_{Steel} = 100\,\mathrm{GPa}$ and $E_{Soil} = 7.5\,\mathrm{MPa}$ are taken. All the other parameters are kept constant and equal to the ones of Section 4.4.2. The obtained $\mathrm{IL}_{max}$ plots are presented in Fig. 4.17. Fig. 4.17a shows the outcome for the softer steel and reference soil, while Fig. 4.17b corresponds to the reference steel and softer ground.

The variation of the Young's modulus for the steel of the resonators does not seem to affect the result. The computed insertion loss shows almost the same values and trend as the reference case (cf. Fig. 4.10b). Indeed, the curves appear almost overlapped. Other scenarios with even smaller values of $E_{Steel}$ have been investigated (50 GPa and 10 GPa), but the outcomes are both similar to the left plot of the figure. This means that a variation of the resonator Young's modulus is not able to significantly move the band gaps in the frequency spectrum, i.e., the dispersion curves of the unit cells remain almost unvaried. For example, the longitudinal eigenfrequency still occurs at 7.5 Hz for the $h_b = 0.4$ m unit cell. As observed, the Young's modulus of the resonator has a marginal effect. It can be stated if the resonator has a limited embedded part, while a much stronger influence would be expected if the resonator assumes an in-filled trench aspect with most of the height that is embedded in the soil.

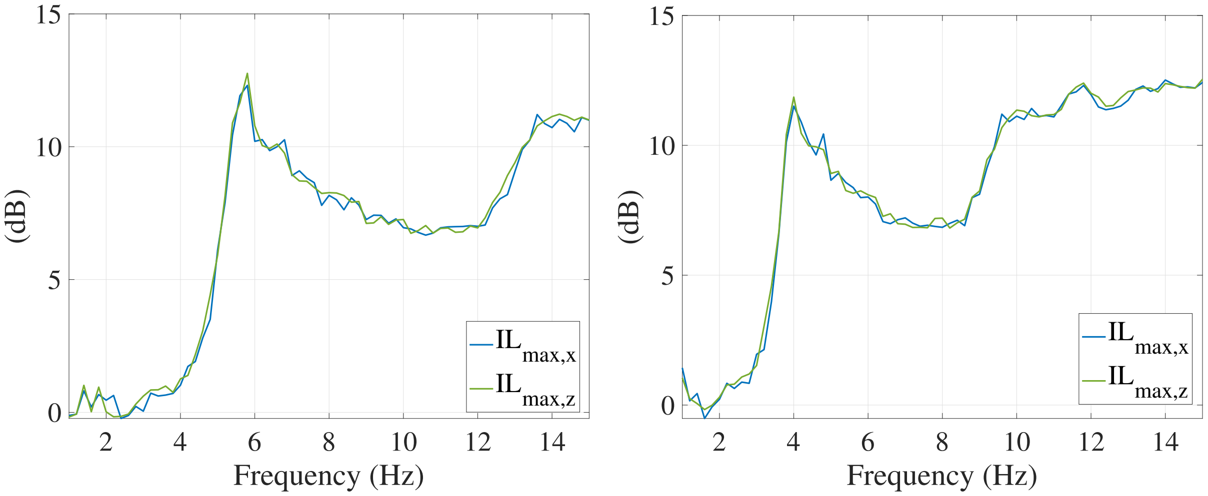

(a) $E_{Steel} = 100$ GPa and $E_{Soil} = 15$ MPa.

(b) $E_{Steel} = 200$ GPa and $E_{Soil} = 7.5$ MPa.

Figure 4.17: $\text{IL}_{max}$ for softer steel and reference soil (a) and for reference steel and softer soil (b).

The strong effect of the soil Young's modulus is proven by Fig. 4.17b. A unit cell with softer soil presents the longitudinal natural mode at a lower frequency than the reference case ($\omega_{n,2} = 2\pi \times 5.1$ Hz for the fifth unit cell). Indeed, the second band gap opens at a lower frequency for a softer soil compared to a stiffer one [37]. This aspect - qualitatively equivalent to a resonator mass increase - induces a better vibration mitigation for smaller excitation frequency.

A concrete metawedge with $t = 0.5$ m resonators is examined to complete the analysis of the material properties. The concrete is characterized by mass density $\rho = 2500\,\text{kg/m}^3$, Young's modulus $E = 30$ GPa and Poisson's ratio $\nu = 0.2$ [85]. The material choice and the increased width $t$ are the only differences compared to the reference steel metawedge, which is presented in Section 4.4.2.

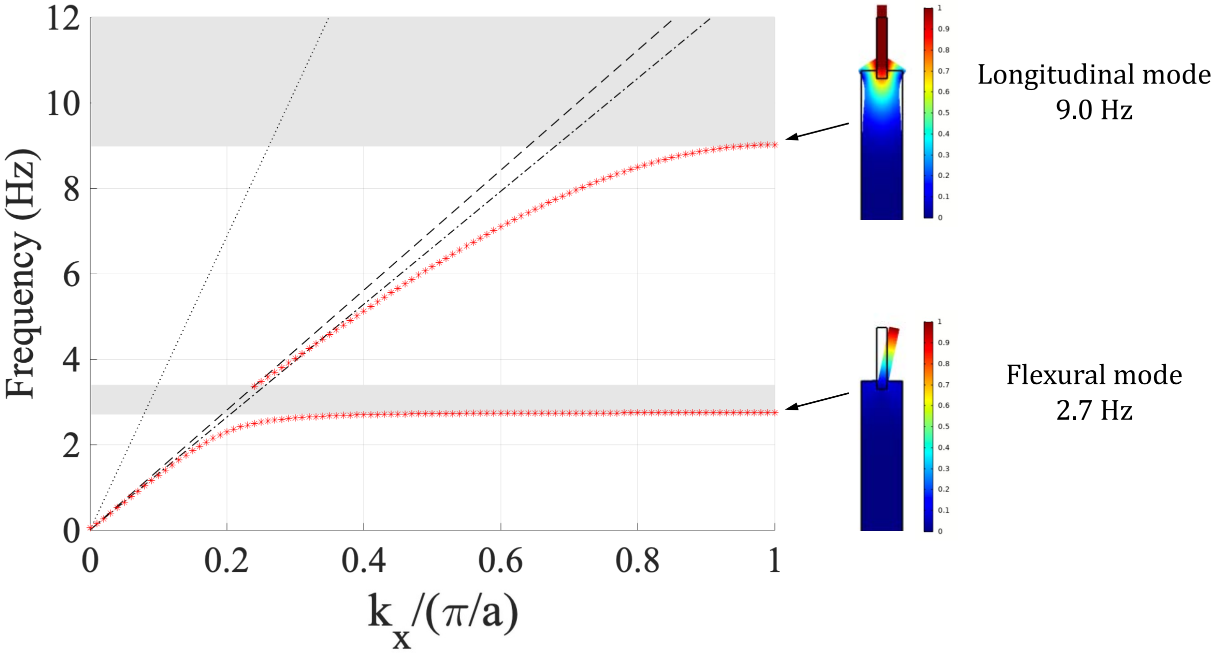

Figure 4.18: Dispersion curves of the surface wave (red star) for the $h_b = 0.4\,\mathrm{m}$ concrete unit cell. Refer to Fig. 4.7 for the description of the superimposed curves.

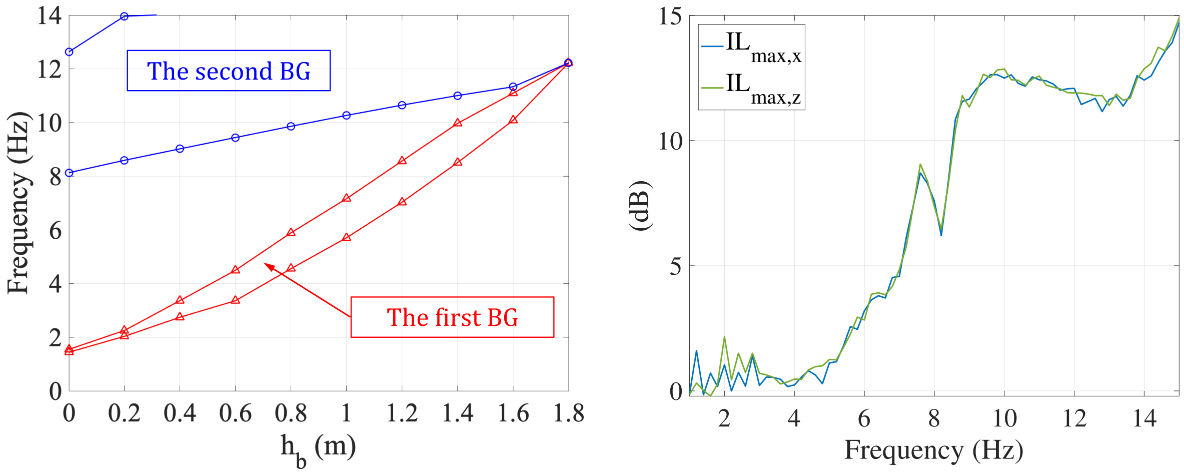

(a) Relations first band gaps with embedded depth $h_b$.

(b) $\mathrm{IL}_{max,x}$ and $\mathrm{IL}_{max,z}$.

Figure 4.19: Concrete metawedge.

Although a thicker cross section is set, the new resonators are characterized by a smaller mass due to the reduced $\rho$. According to the previous results, this should lead to an upward shift of the second band gap in the spectrum, activating the wave-mode conversion mechanism at higher frequencies. The dispersion curves for the fifth unit cell in Fig. 4.18 confirm the above-stated statement. The second band gap is activated by the longitudinal mode at 9.0 Hz, while the flexural one appears at 2.7 Hz. This effect clearly emerges from Fig. 4.19a, where the band gaps result raised up with respect to the analogous steel case, which is depicted in Fig. 4.14a. Despite the wider first band, it does not contribute to the wave attenuation. Indeed, Fig. 4.19b does not display relevant performance for its activation range.

In this section, the importance of the material properties is shown. A softer soil appears beneficial to obtain an improved vibration mitigation effect at lower frequencies. On the other hand, increasing the stiffness difference between the two media through an increase of the resonator Young's modulus does not produce significant effects. Thus, differently from the stiff trench, having a larger stiffness difference does not always give a better mitigation performance. Furthermore, the relevance of the resonator mass is again pointed out by the concrete metawedge. Due to a lower density, a concrete resonator results in lower mass compared to a steel one. Therefore, the second band gap is activated at higher frequencies.

# Part C

# Conclusions and further development

# Conclusions and further development

## Conclusions

The first objective of this thesis is the investigation of the stiff trench mitigation mechanisms and behaviour to improve the existing design guidelines. Its effect and vibration attenuation performance are firstly assessed through field measurements, which were previously acquired during in-situ tests. The recorded signals show how the stiff trench effectively decreases the transmitted waves at the surface level. The energy content is strongly reduced for the vertical component of velocity, while inconsistent results are obtained for the horizontal direction (perpendicular to the railway track).

The performance of the stiff trench and the influence of the most relevant design parameters are analysed with a 2.5D model. The countermeasure is firstly embedded in a non-dispersive homogeneous half-space to facilitate the physical interpretation and understanding of the results. The simulation outputs demonstrate that the stiffness contrast between soil and trench materials is the most important feature to obtain a beneficial vibration mitigation, which can be achieved by increasing this stiffness difference between the two media. The described effect - namely the stiffness effect - is well illustrated by the analysis in the space-wavenumber-frequency domain. The bending modes obtained with the beam model of the trench turn out to be a crucial aspect for the vibration mitigation of the stiff trench. The mitigation mechanism leads to the definition of a critical frequency. Above this frequency value, the stiff trench effectively attenuates the ground vibration. A critical angle can also be defined, it corresponds to the activation point for the bending mode, becoming important for the vibration mitigation. The results in the space-frequency domain show that the stiffness effect generates a conical area where the countermeasure has almost no effect. Within this cone region, the incoming waves are transmitted practically undisturbed. The excitation frequency value plays another important role because the trench provides a more effective vibration attenuation at increasing frequencies.

The outlined physical mechanisms are also identified for the case of a layered half-space, even though the interpretation of the results appears more complex due to the multiple wave reflections among the different ground layers. To guarantee the best possible vibration attenuation with a stiff trench, the ideal situation would involve a stiffer trench in a softer soil that is excited at a higher frequency.

Comparing the in-situ measurement results for the non-moving source with the results of the numerical simulation, they do not show a good agreement. This is mainly observed for the horizontal direction. Concerning the vertical component, a better match is obtained. The computed soil response demonstrates that the device should measure the ground motion outside of the low insertion loss cone to improve the comparison of the results, where both bending modes are activated and the trench effect is more evident.

The second part of the thesis focuses on the development and assessment of the metawedge for railway induced ground vibrations. Both 2D and 2.5D models are adopted for the study. By means of the so-called wave-mode conversion mechanism, the proposed mitigation measure is able to convert the incoming surface waves into body waves exploiting the non-conventional dispersion properties of the resonators array. This wave redirection phenomenon generates at the surface level a successful vibration reduction for the frequency range mainly excited by the cargo train passage ($5 - 10\,\mathrm{Hz}$). Concerning the metawedge performance in the three-dimensional space, it generates positive insertion loss values in the above-mentioned conical region where the stiff trench does not.

The influence of the resonator dimensions and materials on the dispersion relations is investigated. An increase in width or height leads to a larger mass that lowers the longitudinal natural frequency of the resonator. This results in a better mitigation performance of the metawedge at lower frequencies. The same result is achieved if the metawedge is embedded in softer soil, i.e., smaller Young's modulus for the elastic medium. On the other hand, the Young's modulus of the resonator material does not significantly affect the dispersion curves.

The metawedge solution represents a possible alternative to the usual mitigation measures that are typically adopted on the transmission path. However, further research should be carried out to develop competitive solutions with a practical engineering relevance, the effort should focus on the design of feasible and compact systems.

The complementary performance of the two different mitigation measures highlights how a hybrid solution could lead to nearly complete vibration mitigation at the surface. Indeed, the stiffness effect could act where the wave-mode conversion mechanism does not appear effective.

## Further development

The following recommendations for further development come to light from the analyses and discussions presented in this work.

Concerning the in-situ test with a non-moving excitation source, an additional measurement setup is recommended when the performance of a stiff trench must be detected. The available devices should be arranged in parallel to the trench, in order to measure the soil response where the trench effect is more evident. This means measuring the response outside of the conical region, so where the stiff trench appears more effective. In this way, the ground motion is recorded behind the trench at different longitudinal distances from the point load. Furthermore, the developed model should be as detailed as possible to reach a better match with the field measurements, being more similar to the in-situ test scenario.

With respect to the numerical simulation, the implementation of a moving cargo train in the 2.5D model would allow an interesting assessment of the countermeasures performance. The track should also be considered, to evaluate the possible effects generated by its presence. A better understanding and interpretation of the mitigation mechanisms could be achieved with this type of simulation. The contribution of all the incoming waves with different incident angles is considered through the introduction of a moving load. For the metawedge, the investigation of the influence of different propagation angles is particularly interesting because its vibration mitigation seems to strongly depend on this variable.

The results obtained with the metawedge for the railway application suggest that this mitigation measure could represent an effective alternative to the usually installed ones. Further research is recommended to design more compact and practically feasible solutions. To keep the resonators straight and to prevent settling, the presence of foundations - neglected in the considered analysis - should also be implemented in the model. More complex resonators could also be evaluated to combine the advantageous effects of the stiff trench and metawedge. Their complementary performances could merge into a single system that is able to combine both the mitigation mechanisms (stiffness effect and wave-mode conversion). For this purpose, a metawedge composed of resonating stiff trenches could guarantee an effective mitigation result. Moreover, the possibility to attenuate both ground vibration and noise emission could be taken into account during the study. In this way, the annoyance of nearby residents would be alleviated from both noise and vibration transmission.

The effect of the wave-mode conversion mechanism in a layered half-space should be analysed. The waves could reach the surface behind the metawedge from the bottom, being reflected back by the stratified ground. This phenomenon should be carefully considered for a real application since the wave reflection could badly affect the obtained beneficial vibration attenuation at the surface level.

# Bibliography

[1] D. Thompson. Railway noise and vibration: The use of appropriate models to solve practical problems. *21st International Congress on Sound and Vibration 2014, ICSV 2014*, 1:17–32, January 2014.

[2] E. Peris, J. Woodcock, G. Sica, A. T. Moorhouse, and D. C. Waddington. Annoyance due to railway vibration at different times of the day. *The Journal of the Acoustical Society of America*, 131(2):EL191–EL196, feb 2012. doi: 10.1121/1.3679390.

[3] J. Jones. Low Frequency Ground Vibration. In D.J. Thompson, editor, *Railway Noise and Vibration: Mechanisms, Modelling and Means of Control*, pages 399–433. Elsevier, 2008.

[4] Geologische Dienst Nederland. Ondergrondgegevens. https://www.dinoloket.nl/ondergrondgegevens. Accessed: 29-01-2022.

[5] H.V.C. Howarth and M.J. Griffin. Human response to simulated intermittent railway-induced building vibration. *Journal of Sound and Vibration*, 120(2):413–420, jan 1988. doi: 10.1016/0022-460x(88)90453-1.

[6] Michael G. Smith, Ilona Croy, Mikael Ögren, and Kerstin Persson Waye. On the Influence of Freight Trains on Humans: A Laboratory Investigation of the Impact of Nocturnal Low Frequency Vibration and Noise on Sleep and Heart Rate. *PLoS ONE*, 8(2):e55829, feb 2013. doi: 10.1371/journal.pone.0055829.

[7] D. J. Thompson, J. Jiang, M. G. R. Toward, M. F. M. Hussein, E. Ntotsios, A. Dijckmans, P. Coulier, G. Lombaert, and G. Degrande. Reducing railway-induced ground-borne vibration by using open trenches and soft-filled barriers. *Soil Dynamics and Earthquake Engineering*, 88:45–59, sep 2016. doi: 10.1016/j.soildyn.2016.05.009.

[8] C. Van Hoorickx. *Design of vibration reduction measures for railway traffic by means of topology optimization*. PhD thesis, Katholieke Universiteit Leuven, 2017.

[9] P. Coulier, S. François, G. Degrande, and G. Lombaert. Subgrade stiffening next to the track as a wave impeding barrier for railway induced vibrations. *Soil Dynamics*

*and Earthquake Engineering*, 48:119–131, may 2013. doi: 10.1016/j.soildyn.2012.12.009.

[10] P. Coulier, S. François, G. Degrande, and G. Lombaert. A NUMERICAL STUDY OF SUBGRADE STIFFENING AS A MITIGATION MEASURE FOR RAILWAY INDUCED VIBRATIONS THROUGH 2.5D AND 3D FE-BE MODELS. In *Proceedings of the 4th International Conference on Computational Methods in Structural Dynamics and Earthquake Engineering (COMPDYN 2013)*. Institute of Structural Analysis and Antiseismic Research School of Civil Engineering National Technical University of Athens (NTUA) Greece, 2014. doi: 10.7712/120113.4535.c1414.

[11] H. Takemiya and A. Fujiwara. Wave propagation/impediment in a stratum and wave impeding block (WIB) measured for SSI response reduction. *Soil Dynamics and Earthquake Engineering*, 13(1):49–61, jan 1994. doi: 10.1016/0267-7261(94)90041-8.

[12] A. Dijckmans, A. Ekblad, A. Smekal, G. Degrande, and G. Lombaert. A SHEET PILING WALL AS A WAVE BARRIER FOR TRAIN INDUCED VIBRATIONS. In *Proceedings of the 4th International Conference on Computational Methods in Structural Dynamics and Earthquake Engineering (COMPDYN 2013)*. Institute of Structural Analysis and Antiseismic Research School of Civil Engineering National Technical University of Athens (NTUA) Greece, 2014. doi: 10.7712/120113.4534.c1303.

[13] A. Dijckmans, A. Ekblad, A. Smekal, G. Degrande, and G. Lombaert. Efficacy of a sheet pile wall as a wave barrier for railway induced ground vibration. *Soil Dynamics and Earthquake Engineering*, 84:55–69, may 2016. doi: 10.1016/j.soildyn.2016.02.001.

[14] A. Dijckmans, P. Coulier, J. Jiang, M. G. R. Toward, D.J. Thompson, G. Degrande, and G. Lombaert. Mitigation of railway induced ground vibration by heavy masses next to the track. *Soil Dynamics and Earthquake Engineering*, 75:158–170, aug 2015. doi: 10.1016/j.soildyn.2015.04.003.

[15] V.V. Krylov. Scattering of Rayleigh waves by heavy masses as method of protection against traffic-induced ground vibrations. In *Environmental Vibrations: Prediction, Monitoring, Mitigation and Evaluation (ISEV 2005)*, pages 393–398. CRC Press, jun 2021. doi: 10.1201/9781003209379-60.

[16] Mariana Valente Tuler and Sakdirat Kaewunruen. Life cycle analysis of mitigation methodologies for railway rolling noise and groundbourne vibration. *Journal of Environmental Management*, 191:75–82, apr 2017. doi: 10.1016/j.jenvman.2016.12.075.

[17] J. Barbosa. *ANALYSIS AND MITIGATION OF VIBRATIONS INDUCED BY*

*THE PASSAGE OF HIGH-SPEED TRAINS IN NEARBY BUILDINGS*. PhD thesis, University of Porto, 2013.

[18] D. P. Connolly, G. P. Marecki, G. Kouroussis, I. Thalassinakis, and P. K. Woodward. The growth of railway ground vibration problems — a review. *Science of The Total Environment*, 568:1276–1282, oct 2016. doi: 10.1016/j.scitotenv.2015.09.101.

[19] A. Karlström and A. Boström. Efficiency of trenches along railways for trains moving at sub- or supersonic speeds. *Soil Dynamics and Earthquake Engineering*, 27(7):625–641, jul 2007. doi: 10.1016/j.soildyn.2006.12.005.

[20] S. François, M. Schevenels, B. Thyssen, J. Borgions, and G. Degrande. Design and efficiency of a composite vibration isolating screen in soil. *Soil Dynamics and Earthquake Engineering*, 39:113–127, aug 2012. doi: 10.1016/j.soildyn.2012.03.007.

[21] D. E. Beskos, B. DasGupta, and I. G. Vardoulakis. Vibration isolation using open or filled trenches. *Computational Mechanics*, 1(1):43–63, mar 1986. doi: 10.1007/bf00298637.

[22] Y. B. Yang and H. H. Hung. A PARAMETRIC STUDY OF WAVE BARRIERS FOR REDUCTION OF TRAIN-INDUCED VIBRATIONS. *International Journal for Numerical Methods in Engineering*, 40(20):3729–3747, oct 1997. doi: 10.1002/(sici)1097-0207(19971030)40:20<3729::aid-nme236>3.0.co;2-8.

[23] S. François, M. Schevenels, P. Galvín, G. Lombaert, and G. Degrande. A 2.5D coupled FE–BE methodology for the dynamic interaction between longitudinally invariant structures and a layered halfspace. *Computer Methods in Applied Mechanics and Engineering*, 199(23-24):1536–1548, apr 2010. doi: 10.1016/j.cma.2010.01.001.

[24] J. Jiang, M. G. R. Toward, A. Dijckmans, D. J. Thompson, G. Degrande, G. Lombaert, and J. Ryue. Reducing railway induced ground-borne vibration by using trenches and buried soft barriers. In *Notes on Numerical Fluid Mechanics and Multidisciplinary Design*, pages 555–562. Springer Berlin Heidelberg, 2015. doi: 10.1007/978-3-662-44832-8_65.

[25] S. Ahmad and T. M. Al-Hussaini. Simplified Design for Vibration Screening by Open and In-Filled Trenches. *Journal of Geotechnical Engineering*, 117(1):67–88, jan 1991. doi: 10.1061/(asce)0733-9410(1991)117:1(67).

[26] L. Andersen and S.R.K. Nielsen. Reduction of ground vibration by means of barriers or soil improvement along a railway track. *Soil Dynamics and Earthquake Engineering*, 25(7-10):701–716, aug 2005. doi: 10.1016/j.soildyn.2005.04.007.

[27] P. Coulier, V. Cuéllar, G. Degrande, and G. Lombaert. Experimental and numerical evaluation of the effectiveness of a stiff wave barrier in the soil. *Soil Dynamics and Earthquake Engineering*, 77:238–253, oct 2015. doi: 10.1016/j.soildyn.2015.04.007.

[28] P. Coulier, A. Dijckmans, S. François, G. Degrande, and G. Lombaert. A spatial windowing technique to account for finite dimensions in 2.5D dynamic soil–structure interaction problems. *Soil Dynamics and Earthquake Engineering*, 59:51–67, apr 2014. doi: 10.1016/j.soildyn.2014.01.006.

[29] C. Van Hoorickx, M. Schevenels, and G. Lombaert. Double wall barriers for the reduction of ground vibration transmission. *Soil Dynamics and Earthquake Engineering*, 97:1–13, jun 2017. doi: 10.1016/j.soildyn.2017.02.006.

[30] A. Colombi, P. Roux, S. Guenneau, P. Gueguen, and R. V. Craster. Forests as a natural seismic metamaterial: Rayleigh wave bandgaps induced by local resonances. *Scientific Reports*, 6(1), jan 2016. doi: 10.1038/srep19238.

[31] A. Colombi, D. Colquitt, P. Roux, S. Guenneau, and R.V. Craster. A seismic metamaterial: The resonant metawedge. *Scientific Reports*, 6(1), jun 2016. doi: 10.1038/srep27717.

[32] Muhammad, Tingkai Wu, and C. W. Lim. Forest Trees as Naturally Available Seismic Metamaterials: Low Frequency Rayleigh Wave with Extremely Wide Bandgaps. *International Journal of Structural Stability and Dynamics*, 20(14):2043014, dec 2020. doi: 10.1142/s0219455420430142.

[33] Muhammad and C. W. Lim. Natural seismic metamaterials: the role of tree branches in the birth of Rayleigh wave bandgap for ground born vibration attenuation. *Trees*, 35(4):1299–1315, mar 2021. doi: 10.1007/s00468-021-02117-8.

[34] Z. Liu, K. Qin, and G. Yu. Partially Embedded Gradient Metabarrier: Broadband Shielding from Seismic Rayleigh Waves at Ultralow Frequencies. *Journal of Engineering Mechanics*, 146(5):04020032, may 2020. doi: 10.1061/(asce)em.1943-7889.0001752.

[35] A. Palermo, S. Krödel, A. Marzani, and C. Daraio. Engineered metabarrier as shield from seismic surface waves. *Scientific Reports*, 6(1), dec 2016. doi: 10.1038/srep39356.

[36] A. Palermo, M. Vitali, and A. Marzani. Metabarriers with multi-mass locally resonating units for broad band Rayleigh waves attenuation. *Soil Dynamics and Earthquake Engineering*, 113:265–277, oct 2018. doi: 10.1016/j.soildyn.2018.05.035.

[37] Muhammad, C.W. Lim, and Krzysztof Kamil Żur. Wide Rayleigh waves bandgap engineered metabarriers for ground born vibration attenuation. *Engineering Structures*, 246:113019, nov 2021. doi: 10.1016/j.engstruct.2021.113019.

[38] Muhammad and C. W. Lim. From Photonic Crystals to Seismic Metamaterials: A Review via Phononic Crystals and Acoustic Metamaterials. *Archives of Computational Methods in Engineering*, 29(2):1137–1198, jun 2021. doi: 10.1007/s11831-021-09612-8.

[39] 3D berekeningen alternatief ontwerp TROC, Spooromgeving Geldermalsen. Technical Report CC-REP20190701, Cohere Consultants, July 2019.

[40] Karl F. Graff. *Wave Motion in Elastic Solids.* DOVER PUBN INC, June 1991. ISBN 0486667456. URL `https://www.ebook.de/de/product/1934736/karl_f_graff_wave_motion_in_elastic_solids.html`.

[41] J. D. Achenbach. *Wave propagation in elastic solids.* North-Holland Pub. Co.American Elsevier Pub. Co, Amsterdam,New York, 1973. ISBN 9780720403251.

[42] Chongbin Zhao. *Dynamic and Transient Infinite Elements.* Springer Berlin Heidelberg, August 2016. ISBN 3662502399. URL `https://www.ebook.de/de/product/29901395/chongbin_zhao_dynamic_and_transient_infinite_elements.html`.

[43] C. Cornejo Córdova. *Elastodynamics with Hysteretic Damping.* DUP Science, Delft, Netherlands, 2002. ISBN 9040723036.

[44] P. Morse and H. Feshbach. *Methods of theoretical physics.* McGraw-Hill, New York, 1953. ISBN 9780070433168.

[45] Michael A. Slawinski. *Waves and Rays in Elastic Continua.* World Scientific Publishing Company, September 2010. ISBN 9814289000. URL `https://www.ebook.de/de/product/10408256/michael_a_slawinski_waves_and_rays_in_elastic_continua.html`.

[46] K. N. van Dalen. *Soil Dynamics, part B: Body waves in an elastic continuum & Rayleigh waves at the free surface.* June 2015. Lecture notes CIE5340.

[47] Cornelis Wapenaar. *Elastic wave field extrapolation.* Elsevier, City, 1989. ISBN 0444884726.

[48] Larry Lake. *Petroleum engineering handbook.* Society of Petroleum Engineers, Richardson, TX, 2006. ISBN 9781555631208.

[49] Lord Rayleigh. On Waves Propagated along the Plane Surface of an Elastic Solid.

*Proceedings of the London Mathematical Society*, s1-17(1):4–11, nov 1885. doi: 10.1112/plms/s1-17.1.4.

[50] H. H. Hung Y. B. Yang. *Wave Propagation for Train-Induced Vibrations.* World Scientific Publishing Company, June 2009. ISBN 9812835822. URL `https://www.ebook.de/de/product/8581362/y_b_yang_h_h_hung_wave_propagation_for_train_induced_vibrations.html`.

[51] H. Lamb. On the propagation of tremors over the surface of an elastic solid. *Proceedings of the Royal Society of London*, 72(477-486):128–130, jan 1904. doi: 10.1098/rspl.1903.0029.

[52] J. Barbosa, P. A. Costa, and R. Calçada. Abatement of railway induced vibrations: Numerical comparison of trench solutions. *Engineering Analysis with Boundary Elements*, 55:122–139, jun 2015. doi: 10.1016/j.enganabound.2014.11.029.

[53] Eduardo Kausel. *Fundamental Solutions in Elastodynamics.* Cambridge University Press, May 2006. ISBN 0521855705. URL `https://www.ebook.de/de/product/5148751/eduardo_kausel_fundamental_solutions_in_elastodynamics.html`.

[54] Granino Korn. *Mathematical handbook for scientists and engineers; definitions, theorems, and formulas for reference and review.* McGraw-Hill, New York, 1968. ISBN 9780070353701.

[55] William Ewing. *Elastic waves in layered media.* McGraw-Hill, New York, 1957. ISBN 9780070198609.

[56] TRILLINGSMETINGEN EFFECTIVITEIT TROC, Spooromgeving Geldermalsen. Technical Report CC-REP20200501, Cohere Consultants, May 2020.

[57] H. Verbraken, H. Eysermans, E. Dechief, S. François, G. Lombaert, and G. Degrande. Verification of an Empirical Prediction Method for Railway Induced Vibration. In *Notes on Numerical Fluid Mechanics and Multidisciplinary Design*, pages 239–247. Springer Japan, 2012. doi: 10.1007/978-4-431-53927-8_28.

[58] G. Lombaert, G. Degrande, J. Kogut, and S. François. The experimental validation of a numerical model for the prediction of railway induced vibrations. *Journal of Sound and Vibration*, 297(3-5):512–535, nov 2006. doi: 10.1016/j.jsv.2006.03.048.

[59] H. H. Hung, Y. B. Yang, and D. W. Chang. Wave Barriers for Reduction of Train-Induced Vibrations in Soils. *Journal of Geotechnical and Geoenvironmental Engineering*, 130(12):1283–1291, dec 2004. doi: 10.1061/(asce)1090-0241(2004)130:12(1283).

[60] Eduardo Kausel. Early history of soil–structure interaction. *Soil Dynamics and Earthquake Engineering*, 30(9):822–832, sep 2010. doi: 10.1016/j.soildyn.2009.11.001.

[61] J. Jones. Ground-borne Noise. In D.J. Thompson, editor, *Railway Noise and Vibration: Mechanisms, Modelling and Means of Control*, pages 437–464. Elsevier, 2008.

[62] S. François, M. Schevenels, G. Lombaert, and G. Degrande. A two-and-a-half-dimensional displacement-based PML for elastodynamic wave propagation. *International Journal for Numerical Methods in Engineering*, 90(7):819–837, dec 2011. doi: 10.1002/nme.3344.

[63] J. Jiang, M. Toward, A. Dijckmans, D. Thompson, G. Degrande, G. Lombaert, and M. Hussein. THE INFLUENCE OF SOIL CONDITIONS ON RAILWAYINDUCED GROUND-BORNE VIBRATION AND RELE-VANT MITIGATION MEASURES. In *21st International Congress on Sound and Vibration 2014, ICSV 2014*, volume 4, January 2014.

[64] João Manuel de Oliveira Barbosa, Joonsang Park, and Eduardo Kausel. Perfectly matched layers in the thin layer method. *Computer Methods in Applied Mechanics and Engineering*, 217-220:262–274, apr 2012. doi: 10.1016/j.cma.2011.12.006.

[65] Steven G. Johnson. Notes on perfectly matched layers (pmls). August 2021.

[66] Richard D. Woods. Screening of Surface Wave in Soils. *Journal of the Soil Mechanics and Foundations Division*, 94(4):951–979, apr 1968. doi: 10.1061/jsfeaq.0001180.

[67] S.P. Timoshenko. On the transverse vibrations of bars of uniform cross-section. *The London, Edinburgh, and Dublin Philosophical Magazine and Journal of Science*, 43 (253):125–131, jan 1922. doi: 10.1080/14786442208633855.

[68] G. R. Cowper. The Shear Coefficient in Timoshenko's Beam Theory. *Journal of Applied Mechanics*, 33(2):335–340, jun 1966. doi: 10.1115/1.3625046.

[69] P. Hagedorn and A. DasGupta. Vibrations and Waves in Continuous Mechanical Systems. pages 113–178. John Wiley & Sons, Ltd, oct 2007. doi: 10.1002/9780470518434.ch3.

[70] S.P. Timoshenko. On the correction for shear of the differential equation for transverse vibrations of prismatic bars. *The London, Edinburgh, and Dublin Philosophical Magazine and Journal of Science*, 41(245):744–746, may 1921. doi: 10.1080/14786442108636264.

[71] Roberto Corradi. Lecture notes in Noise and Vibration Engineering. Department of Mechanical Engineering of Politecnico di Milano, 2021.

[72] Sudhish Kumar Bakku, Anbazhagan Panjamani, and Sitharam Thallak. DEVELOPMENT OF THEORETICAL DISPERSION CURVES AND COMPARISON WITH MULTICHANNEL ANALYSIS OF SURFACE WAVES (MASW). December 2006.

[73] Nadège Kaina, Mathias Fink, and Geoffroy Lerosey. Composite media mixing Bragg and local resonances for highly attenuating and broad bandgaps. *Scientific Reports*, 3(1), nov 2013. doi: 10.1038/srep03240.

[74] Agnès Maurel, Jean-Jacques Marigo, Kim Pham, and Sébastien Guenneau. Conversion of Love waves in a forest of trees. *Physical Review B*, 98(13):134311, oct 2018. doi: 10.1103/physrevb.98.134311.

[75] H. W. Huang, J. Wang, C. Zhao, and Y. L. Mo. Two-Dimensional Finite-Element Simulation of Periodic Barriers. *Journal of Engineering Mechanics*, 147(2):04020150, feb 2021. doi: 10.1061/(asce)em.1943-7889.0001891.

[76] L. Brillouin. *Wave Propagation in Periodic Structures.* Dover Publications, New York, second edition, 1953. ISBN 0486600343.

[77] Douglas R. Hofstadter. Energy levels and wave functions of Bloch electrons in rational and irrational magnetic fields. *Physical Review B*, 14(6):2239–2249, sep 1976. doi: 10.1103/physrevb.14.2239.

[78] X. Pu, Z. Shi, and H. Xiang. Feasibility of ambient vibration screening by periodic geofoam-filled trenches. *Soil Dynamics and Earthquake Engineering*, 104:228–235, jan 2018. doi: 10.1016/j.soildyn.2017.10.022.

[79] J. Huang, W. Liu, and Z. Shi. Surface-wave attenuation zone of layered periodic structures and feasible application in ground vibration reduction. *Construction and Building Materials*, 141:1–11, jun 2017. doi: 10.1016/j.conbuildmat.2017.02.153.

[80] M. Badreddine Assouar and Mourad Oudich. Dispersion curves of surface acoustic waves in a two-dimensional phononic crystal. *Applied Physics Letters*, 99(12):123505, sep 2011. doi: 10.1063/1.3626853.

[81] *COMSOL Multiphysics Reference Manual, version 5.4.* Comsol Inc, 2018.

[82] Xingbo Pu and Zhifei Shi. A novel method for identifying surface waves in periodic structures. *Soil Dynamics and Earthquake Engineering*, 98:67–71, jul 2017. doi: 10.1016/j.soildyn.2017.04.011.

[83] Matthieu Rupin, Fabrice Lemoult, Geoffroy Lerosey, and Philippe Roux. Experimental Demonstration of Ordered and Disordered Multiresonant metamaterials for lamb waves. *Physical Review Letters*, 112(23):234301, jun 2014. doi: 10.1103/physrevlett.112.234301.

[84] S. Benchabane, A. Khelif, J.-Y. Rauch, L. Robert, and V. Laude. Evidence for complete surface wave band gap in a piezoelectric phononic crystal. *Physical Review E*, 73(6):065601, jun 2006. doi: 10.1103/physreve.73.065601.

[85] Zhengyou Liu, Xixiang Zhang, Yiwei Mao, Y. Y. Zhu, Zhiyu Yang, C. T. Chan, and Ping Sheng. Locally Resonant Sonic Materials. *Science*, 289(5485):1734–1736, sep 2000. doi: 10.1126/science.289.5485.1734.

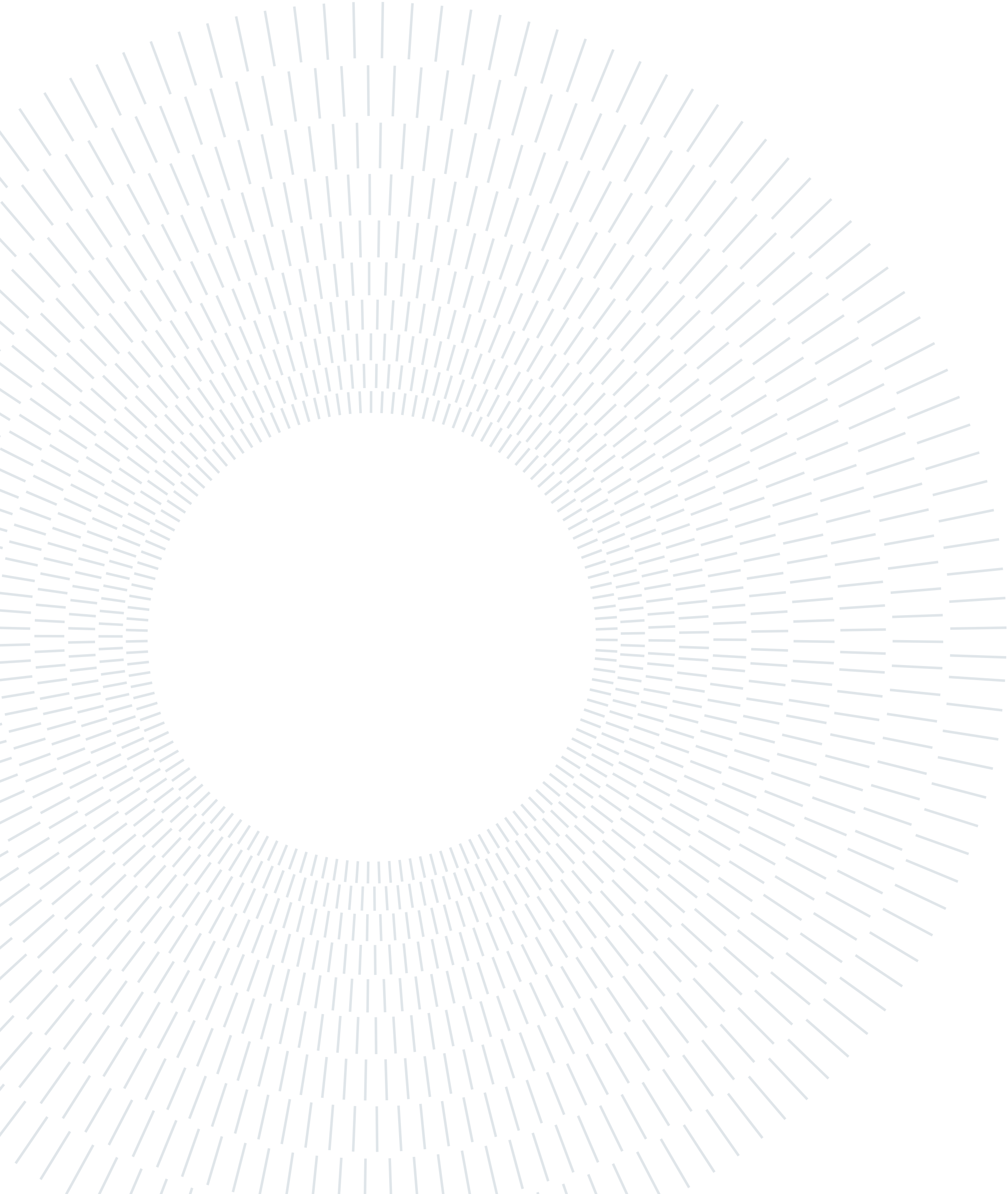

# Appendix

## Soil properties - Chapter 1

The soil properties employed in Chapter 1 are provided in Table 1. For the homogeneous case analysed in Section 1.2.1 the second layer is selected, while for the single layer case the first layer is settled. The depth $L$ is always chosen equal to 10 m.

Table 1: Soil properties

| Layer | $\rho\,(\mathrm{kg/m^3})$ | $\lambda\,(\mathrm{N/m^2})$ | $\mu\,(\mathrm{N/m^2})$ | *Depth* (m) |
|---|---|---|---|---|
| 1 | 1622 | $2.24 \cdot 10^8$ | $1.12 \cdot 10^8$ | 10 |
| 2 | 1827 | $2.24 \cdot 10^9$ | $1.12 \cdot 10^9$ | $\infty$ |

## Lamb's problem ground displacements

The displacements of the surface that result from the Lamb's problem discussed in Section 1.2 are taken by [55] and rewritten in the following. It is reminded that a homogeneous half-space is investigated and that this is a non-dispersive medium characterized by constant $c_P$, $c_S$ and $c_R$. As already mentioned, this implies that the wavenumbers are linear functions of $\omega$, with $k_P = \omega/c_P$, $k_S = \omega/c_S$ and $k_R = \omega/c_R$.

$$
\begin{aligned}
u = \Bigg\{ & \frac{k_R\left(2k_R^2 - k_S^2 - 2\sqrt{k_R^2 - k_R^2}\sqrt{k_R^2 - k_S^2}\right)\mathrm{e}^{\mathrm{i}(\Omega t - k_R x)}}{\left(8\left(2k_R^2 - k_S^2\right)\right)k_R - 8k_R\sqrt{k_R^2 - k_P^2}\sqrt{k_R^2 - k_S^2} - 4k_R^3\frac{\sqrt{k_R^2 - k_S^2}}{\sqrt{k_R^2 - k_P^2}} - 4k_R^3\frac{\sqrt{k_R^2 - k_P^2}}{\sqrt{k_R^2 - k_S^2}}} \\
& + \sqrt{\frac{2}{\pi}}\sqrt{1 - \frac{k_P^2}{k_S^2}}\,\frac{\mathrm{e}^{\mathrm{i}\left(\Omega t - k_S x - \frac{\pi}{4}\right)}}{\left(k_S x\right)^{\frac{3}{2}}} \\
& - \sqrt{\frac{2}{\pi}}\,\frac{k_P^3 k_S^2\sqrt{k_S^2 - k_P^2}}{\left(k_S^2 - 2k_P^2\right)^3}\,\frac{\mathrm{i}\mathrm{e}^{\mathrm{i}\left(\Omega t - k_P x - \frac{\pi}{4}\right)}}{\left(k_P x\right)^{\frac{3}{2}}} + \dots \Bigg\}\frac{F_0}{\mu},
\end{aligned}
\tag{1}
$$

$$
\begin{aligned}
w = \Bigg\{ & \frac{-\mathrm{i}k_S^2\sqrt{k_R^2-k_P^2}\,\mathrm{e}^{\mathrm{i}(\Omega t-k_R x)}}{\left(8\left(2k_R^2-k_S^2\right)\right)k_R-8k_R\sqrt{k_R^2-k_P^2}\sqrt{k_R^2-k_S^2}-4k_R^3\frac{\sqrt{k_R^2-k_S^2}}{\sqrt{k_R^2-k_R^2}}-4k_R^3\frac{\sqrt{k_R^2-k_P^2}}{\sqrt{k_R^2-k_S^2}}} \\
& +2\sqrt{\frac{2}{\pi}}\left(1-\frac{k_P^2}{k_S^2}\right)\frac{\mathrm{i}\mathrm{e}^{\mathrm{i}\left(\Omega t-k_S x-\frac{1}{4}\pi\right)}}{\left(k_S x\right)^{\frac{3}{2}}} \\
& +\frac{1}{2}\sqrt{\frac{2}{\pi}}\frac{k_P^2k_S^2}{\left(k_S^2-2k_P^2\right)^2}\frac{i\mathrm{e}^{\mathrm{i}\left(\Omega t-k_P x-\frac{1}{4}\pi\right)}}{\left(k_P x\right)^{\frac{3}{2}}}+\ldots\Bigg\}\frac{F_0}{\mu},
\end{aligned}
\tag{2}
$$

where ... represents the higher order terms, which can be neglected for farther distance $x$ [50].

## Mean spectra train passage test

The mean spectra for the train passage in geophone A location before and after the trench construction are computed and depicted in Fig. A.1.

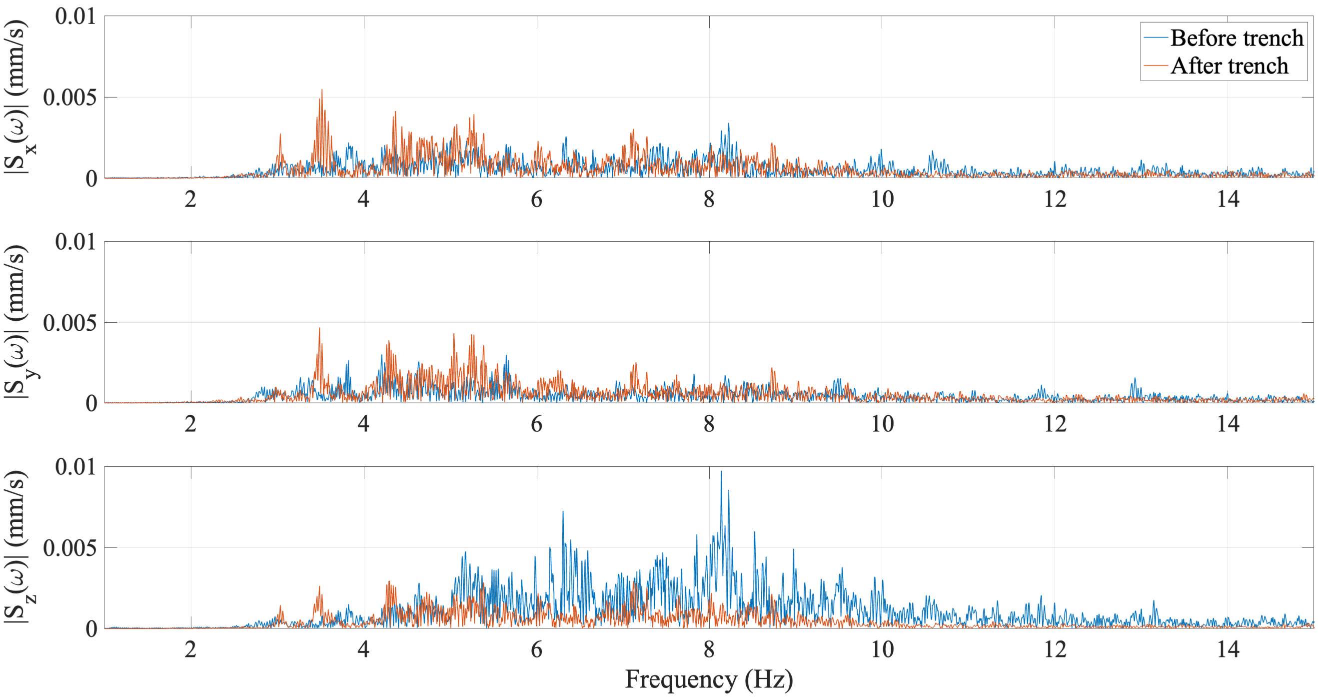

Figure A.1: Mean spectra in in geophone A location associated to the passages of cargo train before (blue) and after (orange) the trench construction.

It is evident that the amplitudes at very low frequencies (smaller than 2.5 Hz) are negligible with respect to the others. Moreover, to calculate the mean spectra amplitude Eq. (3) is used. Here, it is written for a generic group of signals $S(\omega)$, with $n_s$ members.

$$|S(\omega)| = |\frac{1}{n_s}\sum_{i=1}^{n_s} S_i(\omega)|. \tag{3}$$

## Dropping load test further results

In this section are provided additional results that are originated by the dropping load test. Fig. A.2 has the same outcomes as Fig. 2.7 plus the geophones IV and V.

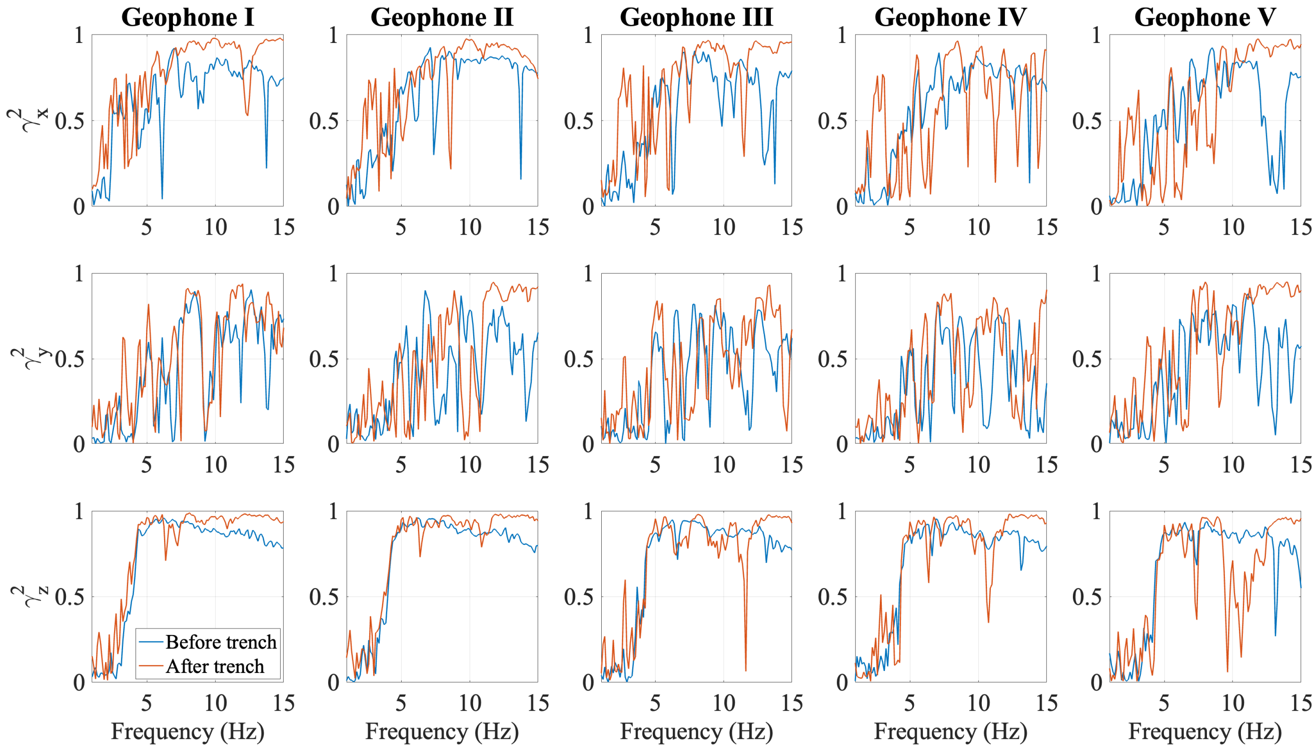

Figure A.2: Coherence computed in the dropping load test before (blue) and after (orange) the trench construction in the three directions for the five geophones placed in row.

Fig. A.3 has the same results as Fig. 2.8 plus the horizontal direction $y$ and the geophones IV and V.

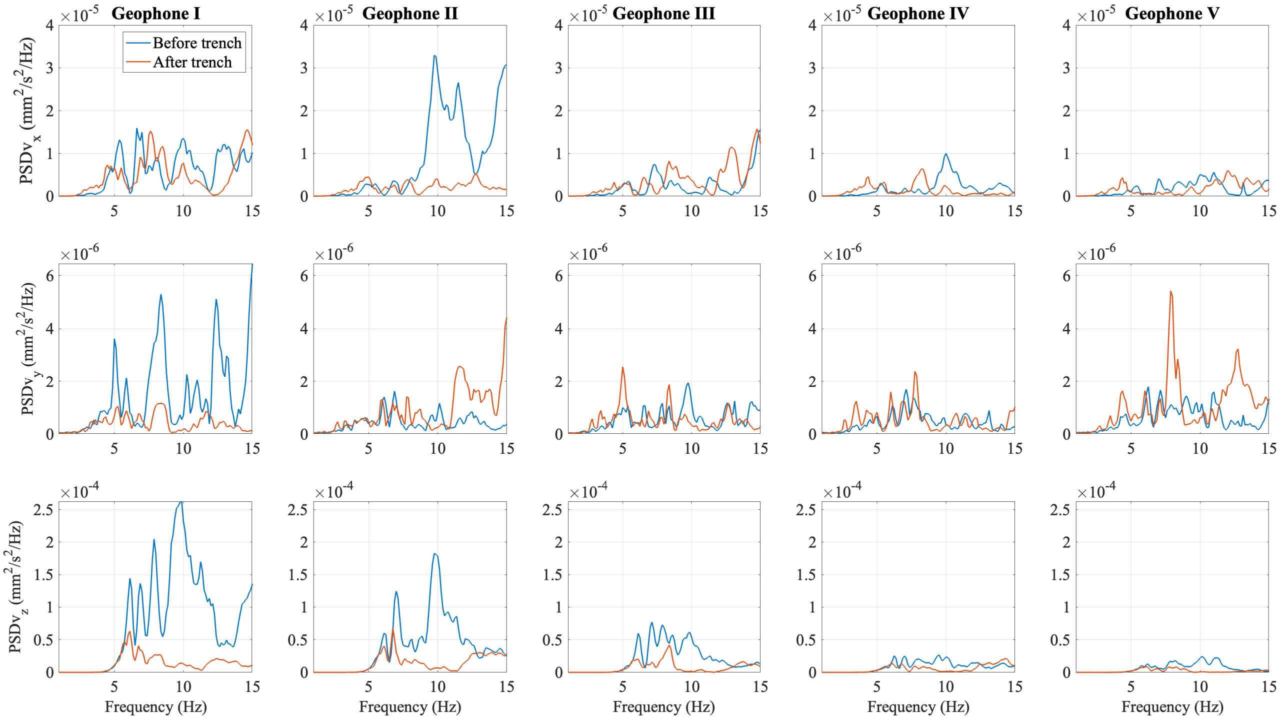

Figure A.3: Averaged PSD computed for the five geophones in the dropping load case before (blue) and after (orange) the trench construction.

The IL$_x$ and IL$_z$ are given for all the five measurement instruments in Fig. A.4.

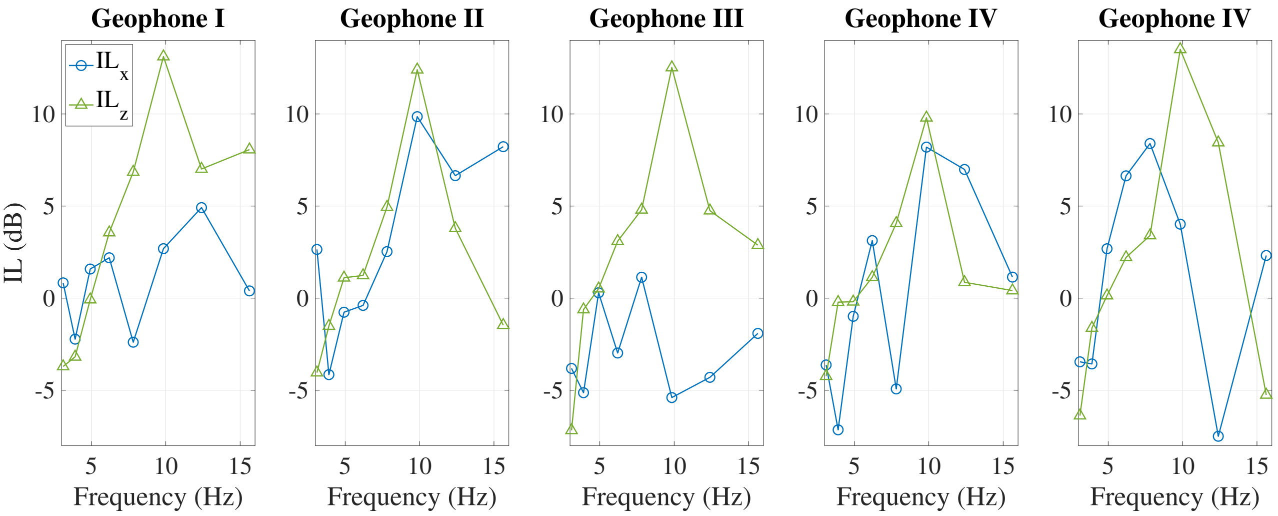

Figure A.4: Averaged PSD computed for the five geophones in the dropping load case before (blue) and after (orange) the trench construction.

## Trench and soil properties - Section 3.1.2

The wave in-filled trench and soil properties from [8] and adopted in Section 3.1.2 are listed in Table 2. Note that the trench is stiffer than the homogeneous half-space.

Table 2: In-filled trench and soil properties [8].

|  | $\rho\,(\mathrm{kg/m^3})$ | $E\,(\mathrm{MPa})$ | $\nu$ | $c_P\,(\mathrm{m/s})$ | $c_S\,(\mathrm{m/s})$ | $\xi_\mathrm{d}\,(\%)$ |
|---|---|---|---|---|---|---|
| Trench | 2000 | 1510 | 0.248 | 950 | 550 | 2.5 |
| Soil | 2000 | 213 | 0.333 | 400 | 200 | 2.5 |

## Homogeneous soil - Section 3.2

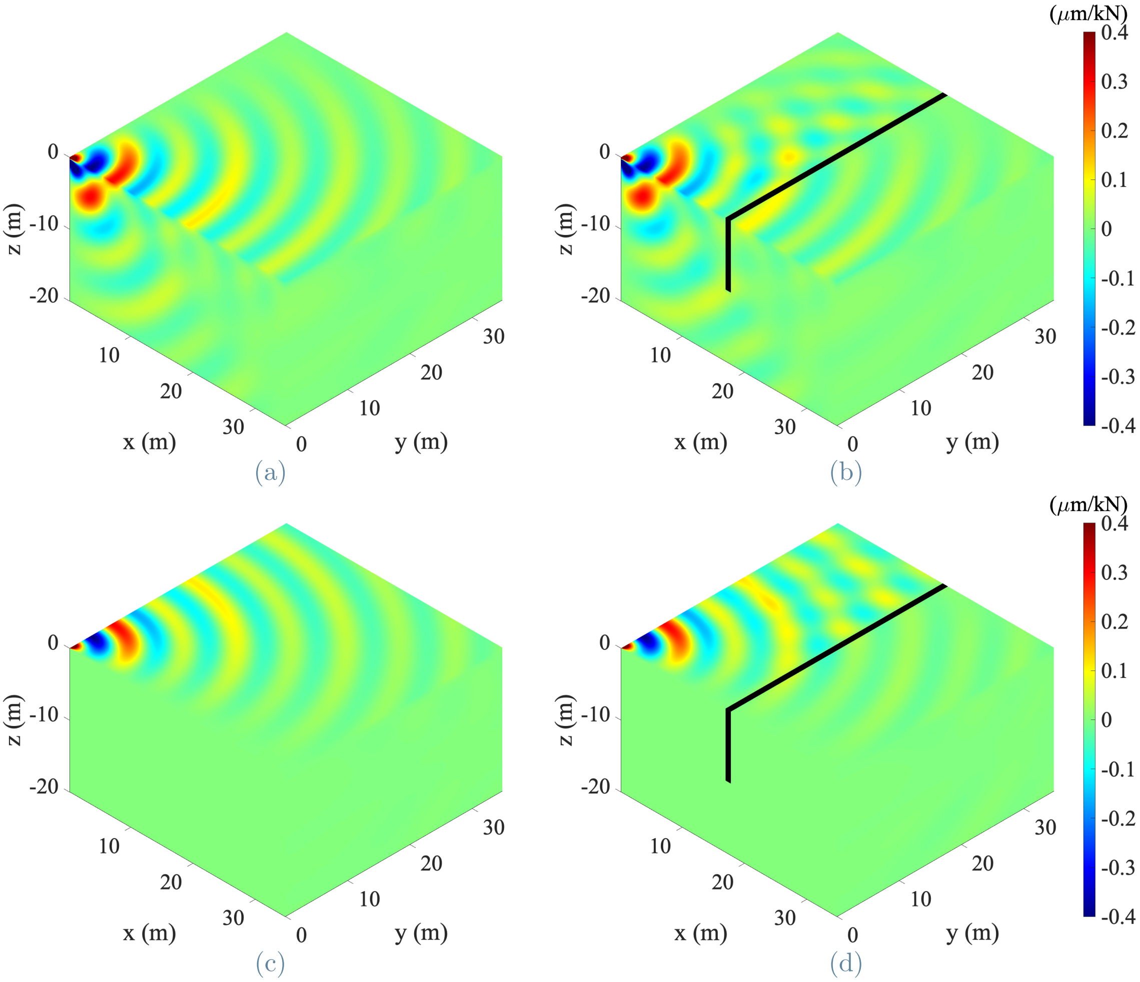

(a) (b)

(c) (d)

Figure A.5: Real part of horizontal displacement components generated by unit harmonic vertical point load with $\Omega = 2\pi \times 25\,\mathrm{Hz}$, $x$ direction (first row) $y$ one (second row). Homogeneous soil (first column) and stiff in-filled trench (second column).

The horizontal component of displacement is provided in Fig. A.5 for the case without (left column) and with (right column) the stiff in-filled trench. The first row refers to the $x$ direction, whereas the second one to the $y$ one.

If the excitation frequency is smaller than the critical one, the stiff in-filled trench results completely useless. It is not able to mitigate vibration. Computing the IL, it is nearly zero everywhere in the space. The case with $\Omega = 2\pi \times 1\,\mathrm{Hz}$ is shown in Fig. A.6 where green box plots arise.

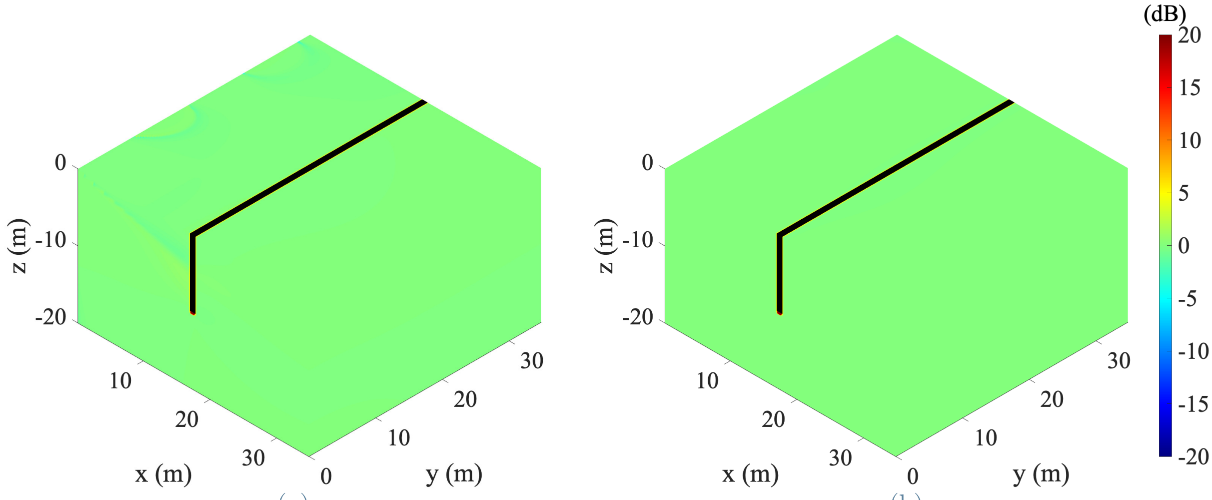

(a) (b)

Figure A.6: Insertion loss in the space-frequency domain: $\mathrm{IL}_x(x, y, z, \Omega = 2\pi \times 1\,\mathrm{Hz})$ (a) and $\mathrm{IL}_z(x, y, z, \Omega = 2\pi \times 1\,\mathrm{Hz})$ (b), where $\Omega = 2\pi \times 1\,\mathrm{Hz} < \omega_{c,x}$.

The $\mathrm{Re}(u_x(x, y, z, \Omega = 2\pi \times 50\,\mathrm{Hz}))$ is depicted in Fig. A.7, while the insertion loss for $\Omega = 2\pi \times 50\,\mathrm{Hz}$ computed with the displacement components along $x$ and $z$ are shown in Fig. A.8a and Fig. A.8b, respectively.

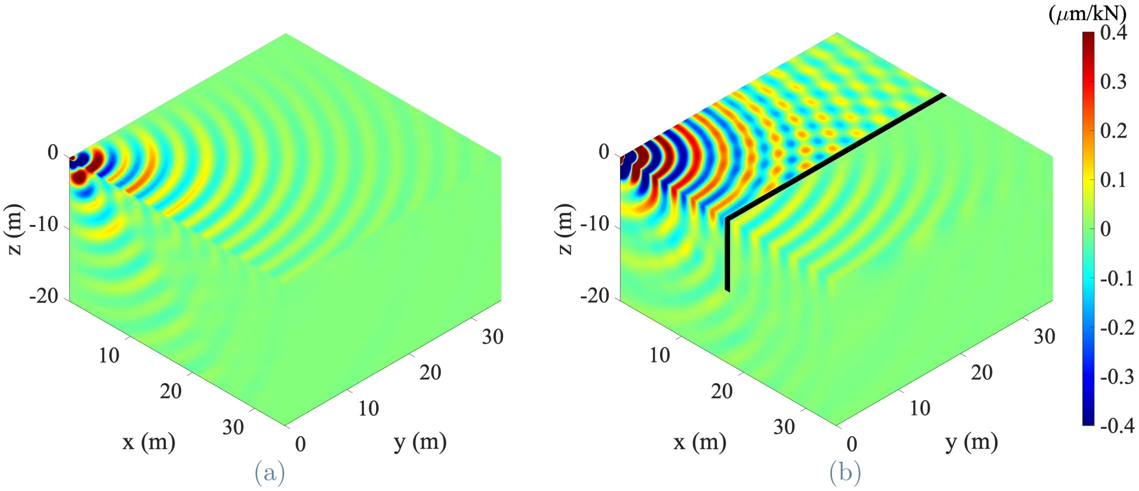

(a) (b)

Figure A.7: Real part of the horizontal displacement component $\mathrm{Re}(u_x(x, y, z, \Omega = 2\pi \times 50\,\mathrm{Hz}))$ generated by unit harmonic vertical point load. Homogeneous soil (a) and with in-filled trench (b).

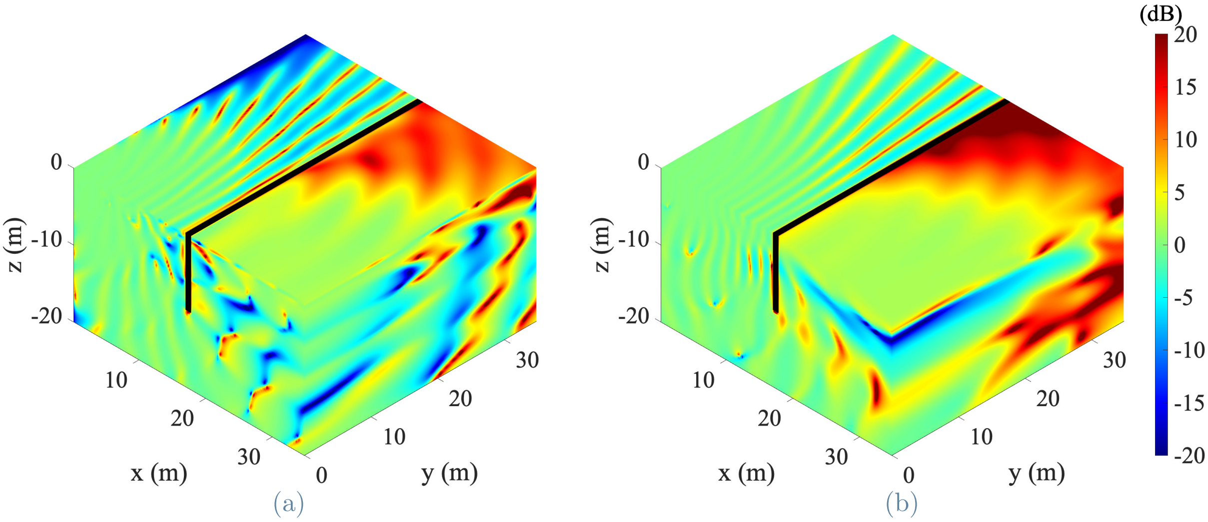

(a) (b)

Figure A.8: Insertion loss in the space-frequency domain: $\mathrm{IL}_x(x, y, z, \Omega = 2\pi \times 50\,\mathrm{Hz})$ (a) and $\mathrm{IL}_z(x, y, z, \Omega = 2\pi \times 50\,\mathrm{Hz})$ (b).

The three-dimensional plot of the vertical insertion loss in the space-wavenumber-frequency domain is given in Fig. A.9a for the softer soil case presented in Section 3.2.5. The analysed case with the stiffer in-filled trench is instead displayed in Fig. A.9b.

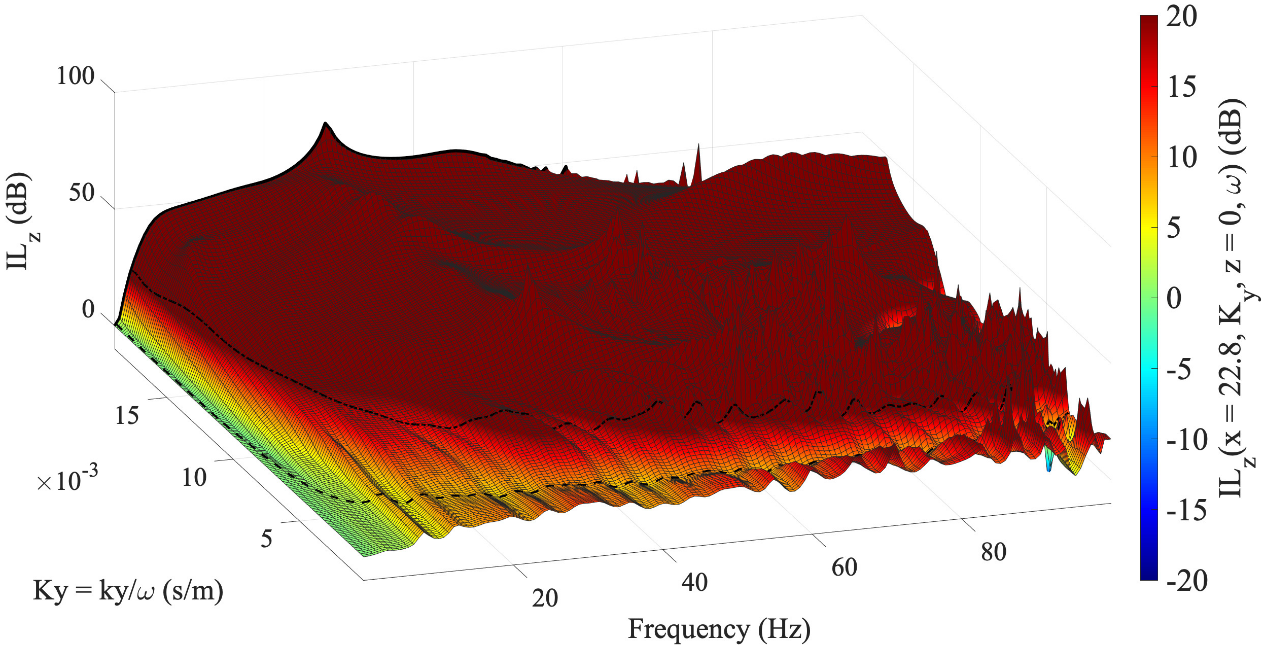

(a)

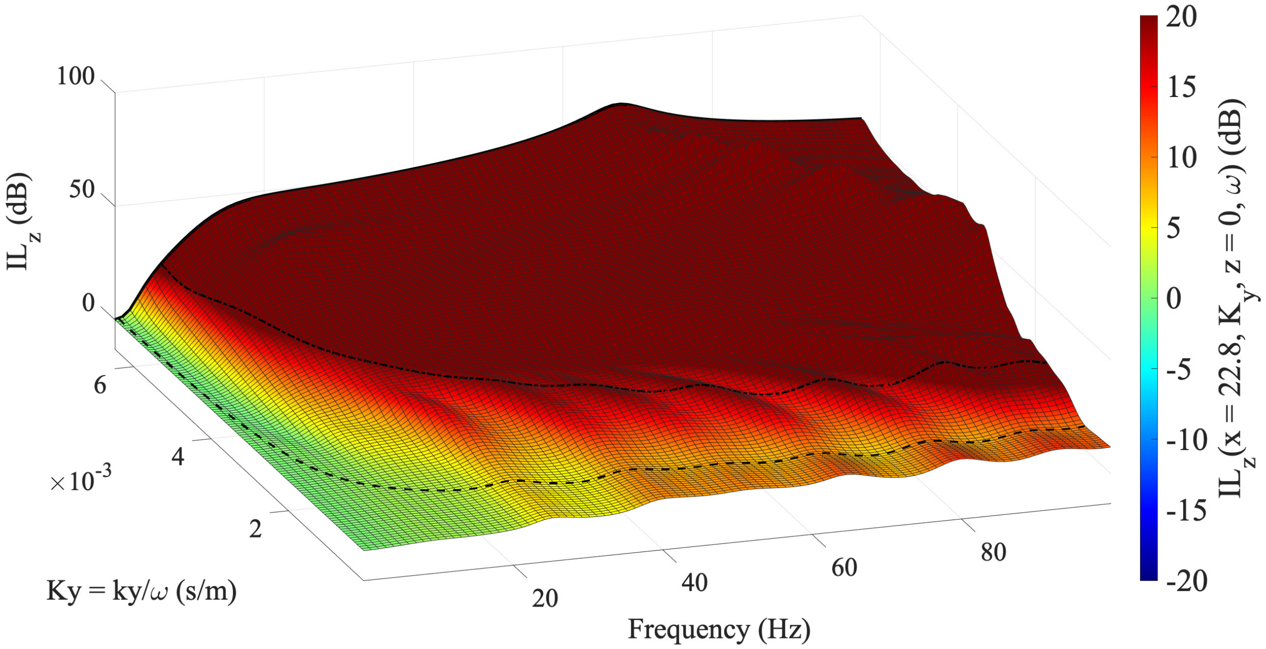

(b)

Figure A.9: Vertical insertion loss $\mathrm{IL}_z(x = 22.8, K_y, z = 0, \omega)$ for softer soil and reference trench (a) and for reference soil and stiffer trench (b). Refer to Fig. 3.6 for the description of the superimposed curves.

The IL$_x$ for the softer soil and stiffer trench case is shown in Fig. A.10a and Fig. A.10b, respectively. The comments in Section 3.2.5 apply to them.

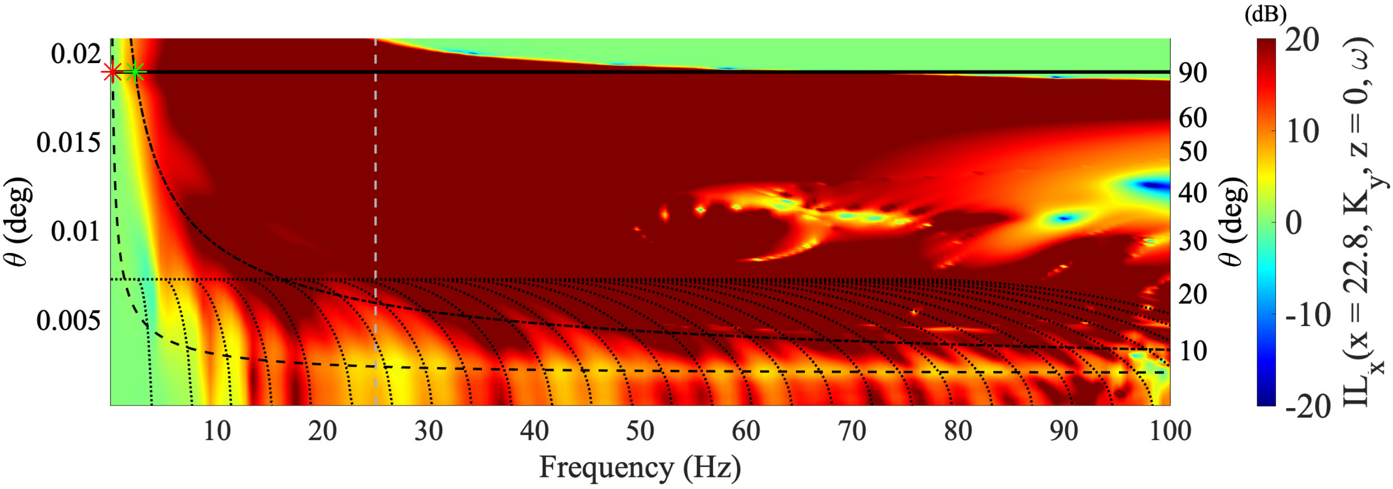

(a)

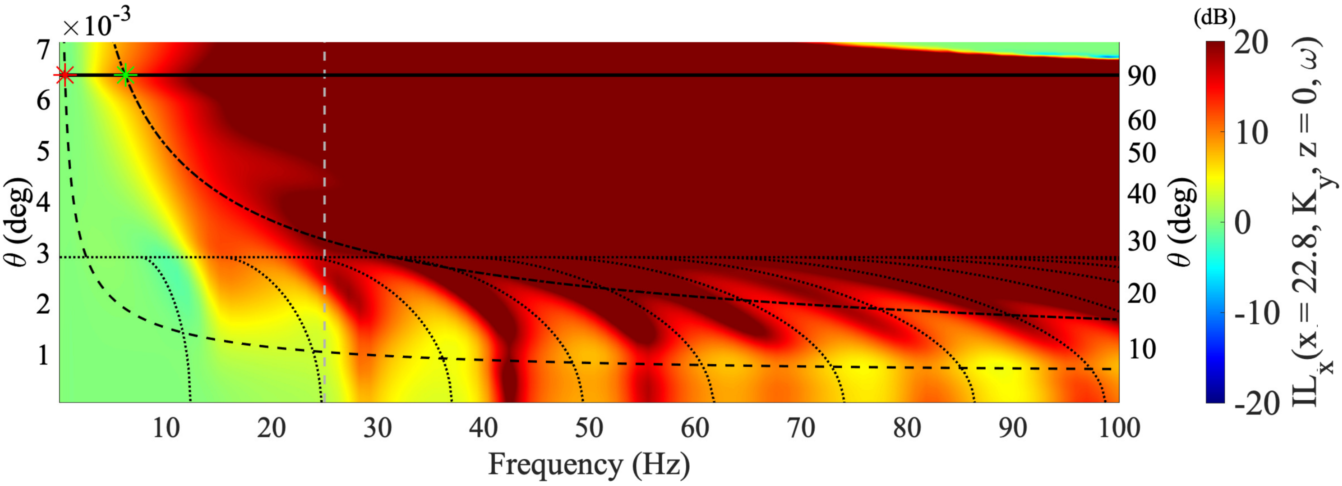

(b)

Figure A.10: Horizontal insertion loss $\mathrm{IL}_x(x = 22.8, K_y, z = 0, \omega)$ for softer soil and reference trench (a) and for reference soil and stiffer trench (b). Refer to Fig. 3.5 for the description of the superimposed curves.

The real part of the displacement field is displayed in Fig. A.11 for the softer soil case, while for the stiffer in-filled trench one in Fig. A.12. In this simulation $\Omega = 2\pi \times 25\,\text{Hz}$.

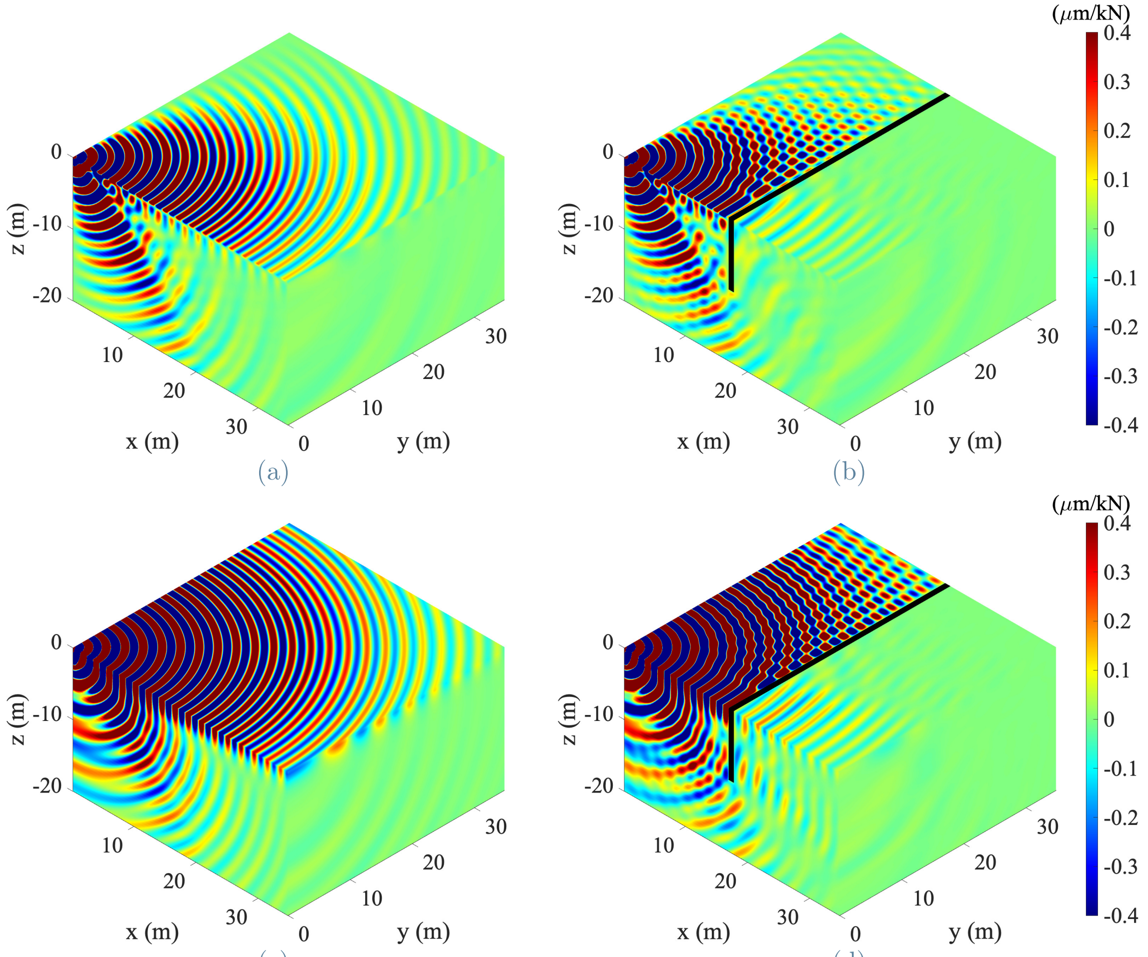

(a) (b)

(c) (d)

Figure A.11: Real part of displacement components generated by unit harmonic vertical point load with $\Omega = 2\pi \times 25\,\text{Hz}$ for the softer soil case ad reference trench, $x$ direction (first row) $z$ one (second row). Homogeneous soil (first column) and stiff in-filled trench (second column).

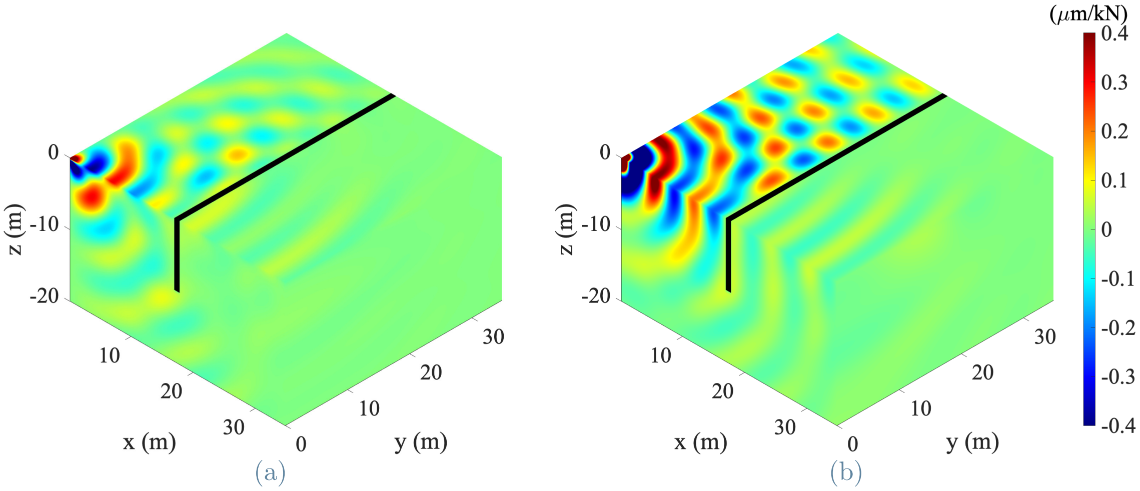

Figure A.12: Real part of displacement components generated by unit harmonic vertical point load with $\Omega = 2\pi \times 25\,\text{Hz}$ for the reference soil and stiffer trench case, $x$ direction (a) $z$ one (b).

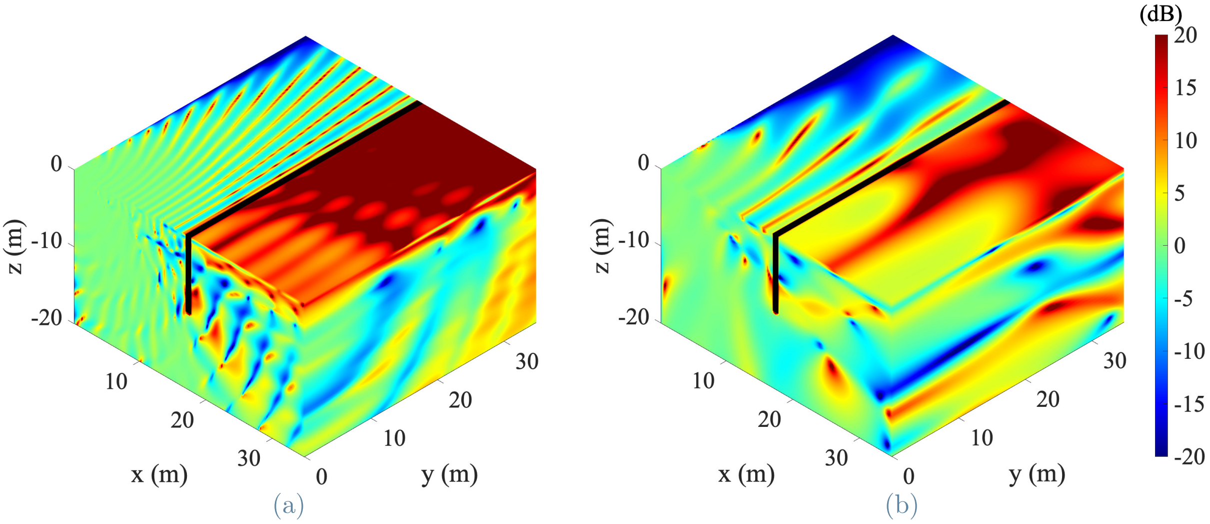

Figure A.13: Horizontal insertion loss $\text{IL}_x(x, y, z, \Omega = 2\pi \times 25\,\text{Hz})$ softer soil and reference trench (a) and for reference soil and stiffer trench (b).

The horizontal insertion loss $\text{IL}_x$ is plotted in the space domain for the softer soil and stiffer in-filler trench case in Fig. A.13, one next to the other. The set frequency is imposed equal to 25 Hz.

## Layered soil - Section 3.3

The three-dimensional plot of the vertical insertion loss in the space-wavenumber-frequency domain is provided in Fig. A.14 for the non-dispersive layered half-space.

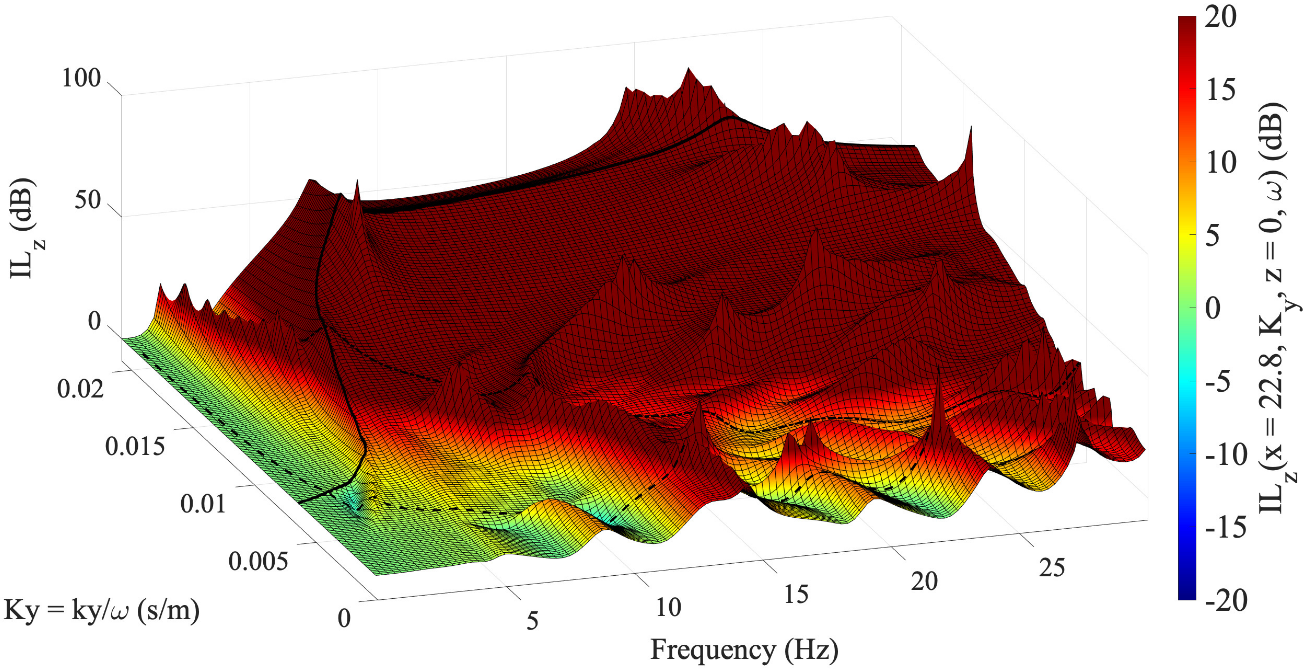

Figure A.14: Vertical insertion loss $\mathrm{IL}_z(x = 22.8, K_y, z = 0, \omega)$ for the reference stiff in-filled trench embedded in layered half-space. Refer to Fig. 3.6 for the description of the superimposed curves.

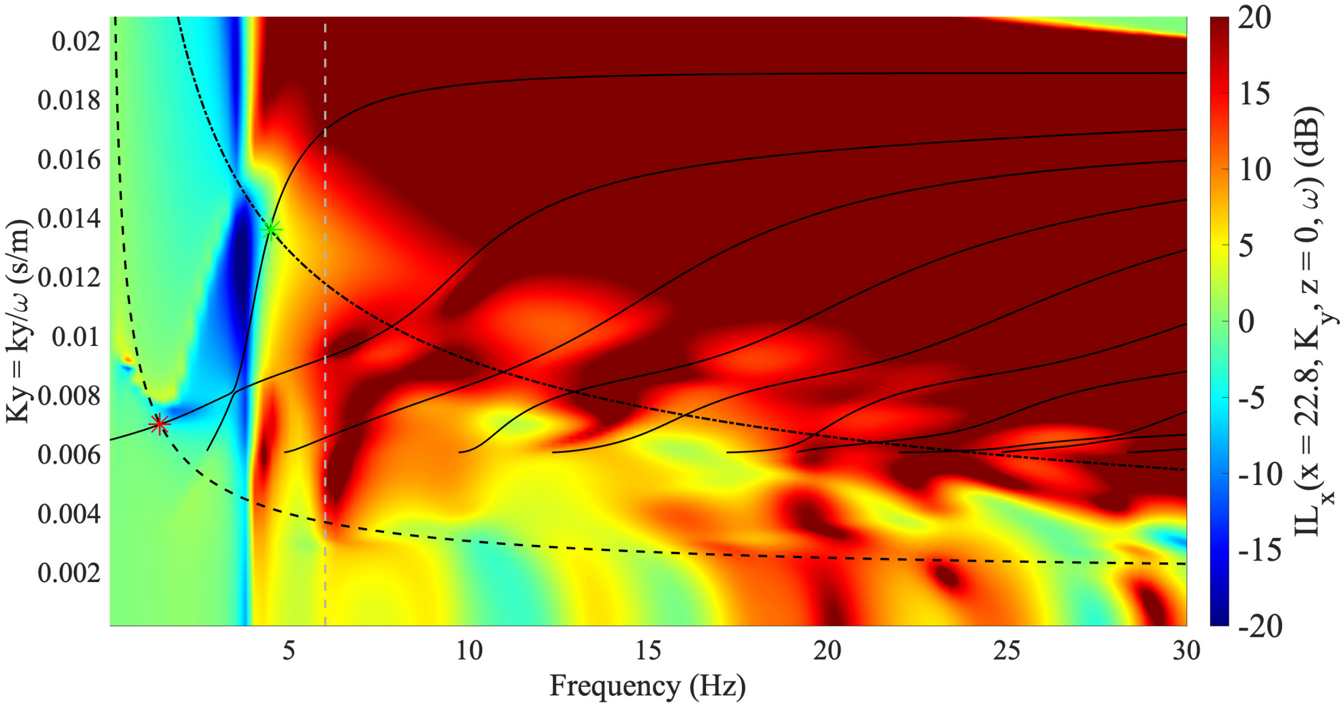

Figure A.15: Horizontal insertion loss $\mathrm{IL}_z(x = 22.8, K_y, z = 0, \omega)$ for the reference stiff in-filled trench embedded in layered half-space. Refer to Fig. 3.17 for the description of the superimposed curves.

The horizontal insertion loss $\mathrm{IL}_x$ for the layered half-space in the space-wavenumber-frequency ($x = 22.8\,\mathrm{m}$ and $z = 0\,\mathrm{m}$) is given in the underlying figure.

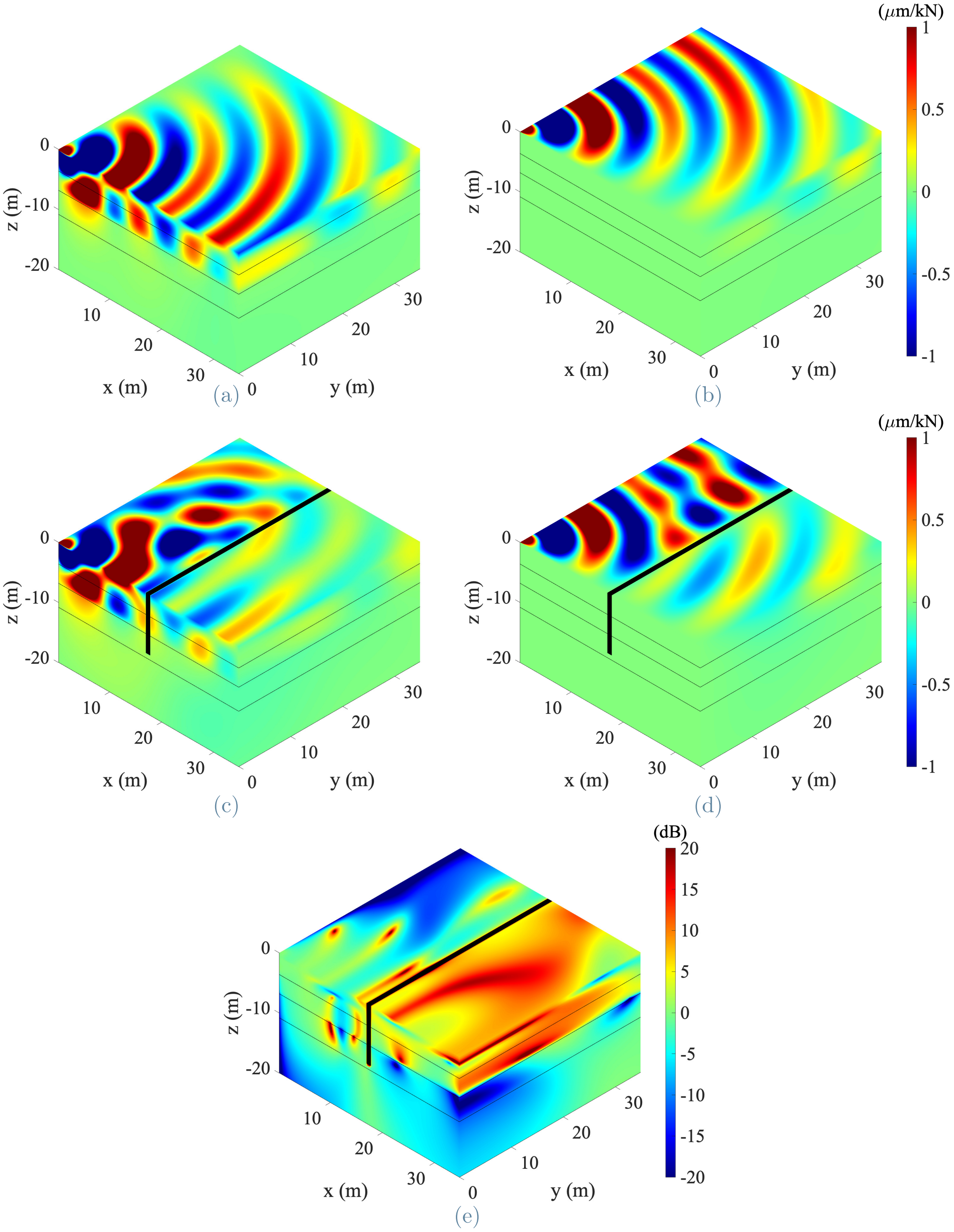

Figure A.16: Real part of horizontal displacement components generated by unit harmonic vertical point load with $\Omega = 2\pi \times 6\,\mathrm{Hz}$, $x$ direction (column) $y$ one (second column). Homogeneous soil (first row) and stiff in-filled trench (second row). $\mathrm{IL}_x$ (third row).

The real part of the horizontal components and the $\mathrm{IL}_x$ are reported in the space domain for $\Omega = 2\pi \times 6\,\mathrm{Hz}$ in Fig. A.16.

The PSD for the five geophones locations in the $x$ and $z$ directions is depicted in Fig. A.17. The results are not reported in the $y$ direction because that displacement component is null due to symmetry reasons.

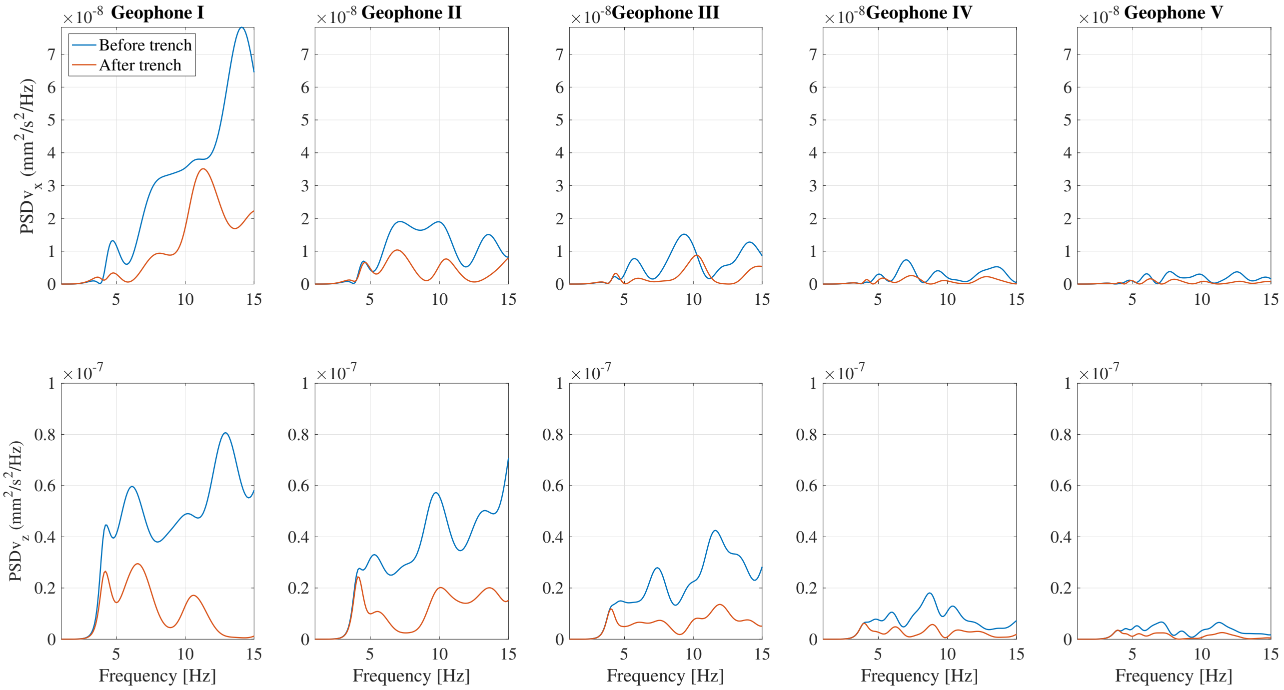

Figure A.17: Numerical PSD for the five geophones locations associated with the vertical harmonic load simulation in layered half-space (blue) and with stiff in-filled trench (orange).

The comparison of the numerical and experimental insertion loss for all the available geophones positions is provided in Fig. A.18. The numerical outcomes derive from the vertical harmonic point simulation, while the experimental ones from the dropping load test that is described in Section 2.2.

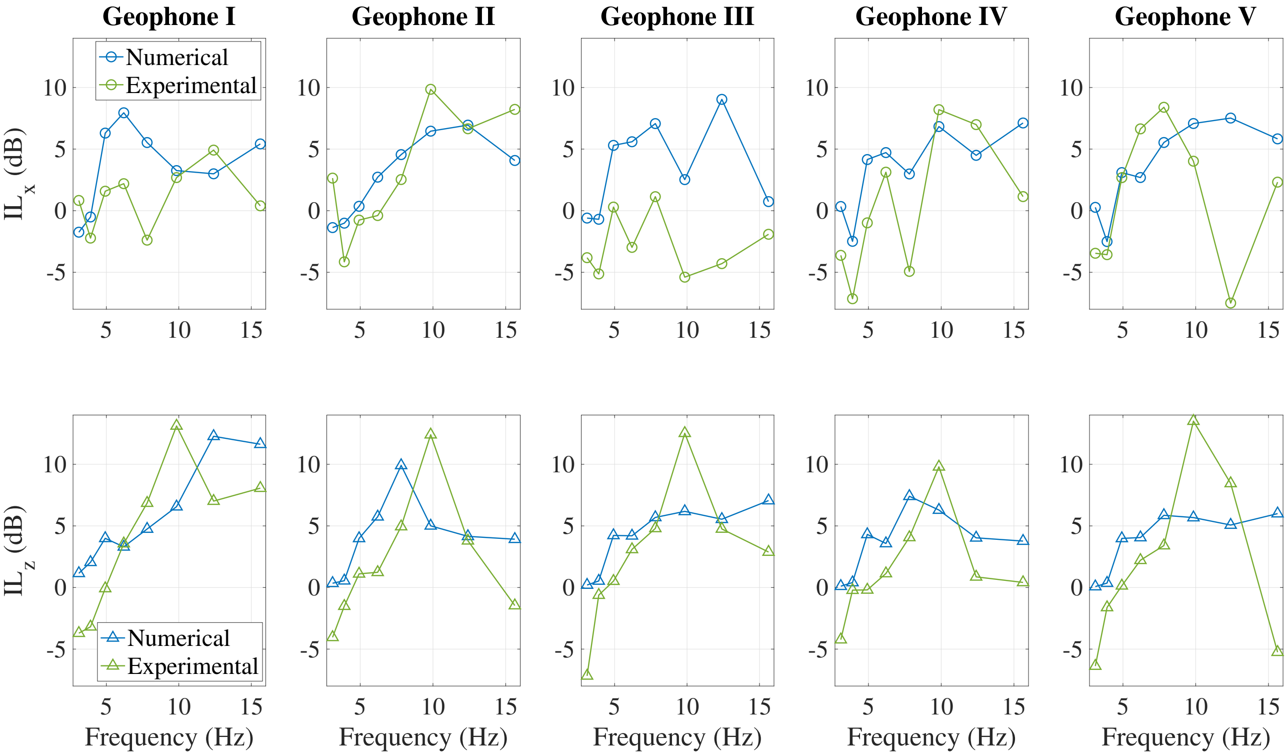

Figure A.18: Comparison numerical (blue) and experimental (green) insertion loss for the five geophones locations in $x$ (circle) and $z$ (triangle) direction.

## Trench and soil properties - Section 4.3

The properties of the homogeneous half-space and concrete resonator from [34] are reported in Table 3. Note that zero damping is imposed in the literature example, while $\xi_d = 0.1\%$ for the exact operation of FEMIX simulations.

Table 3: Unit cell and soil properties [34].

| | $\rho\,(\mathrm{kg/m^3})$ | $E\,(\mathrm{MPa})$ | $\nu$ | $c_P\,(\mathrm{m/s})$ | $c_S\,(\mathrm{m/s})$ | $c_R\,(\mathrm{m/s})$ |
|---|---|---|---|---|---|---|
| Resonator | 2500 | 30000 | 0.2 | 2472 | 1179 | 1074 |
| Soil | 1800 | 30 | 0.3 | 150 | 80 | 74 |

## Metawedge for railway application

Fig. A.19 shows the horizontal insertion loss $\mathrm{IL}_x$ value at the surface level for different excitation frequency and position values. The analogous plot for the insertion loss in the vertical direction is offered in Fig. 4.10a.

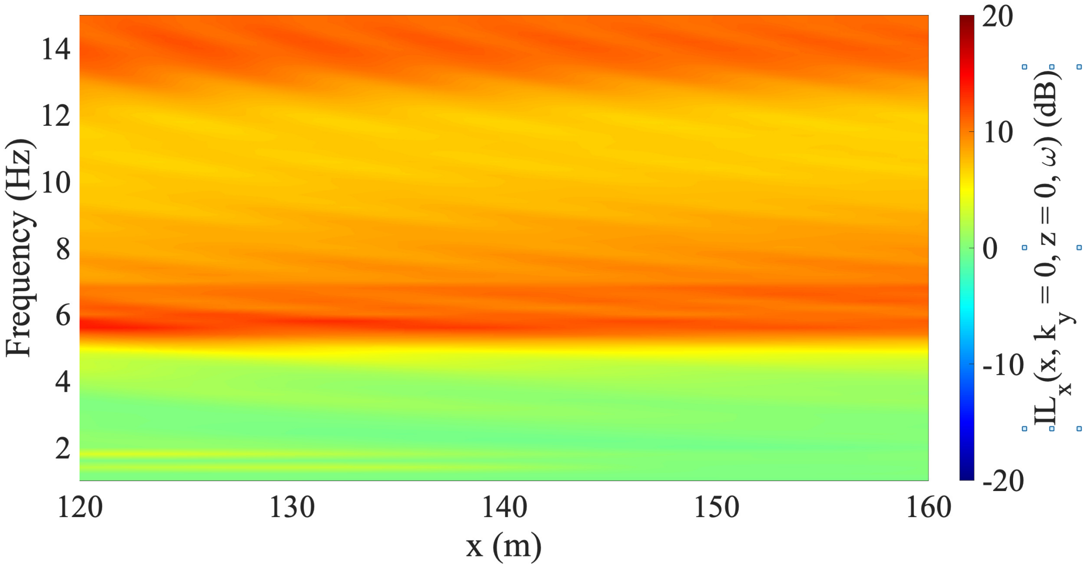

Figure A.19: $\mathrm{IL}_x(x, k_y = 0, z = 0, f)$ with $120\,\mathrm{m} < x < 160\,\mathrm{m}$.

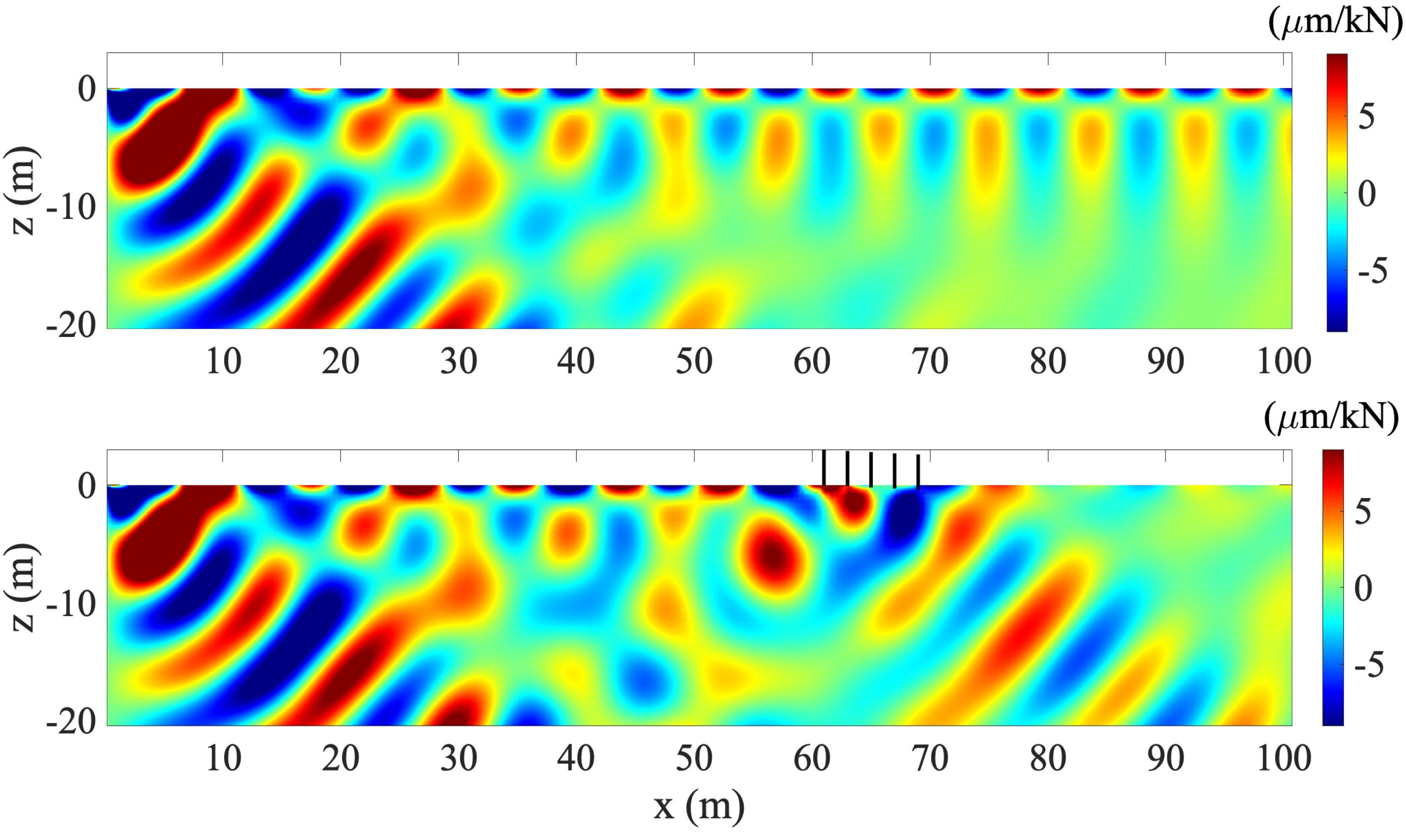

Figure A.20: Real part of the horizontal displacement component $\mathrm{Re}(u_x(x, k_y = 0, z, \Omega = 2\pi \times 6\,\mathrm{Hz}))$ generated by vertical harmonic load in homogeneous soil (first row) and with metawedge (second row).

In Fig. A.20 and Fig. A.21, the real part of the horizontal and vertical components of the displacement are plotted. The vertical harmonic force - located at $x = 0\,\mathrm{m}$ and $z = 0\,\mathrm{m}$ - is characterized by $\Omega = 2\pi \times 6\,\mathrm{Hz}$ , which is the dominant frequency value elicited by cargo trains [39]. The wave-mode conversion mechanism occurs when the incoming surface wave passes through the metawedge becoming shear bulk wave that is directed into the soil.

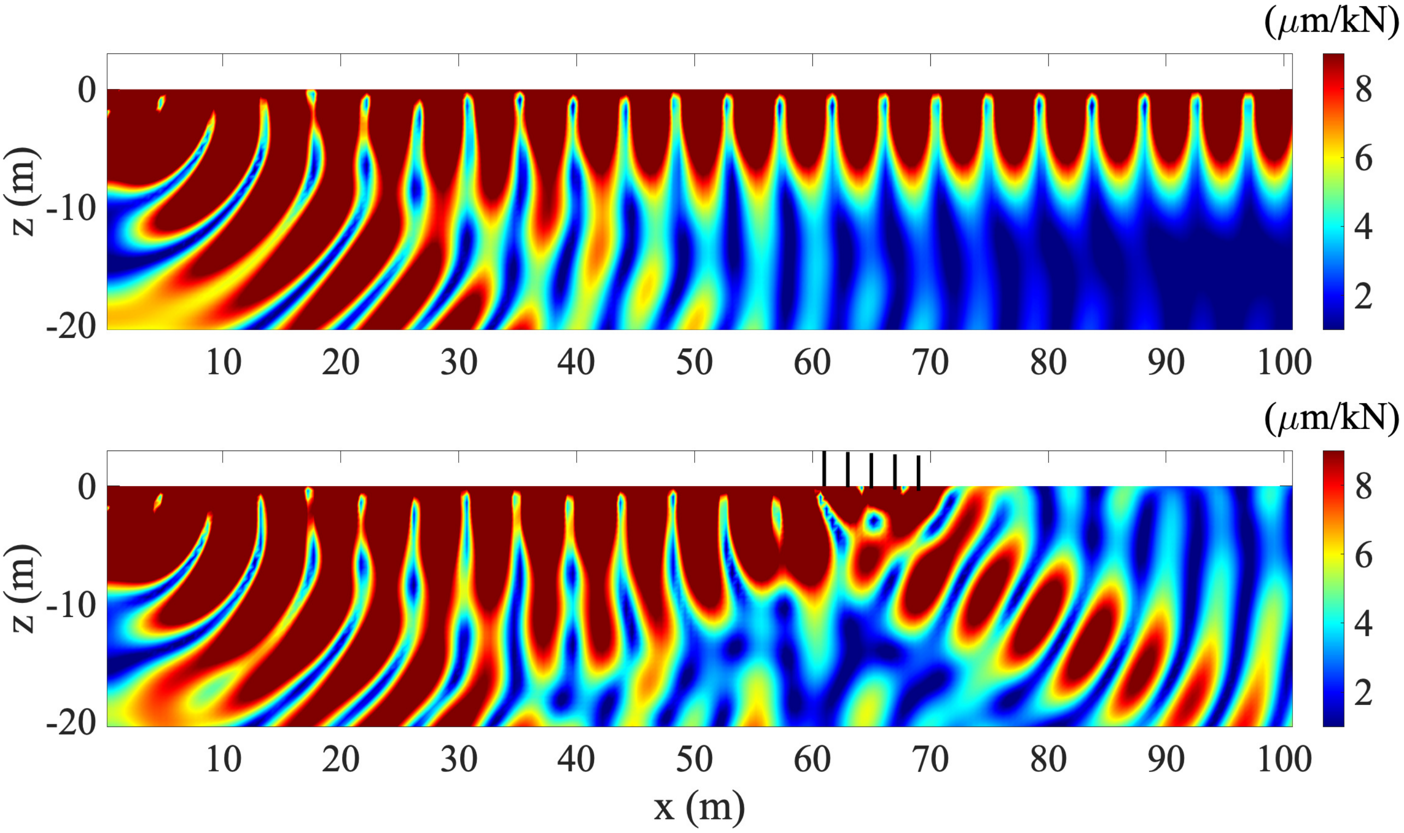

Figure A.21: $u_{\mathrm{Re}}(x, k_y = 0, z, \Omega = 2\pi \times 6\,\mathrm{Hz})$ generated by vertical harmonic load in homogeneous soil (first row) and with metawedge (second row).

Fig. A.22 depicts the horizontal insertion loss plot for the designed metawedge. It is computed in the space-wavenumber-frequency domain for a receiver located at the surface level for $x = 120\,\mathrm{m}$.

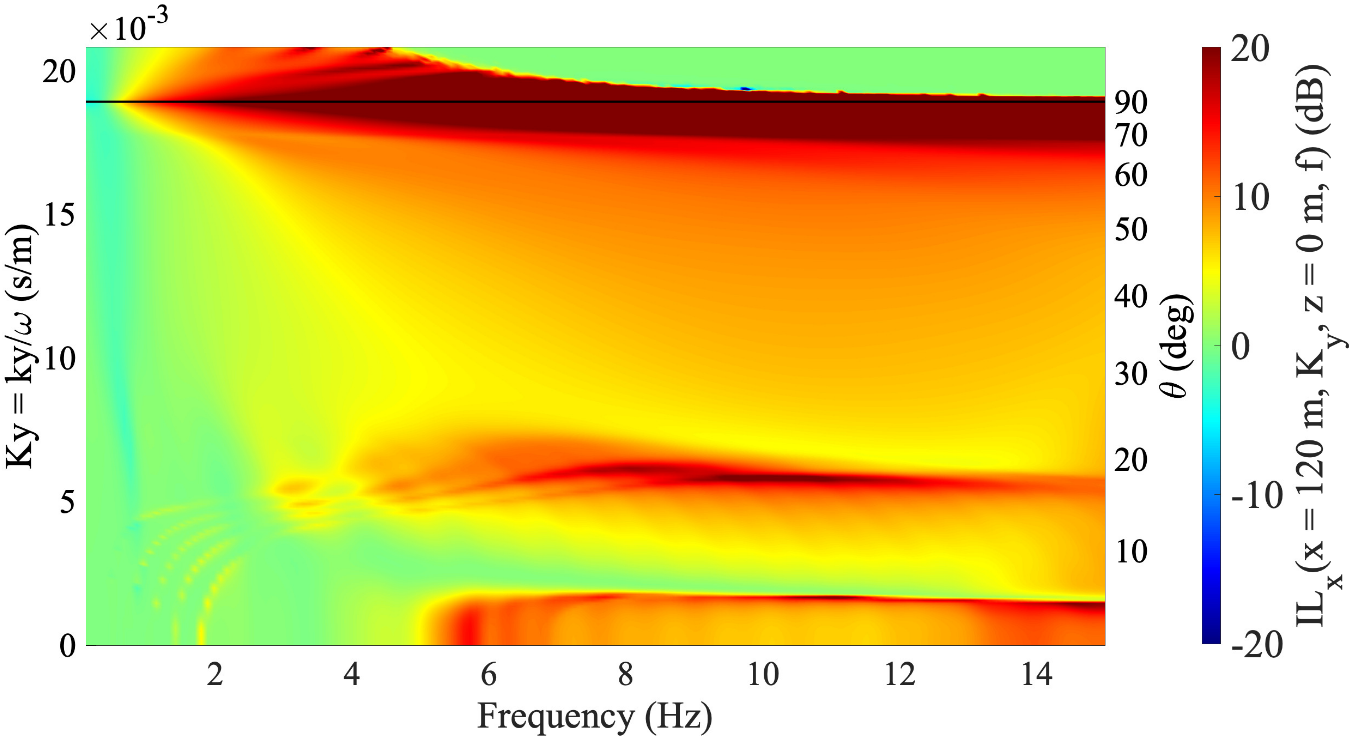

Figure A.22: Horizontal insertion loss $\mathrm{IL}_x(x = 120, K_y, z = 0, \omega)$ for the designed metawedge embedded in homogeneous half-space. Superimposed is the dispersion curve Rayleigh wave (solid line).

The effects related to a change of the dimensions of the resonator cross section are visible in Fig. A.23 and Fig. A.24. They depict the outcomes for a thicker board and smaller height, respectively. The discussion presented in Section 4.4.3 applies to them.

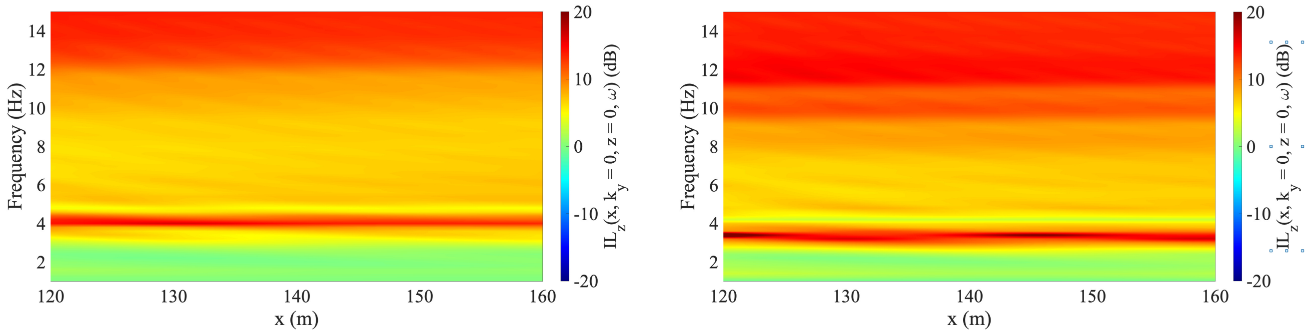

(a) $t = 0.5\,\mathrm{m}$ and $h = 3\,\mathrm{m}$.

(b) $t = 0.8\,\mathrm{m}$ and $h = 3\,\mathrm{m}$.

Figure A.23: $\mathrm{IL}_z(x, k_y = 0\,\mathrm{m}^{-1}, z = 0\,\mathrm{m}, \omega)$ with resonator thickness $t$ increase.

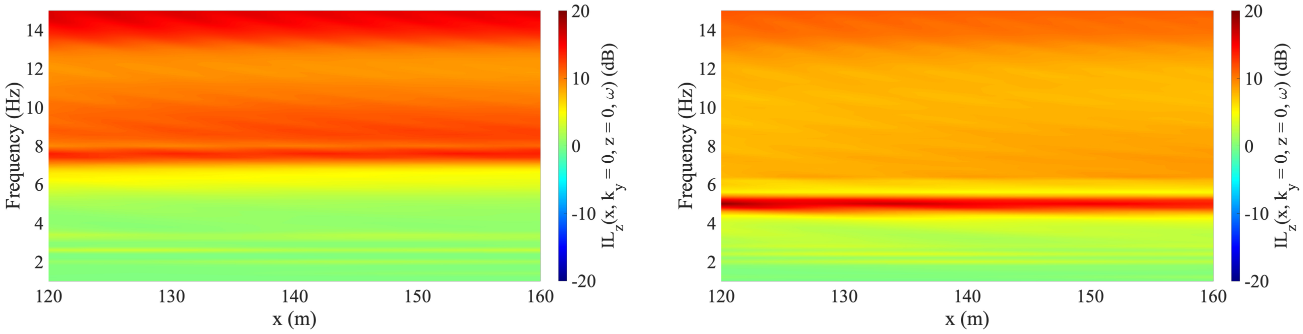

(a) $t = 0.2\,\mathrm{m}$ and $h = 2\,\mathrm{m}$. (b) $t = 0.5\,\mathrm{m}$ and $h = 2\,\mathrm{m}$.

Figure A.24: $\mathrm{IL}_z(x, k_y = 0, z = 0, \omega)$ with resonator height $h$ decrease.

The performance of the metawedge with different board dimensions are displayed in Fig. A.25a and Fig. A.25b, while Fig. A.25c depicts the performance of the concrete metawedge. The discussion presented in Section 4.4.4 is valid for them.

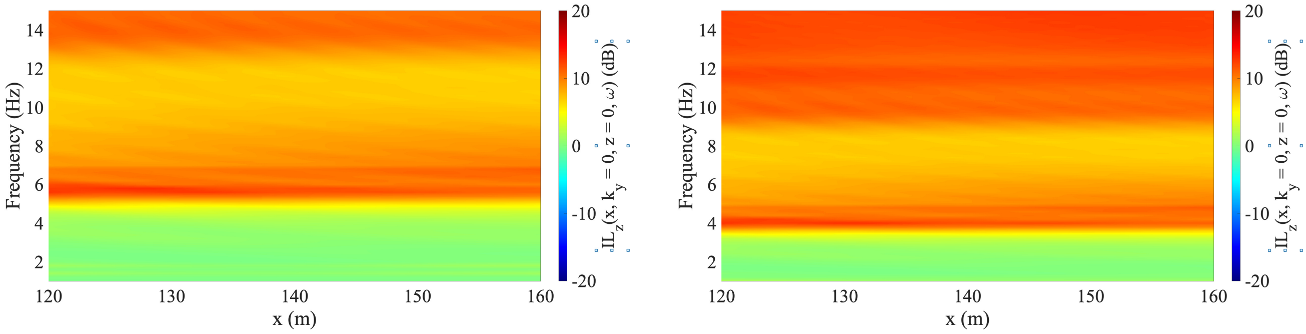

(a) $E_{Steel} = 100\,\mathrm{GPa}$. (b) $E_{Soil} = 7.5\,\mathrm{MPa}$.

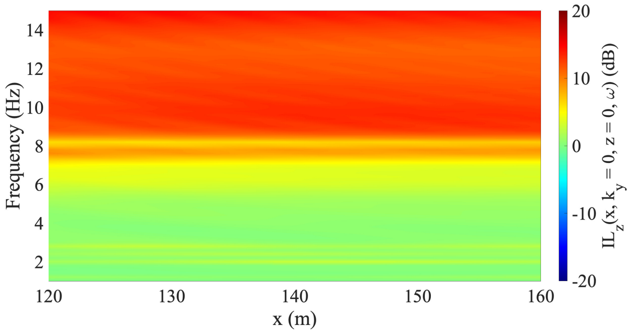

(c) Concrete metawedge.

Figure A.25: $\mathrm{IL}_z(x, k_y = 0, z = 0, \omega)$ for softer steel and reference soil (a), for reference steel and softer soil (b) and for concrete metawedge and reference soil (c).

The displacement field of the horizontal component and the horizontal insertion loss are plotted in Fig. A.26a and Fig. A.26b for $\Omega = 2\pi \times 6\,\mathrm{Hz}$, respectively.

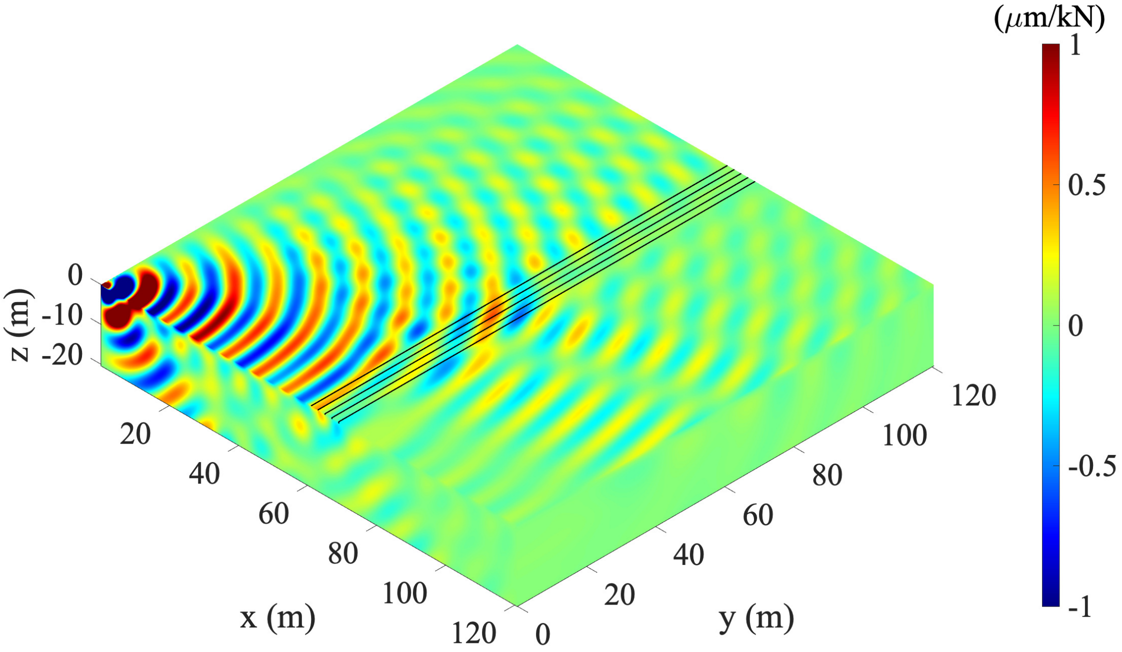

(a) $\mathrm{Re}(u_x(x, y, z, \Omega = 2\pi \times 6\,\mathrm{Hz}))$.

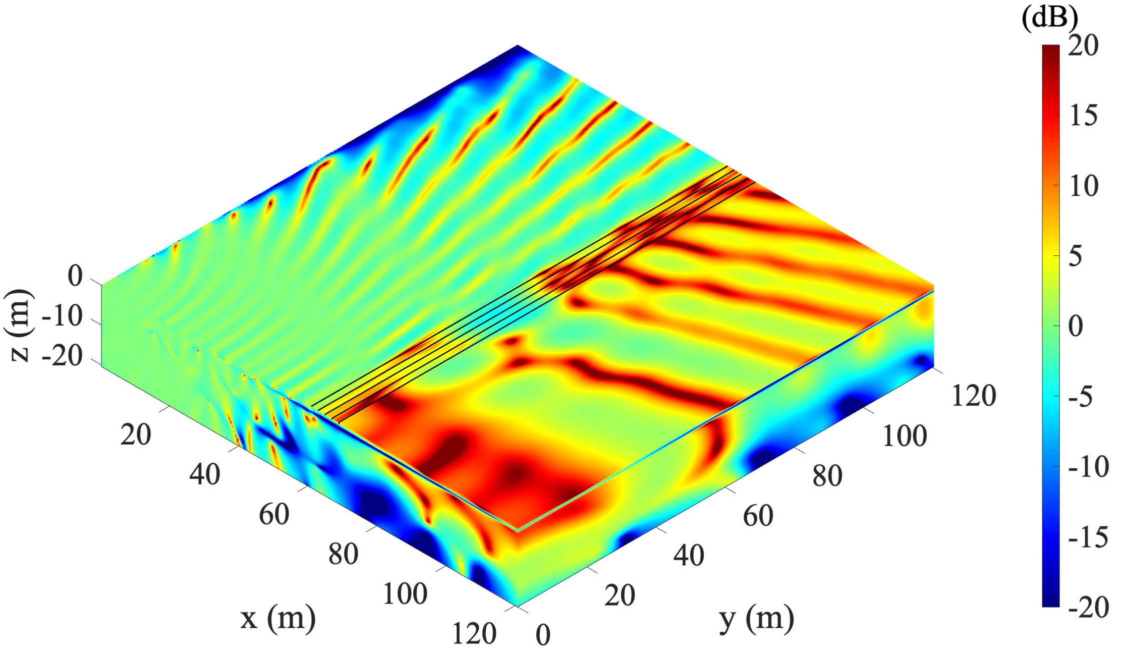

(b) $\mathrm{IL}_x(x, y, z, \Omega = 2\pi \times 6\,\mathrm{Hz})$.

Figure A.26: Real part of the horizontal displacement component (a) and horizontal insertion loss (b) generated by unit harmonic vertical point load.

# List of Figures

# List of Tables

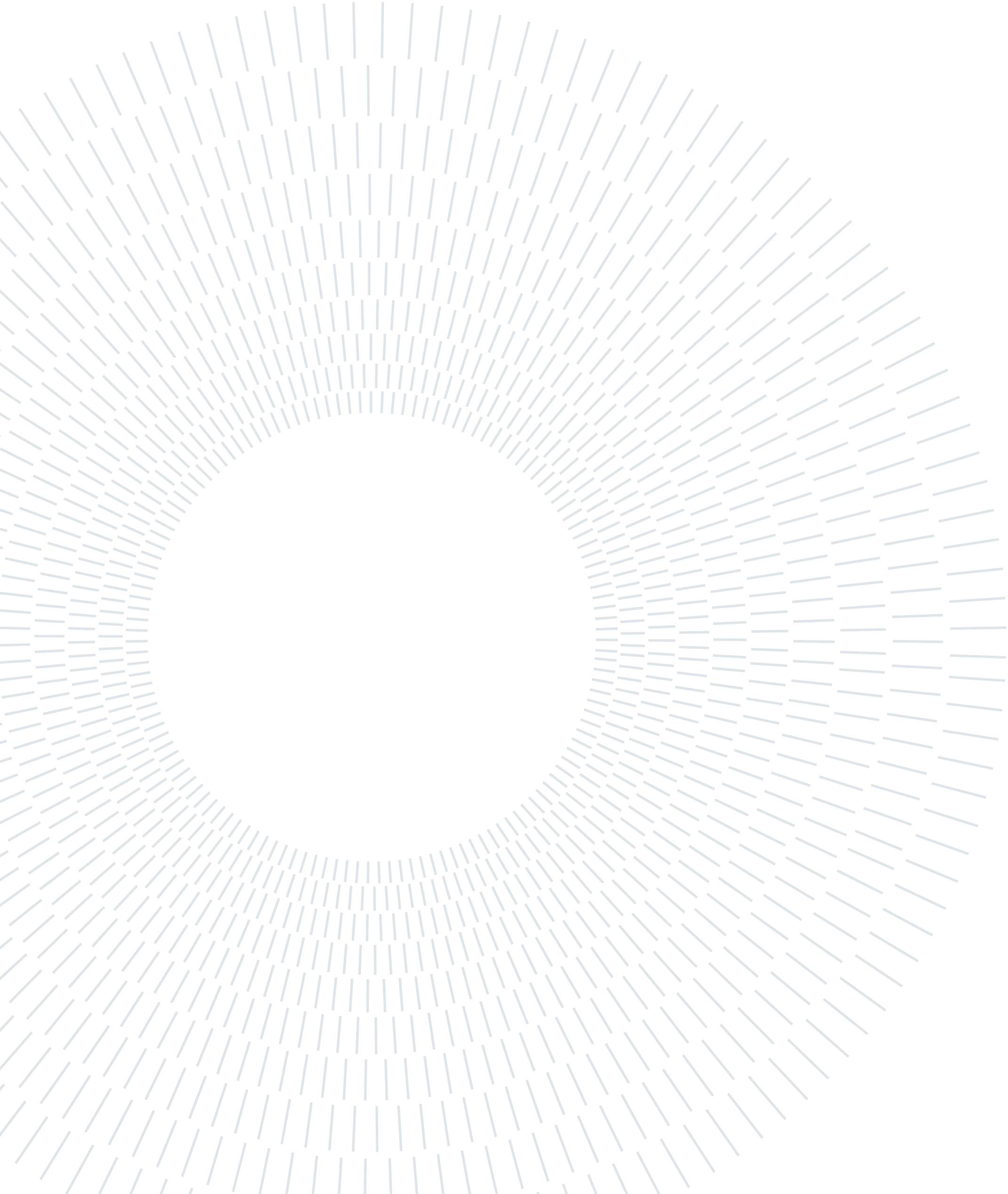

# Acknowledgements

At first, I would like to thank Prof. Corradi for the helpfulness and support. Thank you for giving me the opportunity to work on this project, making this collaboration between PoliMi and TU Delft possible.

I would like to thank Prof. van Dalen and Prof. Metrikine for the valuable advice on critical points of the study and for giving the main directions.

I would like to thank Andrei Fărăgău for the countless hours you have dedicated to carefully guiding me, always with patience and trust. With the research group, you all welcomed me and made me feel like one of you.

I would also like to thank Eliam Vlijm for the fundamental contribution to the work, especially with the most practical engineering aspects. Thank you for the amazing experience at the Cohere Consultants.

Furthermore, I would like to thank João de Oliveira Barbosa for making FEMIX available and for the priceless help with the modelling approach.

Last but not least, I would like to thank Qianqian Li for the constructive suggestions, they helped me during the writing phase of the report.

At last, an immeasurable thank you to my family and Carola for their special and inspiring role. Without you and friends, I would not be where I am today.